Novel femtosecond optical parametric oscillators in the infrared

Callum Francis O'Donnell

Universitat Politecnica de Catalunya

Barcelona, September 2018

Doctorate Program: **Photonics**

Duration: **2015-2018**

Thesis advisor: **Prof. Majid Ebrahim-Zadeh**

Thesis co-advisor: **Dr. Chaitanya Kumar Suddapalli**

Thesis submitted in partial fulfillment of the requirements for the degree of Doctor of Philosophy of the Universitat Politecnica de Catalunya

December 2018

Dedicated to my family and friends

Those people who think they know everything, are a great annoyance to those of us who do.

- Isaac Asimov

Declaration

I hereby declare that the matter embodied in the thesis entitled, **"Novel femtosecond optical parametric oscillators in the infrared"** is the result of investigations carried out by me at the ICFO-Institute of Photonic Sciences, Castelldefels, Barcelona, Spain under the supervision of Prof. Majid Ebrahim-Zadeh, and Dr. Chaitanya Kumar Suddapalli, and that it has not been submitted elsewhere for the award of any degree or diploma. In keeping with the general practice in reporting scientific observations, due acknowledgment has been made whenever the work described is based on the findings of other investigators.

_____

Callum F. O'Donnell

Certificate

I hereby certify that the matter embodied in this thesis entitled, **"Novel femtosecond optical parametric oscillators in the infrared"** has been carried out by Mr. Callum F. O'Donnell at the ICFO-Institute of Photonic Sciences, Castelldefels, Barcelona, Spain, under my supervision, and that it has not been submitted elsewhere for the award of any degree or diploma.

_____

Prof. Majid Ebrahim-Zadeh

(ICFO, Research supervisor)

_____

Dr. Chaitanya Kumar Suddapalli

(Radiantis, Research co-supervisor)

Acknowledgements

Attempting to list all the people who have helped and supported me during these formative and often exhilarating last three years is a herculean task in itself. First and foremost, I owe an immense amount of gratitude to Prof. Majid Ebrahim-Zadeh and Dr. Sara Otero for offering the unique opportunity to conduct my PhD studies under their supervision, in the wonderful city of Barcelona. Majid's continual guidance and encouragement, as well as his vast scientific and industrial knowhow, instilled in me the necessary confidence to carry out each experiment and communicate the results in the most effective way possible. I count myself lucky to have had an advisor whose friendly and approachable nature meant any discussion we had felt relaxed and informal, whether the subject be a complicated technical issue or Premier League football. Additionally, being a part of the Marie Sklodowska-Curie Innovative Training Networks was a huge privelige and gave me opportunities and knowledge I never expected to have.

Work at ICFO was always made easier by having a close group of labmates, especially since so many of us started and finished our PhDs at similar times so were in the struggle together. Cheers to Pep, Jun, Anuja, Hanyu, Shahrzad, Sukeert and Biplob, I'm glad we could help each other out and I hope we can stay in touch in the future! Anuja, Hanyu and I have been lucky enough to travel a lot around Europe to various meetings and conferences, and have many fond and funny memories of exploring various cities. I'm also very grateful to Kavita, from showing me round the labs on the first day, to answering any random queries I had, and to Adolfo, for introducing me to the art of femtosecond laser alignment, and our enjoyable film discussions (and hosting a spectacular wedding!).

Most of the work in this thesis would not have been possible without the expertise and guidance of Chaitanya, who has been a great mentor and friend during my time here. His encyclopedic knowledge of the field, rigorous attention to detail, and superhuman dedication, has been a huge influence on me and the way I work. Also thank you to the PhD students in Roskilde, Lund, Berlin, and Exeter (Ashik, Saher, Lichun, Laurent, Yu-Pei, Rasmus, Mahmoud, Jan, Sylvain, Yohei, Michael and Pascaline) and academics involved in the Mid-TECH project, the times we spent together at summer schools and conferences were always full of entertainment and scientific enrichment. The tragic loss of our colleague and friend Morgan is something that has never been far from my mind. While working in Radiantis I learnt a lot from my colleagues, Antonio, Andy, Sarah, Nerea, Marie-France, Nieves, Ro-

man and Oscar, and will miss the familial atmosphere in the company. I'd also like to thank Prof. Lluis Torner and the management team, for fostering a world class environment to work in. ICFO is a well-oiled machine, and that is down to the efficiency of the various departments; HR, KTT, events, logistics, front desk, purchasing and the electronic/mechanical workshops. Their work enabled me to focus single-mindedly on my research. My time here was made extra memorable by all the Pyrenean hikes, and late nights in and around the city with a great group of friends, I'm already looking forward to return visits in the future. I'm glad I could offer holiday accommodation to my friends from the UK, your visits kept me relaxed and motivated during stressful times. Tess, I'll write something about you as well. It boggles my mind to think of the unlikely circumstances that brought us simultaneously to Barcelona, but it truly was the best surprise of all. Thanks for being the best lab/life collaborator.

Lastly, I want to give enormous thanks to my parents Frances and Paul, and sister Roisin, for always being so supportive of my choices, and not chastising me for pursuing science over the arts!

Abstract

High-repetition-rate femtosecond laser sources are essential laboratory tools for spectroscopy, microscopy, amongst other applications. With the relative length of one femtosecond to one second being similar to the length of 1 second compared to the age of the universe, such lasers enable scientists to probe physical processes at unimaginably short timescales. Furthermore, the high peak powers can excite strong nonlinear response in delicate material samples without delivering potentially damaging levels of energy. The infrared (IR) spectral region across 1–12 μm is rich in molecular absorption features, but in general poorly served by conventional coherent light sources. Optical parametric oscillators (OPOs) represent the most viable solution to this long-term issue, due to their table-top nature, and unparalleled tunability and spectral brightness in the near- and mid-IR.

Recent breakthroughs in nonlinear crystal technology have opened the door to the generation of laser light in the previously difficult to access region above 4 μm, using high power lasers near 1 μm. Exploiting these new nonlinear materials to improve the spectral coverage and output power of OPOs has the potential to provide important societal benefits, particularly in the fields of frequency metrology, security, and medical imaging. In addition, theoretical modelling and exploration of devices with novel cavity designs can lead to technological advances which improve OPO affordability and increase their appeal to a wider scientific audience.

In this thesis, we have demonstrated three OPOs across 1–8.4 μm in the infrared, which are pumped using well-established Ti:sapphire laser technology. The first is a compact and cost-effective device tunable across 1051–1700 nm in the near-IR, producing sub-100 fs pulses at 80 MHz. The incorportion of an optical fibre into the cavity leads to excellent passive power and wavelength stability, and enables soliton formation to be observed, together with other interesting nonlinear effects.

We have also demonstrated an efficient, low-threshold mid-IR OPO exploiting group-velocity match effects in MgO:PPLN, which enables the use of a long (42 mm) nonlinear crystal. In doing so, we report quantum conversion efficiencies as high as 48% from the near-IR ($\sim$1 μm) pump to the mid-IR (3.1–4.3 μm), and use the source to perform basic spectroscopy.

The third device uses Ti:sapphire light at $\sim$1 μm to directly pump the new nonlinear crystal, $CdSiP_2$, generating up to 20 mW average power across 6.6–8.4 μm in the deep mid-IR. As the first demonstration of a single-stage Ti:sapphire-pumped deep mid-IR OPO with practical output powers, it has potential for medical imaging applications in the important amide II and III regions.

Finally, upconversion imaging using femtosecond OPOs is reported and briefly discussed, together with future directions for deep mid-IR generation using orientation-patterned gallium phosphide (OP-GaP).

Resumen

Las fuentes de láser de femtosegundo son instrumentos esenciales para espectroscopia, microscopía, entre otras aplicaciones. Dado que la duración relativa de un femtosegundo a un segundo es comparable con la duración de 1 segundo con respecto a la edad del universo, estos láseres permiten a los científicos investigar procesos físicos en escalas de tiempo increíblemente cortas. Además, las altas potencias de pico pueden provocar fuertes respuestas no lineales en materiales delicados sin entregar niveles de energía potencialmente dañinos. La región espectral del infrarrojo (IR) tiene numerosas características de absorción molecular, pero en general está mal servida por fuentes de luz coherentes convencionales. Los osciladores ópticos paramétricos (OPOs) representan la solución más viable para este problema a largo plazo, debido a su portabilidad, su capacidad de sintonizar y brillo espectral en el IR cercano y medio.

Los avances recientes en la tecnología de cristales no lineales han permitido la generación de luz en la región de difícil acceso inferior a 4 μm, utilizando láseres de alta potencia cercanos a 1 μm. La explotación de estos nuevos materiales no lineales para mejorar la cobertura espectral y la potencia de salida de los OPOs, tiene el potencial de ofrecer beneficios sociales importantes, especialmente a través de los campos de metrología de frecuencias, seguridad e imágenes médicas. Además, el modelado teórico y la exploración de dispositivos con diseños de cavidades novedosos, puede conducir a avances tecnológicos que mejoran la asequibilidad del OPO y aumentan su atractivo para una audiencia científica más amplia.

En esta tesis, hemos demostrado tres OPO en el rango espectral de 1–8.4 μm en el infrarrojo, que se bombean utilizando tecnología de làser bien establecida como el Ti: sapphire. En primer lugar, se demostró un dispositivo compacto y rentable, sintonizable a través de 1051–1700 nm en el IR cercano, que produce pulsos <100 fs a 80 MHz. La incorporación de una fibra óptica en la cavidad conduce a una excelente potencia pasiva y estabilidad de la longitud de onda, y permite observar la formación de solitones, con otros efectos no lineales interesantes.

También hemos demostrado un OPO de infrarrojo medio eficiente, de bajo umbral, que explota la coincidencia de velocidad de grupo en MgO:PPLN, que permite el uso de un cristal no lineal largo (42 mm). Al hacerlo, reportamos eficiencias de conversión cuántica tan altas como 48% desde la bomba de IR cercano (~ 1 μm) hasta el IR medio (3.1–4.3 μm), y usamos la fuente para realizar la espectroscopia básica.

El tercer dispositivo utiliza luz de láser Ti:sapphire cerca de 1 μm para bombear

directamente el nuevo cristal no lineal $CdSiP_2$, generando hasta 20 mW de potencia promedio con longitud de onda de 6.6–8.4 μm en el IR medio profundo. Como la primera demostración de un OPO de infrarrojo medio bombeado por un Ti:sapphire láser en una sola etapa con potencias de salida prácticas, tiene potencial para aplicaciones de imágenes médicas en las importantes regiones amida II y III.

Finalmente, las imágenes de conversión ascendente que utilizan un OPO de femtosegundo es comentada y analizada brevemente, junto con los futuros avances para la generación de IR profundo con un cristal de OP-GaP.

Publications

Journal Publications

1. **C. F. O'Donnell**, S. Chaitanya Kumar, and M. Ebrahim-Zadeh: "Low threshold, highly efficient, tunable mid-IR optical parametric oscillator exploiting group-velocity matching in MgO:PPLN," (to be submitted).

2. **C. F. O'Donnell**, S. Chaitanya Kumar, T. Paoletta, and M. Ebrahim-Zadeh: "Generation of widely tunable, ultra-stable, sub-100 fs solitons and dispersive pulses in a fibre-feedback optical parametric oscillator," (to be submitted).

3. A. S. Ashik, **C. F. O'Donnell**, S. Chaitanya Kumar, M. Ebrahim-Zadeh, P. Tidemand-Lichtenberg, and C. Pedersen: "Mid-infrared synchronous femtosecond upconversion imaging using an optical parametric oscillator," (to be submitted).

4. **C. F. O'Donnell**, S. Chaitanya Kumar, K. T. Zawilski, P. G. Schunemann and M. Ebrahim-Zadeh: "Single-stage Ti:sapphire-pumped deep-infrared optical parametric oscillator based on $CdSiP_2$," IEEE J. Sel. Top. Quantum Electron. 24, 1-9 (2018).

5. **C. F. O'Donnell**, S. Chaitanya Kumar, K. T. Zawilski, P. G. Schunemann and M. Ebrahim-Zadeh: "Critically phase-matched Ti:sapphire-laser-pumped deep-infrared femtosecond optical parametric oscillator based on $CdSiP_2$," Opt. Lett. 43, 1507-1510 (2018).

Conference Publications

1. **C. F. O'Donnell**, S. Chaitanya Kumar, T. Paoletta, and M. Ebrahim-Zadeh: "Soliton fibre-feedback femtosecond optical parametric oscillator," EPS-QEOD Europhoton Conference, Barcelona, Spain, September 2018.

2. **C. F. O'Donnell**, S. Chaitanya Kumar, and M. Ebrahim-Zadeh: "Broadband mid-IR femtosecond optical parametric oscillator exploiting zero-group-velocity-mismatch in MgO:PPLN," EPS-QEOD Europhoton Conference, Barcelona, Spain, September 2018.

3. B. Nandy, S. Chaitanya Kumar, J. Canals Casals, **C. F. O'Donnell**, and M. Ebrahim-Zadeh, "Compact, stable, high-average-power, integrated-mirror-fiber-feedback picosecond optical parametric oscillator for the near- and mid-infrared," EPS-QEOD Europhoton Conference, Barcelona, Spain, September 2018.

4. **C. F. O'Donnell**, S. Chaitanya Kumar, T. Paoletta, and M. Ebrahim-Zadeh: "Compact fibre-integrated femtosecond optical parametric oscillator," Conference on Lasers and Electro-Optics (CLEO), San Jose, USA, May 2018.

5. **C. F. O'Donnell**, S. Chaitanya Kumar, K. T. Zawilski, P. G. Schunemann and M. Ebrahim-Zadeh: "Critically phase-matched deep-infrared femtosecond optical parametric oscillator based on $CdSiP_2$," Conference on Lasers and Electro-Optics (CLEO), San Jose, USA, May 2018.

6. **C. F. O'Donnell**, S. Chaitanya Kumar, T. Paoletta, and M. Ebrahim-Zadeh: "Compact femtosecond optical parametric oscillator based on an integrated fibre retroreflector," SPIE Photonics Europe, Strasbourg, France, April 2018.

7. **C. F. O'Donnell**, S. Chaitanya Kumar, K. T. Zawilski, P. G. Schunemann and M. Ebrahim-Zadeh: "High-Average-Power, Deep-Infrared, Ti:sapphire-Pumped Femtosecond Optical Parametric Oscillator Based on $CdSiP_2$," Mid-Infrared Coherent Sources (MICS), Strasbourg, France, March 2018.

8. **C. F. O'Donnell**, S. Chaitanya Kumar, K. T. Zawilski, P. G. Schunemann and M. Ebrahim-Zadeh: "Femtosecond deep-infrared optical parametric oscillator pumped directly by a Ti:sapphire laser," SPIE Photonics West, San Francisco, USA, January 2018.

9. **C. F. O'Donnell**, S. Chaitanya Kumar, K. T. Zawilski, P. G. Schunemann and M. Ebrahim-Zadeh: "Single-Stage Ti:sapphire-Pumped Deep-Infrared Femtosecond Optical Parametric Oscillator based on $CdSiP_2$," Advanced Solid State Lasers (ASSL), Nagoya, Japan, October 2017.

Novel femtosecond optical parametric oscillators in the infrared

Contents

1 Introduction **12**

1.1 Background 12
1.2 Overview 18

2 Basics of Nonlinear Optics **21**

2.1 Optical nonlinearity 21
2.2 Second order nonlinear processes 22
2.3 Second order nonlinear susceptibility 24
2.4 Coupled wave equations in second order nonlinear optics . 28
2.5 Phase-matching 31
2.5.1 Birefringent phase-matching 31
2.5.2 Quasi-phase-matching 34
2.6 Optical parametric oscillators 37
2.6.1 Femtosecond pump sources 37
2.6.2 Gain, amplification, and threshold 39
2.6.3 Phase-matching bandwidth 41
2.6.4 Wavelength tuning 43

3 Femtosecond optical parametric oscillators **46**

3.1 Nonlinear material 46
3.2 Damage threshold 47
3.3 Dispersion and self-phase-modulation 48
3.3.1 Group-velocity mismatch 48
3.3.2 Group velocity dispersion 49
3.3.3 Cavity length tuning 51
3.3.4 Self-phase modulation 51
3.3.5 Interaction between GVM, GVD and SPM 52
3.3.6 Dispersion control 54
3.4 Resonator design 55
3.5 Numerical simulation 59

4 **Soliton fibre-feedback femtosecond optical parametric oscillator** 62
4.1 Background and motivation . . . 62
4.2 Experiment . . . 65
4.3 Experimental results . . . 67
4.3.1 Wavelength tuning . . . 67
4.3.2 Anomalous dispersion characteristics . . . 71
4.3.3 Normal dispersion characteristics . . . 72
4.4 Pulse dynamics . . . 77
4.4.1 Numerical model . . . 77
4.4.2 Anomalous dispersion simulations . . . 80
4.4.3 Spectral interference near degeneracy . . . 85
4.4.4 Normal dispersion simulations . . . 87
4.5 Conclusions . . . 89

5 **Low threshold, high efficiency, group velocity-matched mid-IR OPO** 91
5.1 Background . . . 91
5.2 Experimental setup . . . 94
5.3 Results . . . 96
5.3.1 Cavity length tuning . . . 96
5.3.2 Pump tuning . . . 96
5.3.3 Power and efficiency . . . 98
5.3.4 Spectral and temporal characteristics . . . 100
5.3.5 Spectroscopy . . . 101
5.4 Conclusions . . . 103

6 **Single-stage Ti:sapphire pumped OPO based on $CdSiP_2$** 106
6.1 Background and motivation . . . 106
6.2 Single-stage femtosecond parametric sources beyond 4 μm . 109
6.3 Experiment . . . 112
6.3.1 Experimental setup . . . 112

6.3.2 Nonlinear absorption 116
6.3.3 Device tuning 117
6.3.4 Output power 121
6.3.5 Spectrum and pulse durations 123
6.4 Conclusions 126

7 Summary and outlook **128**
7.1 Future directions 129

List of Figures

1.1 Emission wavelengths of commercially available ultrafast lasers. 13
1.2 Competing coherent sources. 16
1.3 Transparency ranges of different infrared nonlinear crystals, and their respective figures of merit. Dashed lines indicate crystals which are not widely available, or still under active development. The vertical dotted line marks the key 1 μm wavelength, where the most established high power lasers emit. 17
1.4 Outline of the thesis. 19
2.1 Polarisation response in the linear (blue) and nonlinear (red) optical regimes. 22
2.2 Second order nonlinear processes. 25
2.3 Coordinate system for calculating effective nonlinearity . . . 27
2.4 (a) Non-critical phase-matching (b) Critical phase-matching 32
2.5 Quasi-phase matched nonlinear crystal with a fan-grating structure. 36
2.6 Intensity of output waves in a parametric interaction for perfect (birefringent) phase-matching in black, quasi-phase matching in blue, and no phase-matching in red. 36
2.7 KLM Ti:sapphire cavity design. 38
2.8 (a) QPM parametric gain efficiency for the signal and idler in a 1-mm-long MgO:PPLN crystal, at a pump wavelength of 800 nm. (b) Signal gain bandwidth evaluated at $\Lambda = 20.5$ μm. 45
2.9 (a) Signal and idler parametric gain efficiency for pump tuning in a 1-mm-long MgO:PPLN crystal, at a fixed grating period of $\Lambda = 20.5$ μm. (b) Pump acceptance bandwidth evaluated at $\lambda_p = 800$ nm. 45

3.1 (a) An input 100 fs $sech^2$ pulse (dotted line) and the output (filled curve) after propagating through 5 cm of MgO:PPLN at 1 μm. (b) Instantaneous frequency variation across the final pulse. 50
3.2 Initially transform-limited $sech^2$ pulse undergoing SPM with a nonlinear phase shift of $\phi_{NL} = 4$. 53
3.3 Dispersion compensation using an equilateral prism pair. . . 55
3.4 Different resonator configurations used for synchronously pumped OPOs. (a) z-cavity, (b) x-cavity, (c) Ring cavity . . . 56
3.5 Femtosecond synchronously-pumped OPO operating in an x-cavity configuration. 57
3.6 Temporal and spectral evolution of a 100 fs pulse propagating through 10 cm of MgO:PPLN. 61
4.1 Schematic of the experimental setup for the Ti:sapphire pumped soliton fibre-feedback OPO. HWPs, half-wave plates; PBS, polarising beamsplitter; L, lenses; M, mirrors; OC, output coupler; SMF-28, single-mode fibre retroreflector. 66
4.2 Photo of the soliton fibre-feedback OPO. 67
4.3 Measured signal data points (white), superimposed on the parametric gain bandwidth for 1-mm-long MgO:PPLN crystal with QPM grating periods varying from $\Lambda = 19.0$–22 μm, calculated using the sellmeier equations in [99]. 68
4.4 Cavity delay tuning of the OPO, with measured signal data points plotted against relative change in cavity length, normalised to the shortest possible cavity for operation; inset: calculated net cavity GDD across the tuning range. 69
4.5 Measured signal spectra and output average power across the anomalous dispersion regime. 70
4.6 Typical interferometric autocorrelation at 1460 nm, and simultaneous signal spectrum. 72
4.7 Power stability measurement at $\lambda_s \sim 1455$ nm over a period of 30 minutes, inset: spectral stability measurement over a period of 30 minutes. 73

4.8 Rms fluctuations in central wavelength and FWHM bandwidth over 20 minutes. 73
4.9 Measured signal spectra and output average power across the normal dispersion regime. 74
4.10 Typical interferometric autocorrelation at 1215 nm and simultaneous signal spectrum. 75
4.11 Power scaling measurement at 1220 nm, inset: signal beam profile. 76
4.12 Spectral stability measurement at 1171 nm over a period of 20 minutes. 76
4.13 Schematic of the simplified model considered in the simulations. OC represents the fractional output coupler transmission (5% or 30%). 79
4.14 Simulation of a soliton pulse evolving from noise at an initial wavelength of 1350 nm, with ΔT_s free to adapt to the changing group velocity. Inset: Close-up of the final two round-trips at steady state, showing a pulse duration of 95 fs. (b) Corresponding spectral evolution showing the soliton self-frequency shift after 10 round trips. 80
4.15 Comparison of steady state simulated spectrum, to the experimentally measured spectrum at the same wavelength. . 81
4.16 Schematic of stable soliton formation: (1) Pulse builds from noise, (2) Pulse undergoes self-frequency shift (arrow indicates deceleration), (3) Cavity is delayed to resume synchronisation, (4) Synchronisation at λ_s' with a temporal offset ΔT_s from the cold cavity round-trip time. 82
4.17 Cavity length offset Δz from the cold cavity length as a function of the shifted soliton wavelength λ_s', as a function of intracavity peak power between 0 and 32 kW. Yellow spots represent points at which 2 kW contours are crossed for $\Delta z = 36$ μm. 83

4.18 Experimentally measured intracavity peak power vs wavelength when tuning by cavity delay for a grating period of 20.2 μm, compared to values taken from Figure 4.17. Arrows represent observed power hysteresis loop, the blue zone represents wavelengths at which oscillation is recovered. 84
4.19 (a) Idler spectra recorded from $\lambda_i \sim$ 1527 nm to degeneracy at ~1606 nm, showing the increase in modulation period $\Delta\lambda$. The signal spectrum also becomes visible as degeneracy is approached. (b) Comparison of experimentally determined $\Delta\lambda$, and relative signal/idler group delay, with the theoretical predictions. 86
4.20 (a) Simulated temporal and (b) spectral evolution of a femtosecond pulse from noise in the OPO at a central wavelength of 1104 nm. 88
4.21 (a) Comparison of the steady state simulated spectrum with an experimentally measured spectrum at the same wavelength, (b) experimentally measured autocorrelation, and (c) simulated autocorrelation at the same wavelength. 89
5.1 Parametric gain map for a 42-mm-long MgO:PPLN crystal at 100°C containing 4 QPM grating periods. Dashed lines represent the pump and signal wavelengths corresponding to group velocity matching between the pump and idler waves. 93
5.2 Experimental setup of the group-velocity-matched femtosecond OPO. M: mirrors, L: lenses, F: long-pass filter, OC: output coupler. 95

5.3 Cavity delay tuning of the OPO for grating periods of (a) 28.5 μm, (b) 29 μm, (c) 29.5 μm, and (d) 30 μm, with the signal and idler powers plotted as triangles and the signal wavelength as circles. Dotted lines represent calculated signal wavelengths corresponding to zero GVM between the experimentally determined optimum pump wavelength (shown on figure) and the idler. 97
5.4 Power and idler wavelength dependence on pump wavelength for $\Lambda = 28.5$ μm, with predicted optimum pump wavelength indicated by dotted line. 99
5.5 Power scaling of the device with signal and idler wavelengths of 1469 nm and 3369 nm, respectively. 100
5.6 Passive signal and idler power stability over one hour. . . . 101
5.7 (a) Pump autocorrelation trace at $\lambda_p = 1035$ nm, (b) corresponding spectrum, compared to the calculated acceptance bandwidth (dashed line), (c) signal autocorrelation trace at $\lambda_s = 1459$ nm, (d) corresponding spectrum compared to the parametric gain bandwidth. 102
5.8 Idler spectra and average power across the tuning range. . . 103
5.9 Transmission spectroscopy of CH_4 using OPO idler output, compared to the HITRAN database. 104
6.1 (a) GVM between the pump at 993 nm, signal and idler, and GVD across 1100–1200 nm. (b) Spatial walk-off and aperture length for a phase-matching angle from $\theta = 70°$ to 90°. . 109
6.2 Signal and idler tuning curves for type-I ($e \rightarrow oo$) critical phase-matching as a function of the CSP internal angle for various pump wavelengths in the range so far used to pump CSP OPOs. 112
6.3 Schematic of the experimental setup for the Ti:sapphire-pumped CSP femtosecond OPO. HWP: Half wave plate, M: Mirrors, OC: Output coupler, L: Lenses. 113

6.4 Ti:sapphire power across 990–1015 nm. Insets: (a) spectra across tuning range, (b) typical interferometric autocorrelation. 114
6.5 Transmission of the 1-mm-long CSP across 900–1020 nm for both *ordinary (o)* and *extraordinary (e)* polarisations. 115
6.6 Transmission measurements of the 1-mm-long CSP crystal at 993 nm for both *ordinary (o)* and *extraordinary (e)* polarisations, at increasing intensities. 116
6.7 Pump tuning of the OPO across 993–1011 nm, superimposed on the parametric gain bandwidth for a 1-mm-long crystal. . 117
6.8 Idler and signal tuning as a function of the internal phase-matching angle in the CSP crystal, for pump wavelengths of 993 nm and 1000 nm, compared to the wavelength tuning curves predicted using the Sellmeier equations in [36]. Error bars represent additional cavity delay tuning. 119
6.9 Cavity delay tuning at normal incidence for a pump wavelength of 993 nm. 120
6.10 Signal and idler average powers measured across the total tuning range, using a 5% output coupler to extract the signal. 121
6.11 Power scaling of the idler extracted from the CSP femtosecond OPO. Inset: Input pump spectrum and depleted pump spectrum while the OPO is operating at maximum power. . 122
6.12 Passive power stability of signal and idler at 1143.3 nm and 7571 nm, respectively, measured over 1 hour. 123
6.13 Spatial beam profiles of the idler and signal at 7611 nm and 1142 nm, respectively. 124
6.14 Signal and idler spectra, with idler FWHM bandwidths across the tuning range of the OPO. 124
6.15 Signal intensity autocorrelation at (a) perfect cavity synchronisation, with (b) corresponding spectrum. (c) Signal intensity autocorrelation with the cavity detuned, with (d) corresponding spectrum. 125

7.1 Photo of synchronously-pumped OP-GaP OPO operating with idler ~7 μm. Visible light is non-phase-matched SHG of the resonant signal at ~1.2 μm. 129
7.2 Experimental setup used for mid-IR femtosecond synchronous upconversion imaging. PBS: Polarising beam splitter, HWPs: Half-wave plates, DBC: Dichroic beam combiner. 130

List of Tables

2.1 d_{ijk} contraction 26
2.2 Electric field components for the fundamental and second harmonic beams in an SHG interaction. 27
2.3 Different phase-matching combinations for the OPO process. 33
4.1 Quantities contributing to parametric gain. Refractive indices are calculated from [35]. 78
6.1 Femtosecond mid-IR and deep-IR single-stage OPOs. [a]Tuning methods: P: Pump tuning, A: Angle tuning, C: Cavity delay tuning, Q: QPM grating tuning. [b]Range defined relative to weighted centre of most extreme recorded spectra, not 10 dB limit. [c]Maximum idler power and power at selected wavelengths of interest. 111
6.2 Optics and coatings. 114

1 Introduction

1.1 Background

Once dismissed as "a solution looking for a problem," lasers are now a deeply ingrained part of society. Behind the scenes, they have streamlined and simplified some of our most common everyday tasks, including shopping, printing and watching TV. As a scientific tool, the laser has revolutionised numerous fields of research and has contributed to the award of 11 Nobel prizes across physics and chemistry, notably to Townes, Basov and Prokhorov in 1964 for the development of fundamental theory, to Bloembergen and Schawlow in 1981 for the advancement of laser spectroscopy and nonlinear optics, to Hall and Hänsch in 2005 for the invention of the optical frequency comb, and to Ashkin, Mourou and Strickland in 2018 for optical trapping and chirped pulse amplification [1]. Starting from the first working prototype, built by Theodore Maiman in 1961, the global laser industry has grown exponentially, and annual sales surpassed $13 billion in 2018 [2, 3]. These days, common markets for the laser are industrial manufacturing, communications, and academic research [4].

The principle of laser operation is based on stimulated atomic transitions, which produce a stream of identical photons with consistent spectral purity and coherence. Early devices were inefficient and restricted to emitting at just a few wavelengths, corresponding to discrete transitions in each material; 694 nm in ruby, 1064 nm in neodynium (Nd)-doped crystals, and 633 nm in helium-neon (He-Ne) to name a few examples. Soon, the demand for lasers at alternative wavelengths, particularly for the purpose of probing specific molecular resonances, outgrew the range of available sources and motivated the scientific community to search for new options. Key breakthroughs arrived in the form of dye lasers in 1964, and the Ti:sapphire laser in 1981, both of which exploit broadband emission spectra to tune over a much wider wavelength range. A broadband gain spectrum also supports the generation of ultrashort pulses, as short as a few femtoseconds, which enables rapid processes in biology and chem-

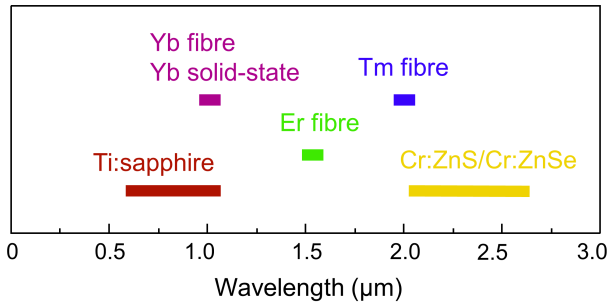

Figure 1.1: Emission wavelengths of commercially available ultrafast lasers.

istry to be studied in real time [5].

The spectral range across 2–20 μm is often referred to as the molecular fingerprint region, due to the rich prevalence of unique absorption features of common molecules [6]. An increasingly varied range of applications have begun to exploit these fingerprints, including security, environmental sensing, and food and medical diagnostics. Figure 1.1 shows the current range of commercially available ultrafast femtosecond lasers. Important parts of the visible and near-infrared (near-IR) are not covered, and the desire to perform spectroscopy in the atmospheric transmission windows across 3–5 μm and 8–12 μm is compounded by the lack of any laser source beyond 3 μm. This highlights the clear need to develop new coherent sources, in order to fully realise the potential of laser-based technologies.

The invention of the laser enabled interactions between high-intensity electric fields and matter to be studied in a controlled lab environment, and led to an explosion in discoveries of new phenomena in the blossoming field of nonlinear optics. Nonlinear optical effects, specifically the Kerr, Pockels, and Raman effects, were observed as early as the late 19th century, and the umbrella term "nonlinear optics" was introduced by Schrödinger in 1942 [7–9]. However, it was not until the observation of second harmonic generation (SHG) in quartz by Franken in 1961, that frequency con-

version using nonlinear optics was first demonstrated [10]. The theory of parametric electromagnetic interactions was expanded by Armstrong *et al* in 1962, revealing that by exploiting the concept of phase-matching in a nonlinear medium, light could be converted from common laser emission wavelengths to new wavelengths [11]. Intense phase-matched SHG was demonstrated soon after, with difference-frequency-generation (DFG) reported in 1963, and finally the first optical parametric oscillator (OPO) was demonstrated by Giordmaine and Miller in 1965 [12–14].

The OPO represented an important breakthrough, as a single device able to generate coherent light with a variable wavelength, in spectral regions inaccessible to conventional lasers. Based on a $LiNbO_3$ crystal, and pumped with the second harmonic of an Nd:CaWO4 nanosecond laser at 529 nm, oscillation was observed at a threshold pump power of 6.7 kW. Despite this impressive early progress, translating OPOs to other wavelengths and timescales (continuous wave (CW), and ultrashort pulses (picosecond to femtosecond)) proved challenging. This was mainly due to sluggish development of reliable high-power lasers, crystals with poor linear and nonlinear optical properties, and low-quality optical coatings. Sporadic reports continued throughout the late 1960s and 1970s, including first CW OPO in 1968, and the first synchronously-pumped picosecond OPO in 1977, however OPOs still remained far from a practical and widespread technology [15, 16].

The period of stagnation came to an end with the achievement of femtosecond pulse generation by passive Kerr-lens mode-locking [17, 18]. Exploiting this principle, laser oscillators were able to provide the high peak intensities required to perform efficient frequency conversion, with only modest average power. Moreover, the ability to generate ultrashort pulse trains at high repetition rates (~80–100 MHz) presented great improvements in the signal-to-noise ratio for experiments. The first femtosecond OPO was reported in 1989 by Edelstein *et al*, and was based on a $KTiOPO_4$ crystal pumped internal to a mode-locked dye laser cavity in a complex non-collinear arrangement [19]. The successful engineering of periodically-poled nonlinear crystals boosted the magnitude of available

effective nonlinearity, enabled collinear pumping, and created a new convenient method with which to tune the output wavelength [20]. Nonlinear optics entered a new golden age, with numerous demonstrations of high-power, high-repetition-rate femtosecond OPOs in the near-IR, and the first commercial systems began to hit the market [21–23].

With technology now established, attention turned to conquering the most barren areas of the optical spectrum; the ultraviolet, visible and mid-IR regions. By the mid 2000s, devices tunable in the ultraviolet and the entire visible range had been reported, utilising frequency doubling of a Ti:sapphire laser to pump in the blue [24, 25]. The deep mid-IR was reached by means of cascaded pumping from now established near-IR OPOs [26]. The successful development of new semiconductor and non-oxide nonlinear crystals with favourable transmission and nonlinear properties has allowed deep mid-IR femtosecond pulses to be generated up to 12 μm in a single frequency conversion stage, using fixed wavelength ytterbium (Yb)-doped lasers near 1 μm [27, 28]. Performing DFG between signal and idler pulses has extended tunability up to 20 μm [29]. Recent landmark achievements utilising OPOs include generation of optical frequency combs, computational networking, and random quasi-phase-matching [30–32].

In spite of growing competition from supercontinuum and quantum cascade lasers (QCLs), OPOs remain indispensable laboratory tools, and the gold-standard light source for applications in the femtosecond regime [33]. Figure 1.2 illustrates how frequency conversion sources offer a unique combination of high power, relative compactness, and broad spectral coverage. However, an unfortunate drawback is that OPOs remain, in general, costly devices and often require technical knowledge to operate optimally. For the end-user this presents a intimidating investment, and subsequently a cheaper alternative may be chosen, with some compromise made in power or spectral coverage. Cost and complexity scales dramatically with each frequency conversion stage, therefore a single-crystal arrangement is always preferred. This presents challenges due to the highest power pump lasers being the Ti:sapphire and Yb-based systems at 0.7–1.04

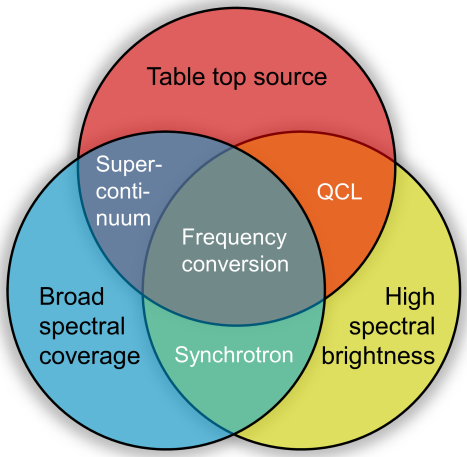

Figure 1.2: Competing coherent sources.

μm. Unfortunately, most nonlinear crystals which have favourable properties in the mid-IR, suffer from detrimental linear and nonlinear absorption at these wavelengths, and require pump wavelengths >2 μm. On the other hand, producing tunable light in the UV and visible inevitably requires an upconversion stage, in the form of internal or external frequency doubling. However, high quality commercially available crystals, such as β-BaB_2O_4 (BBO) and BiB_3O_6 (BIBO) ensure that conversion efficiency remains high and automated commercial systems now exist [34].

Figure 1.3 shows a chart of nonlinear crystals across the near-IR to deep mid-IR spectral region, where most ongoing research is currently focused (data taken from [35]). The x-axis is the practical transmission range, considering two-photon and multiphoton absorption at short wavelengths, and the y-axis is the figure-of-merit (FoM) of the crystal, a factor proportional to parametric gain. Also marked by the vertical dotted line is the upper emission limit for widely available commercial femtosecond laser oscillators. The dashed lines represent new crystals under development, such as the promising $BaGa_2GeSe_6$ (BGGSe), and crystals with limited

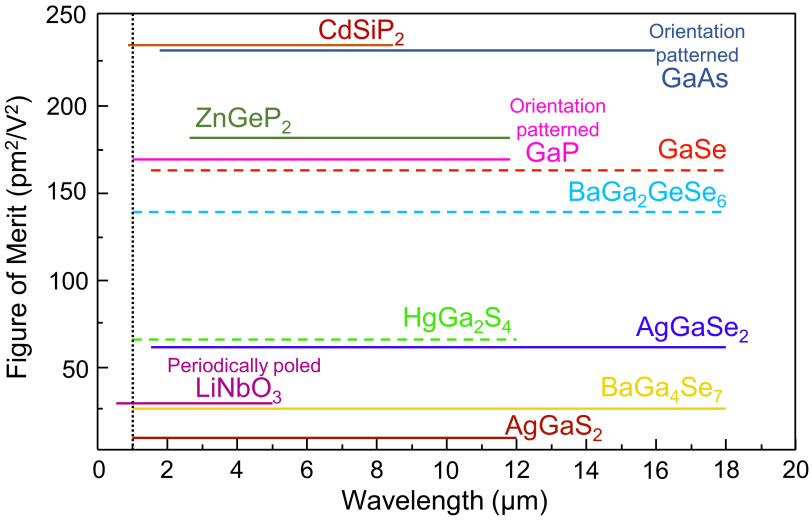

Figure 1.3: Transparency ranges of different infrared nonlinear crystals, and their respective figures of merit. Dashed lines indicate crystals which are not widely available, or still under active development. The vertical dotted line marks the key 1 μm wavelength, where the most established high power lasers emit.

availability (HGS) or poor physical properties (GaSe). It can be seen that only a few crystals have transmission from the dotted line to beyond 5 μm. Of those which do, the two with the highest FoM were only recently developed, with the intention of addressing this issue; $CdSiP_2$ (CSP), and orientation-patterned GaP (OP-GaP) [36, 37]. These crystals have facilitated the generation of deep mid-IR radiation from the near-IR in a single frequency conversion step.

1.2 Overview

This thesis consists of synchronously-pumped femtosecond OPOs operating across the infrared spectral region, in the range 1–8.4 μm. Figure 1.4 presents the overview, with two main research thrusts. In the near- and mid-IR (0.7–5 μm), novel systems are reported which offer significant technological improvements over existing designs, in terms of stability, compactness and efficiency. The performance characteristics are extensively studied and reproduced, using simulations and calculations based on nonlinear optical theory. Furthermore, direct generation of macroscopic deep mid-infrared (>5 μm) radiation from a Ti:sapphire laser is presented for the first time, reducing the cost and complexity associated with existing cascaded sources.

All works are based on the ubiquitous 80 MHz Ti:sapphire laser, which is still the most prevalent femtosecond laser system, due to its clean transform-limited pulses (as short as a few fs) and wide tunability.

Chapter 2 contains an overview of the core concepts in nonlinear optics, which form the basis for parametric wave interactions and frequency conversion. This includes an introduction to phase-matching, derivation of the coupled-amplitude equations, and optical parametric oscillation.

Chapter 3 is a summary of the essential design considerations required to build practical frequency conversion system, in the form of an OPO. Ultrafast physical phenomena such as group-velocity-mismatch, dispersion and $\chi^{(3)}$ nonlinear effects, together with practical issues such as resonator configuration, are discussed.

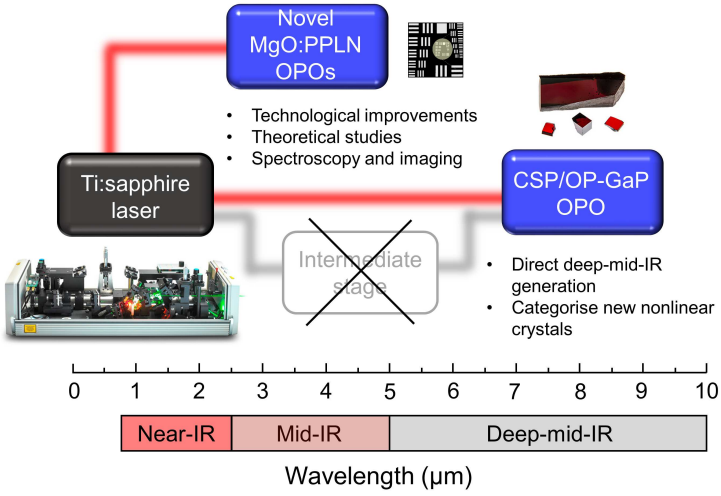

Figure 1.4: Outline of the thesis.

Chapter 4 describes an OPO configured in a fibre-feedback cavity, which produces up to 110 mW of average power in 100 fs pulses tunable across 1051–1700 nm in the near-IR. The use of an optical fibre as part of the cavity enables a design which is compact, cost-effective, and extremely stable to cavity length perturbations. Multiple novel effects, including soliton formation, and a new type of spectral sideband, are observed and explained using detailed simulations.

In chapter 5, an efficient low-threshold mid-IR OPO source across 3132–4273 nm is reported, where a tunable pump laser near 1 μm enables group-velocity matching to be achieved between pump and idler pulses, facilitating the use of a long (42 mm) MgO:PPLN crystal, for the first time in a femtosecond device. Up to 65 mW of mid-IR average power is generated from a pump power of 420 mW, equivalent to a quantum conversion efficiency of 48%. Furthermore, IR transmission spectroscopy of methane is performed, around the absorption peak at 3.3 μm.

In chapter 6, a deep mid-IR OPO based on CSP is presented, for the first time using a Ti:sapphire laser as the direct pump source. The OPO

produced up to 20 mW of average power in the challenging and important spectral region from 6.6–8.4 μm in pulses estimated to be 300 fs in duration. The challenges associated with pumping CSP at a wavelength <1 μm are also discussed.

Finally, chapter 7 provides a summary and a discussion of relevant applications. This includes a collaborative project where mid-IR upconversion imaging was performed using a femtosecond OPO. Future directions and ongoing research into infrared OPOs are also examined.

2 Basics of Nonlinear Optics

2.1 Optical nonlinearity

Everyday life takes place in the linear regime of optics. The effects we observe on a daily basis, such as reflection, refraction, dispersion and diffraction, are the result of low-intensity light-matter interactions. When a small amplitude electromagnetic wave propagates through a medium, the relationship between the electric field, $\mathbf{E}(t)$, and the induced polarisation, $\mathbf{P}(t)$, is approximately linear

$$\mathbf{P}^L = \varepsilon_0 \chi^{(1)} \mathbf{E} \tag{2.1}$$

where ε_0 is the permittivity of free space, and $\chi^{(1)}$ is the linear electric susceptibility tensor with components dependent on frequency ω and other material properties. As the name implies, nonlinear optics refers to the optical regime where this linear model begins to break down. Under the influence of intense light, electron clouds become displaced about their host atom, and the total dipole moment acquires a nonlinear dependence on applied electric field, as illustrated in Figure 2.1 [38]. The unprecedentedly high electric fields generated by the first lasers offered physicists the first opportunity to experiment in this field, which was until then poorly understood. A general expression for the total induced polarisation is given by a power series in electric field [39]

$$\mathbf{P} = \varepsilon_0 (\chi^{(1)} \mathbf{E} + \chi^{(2)} \mathbf{E}^2 + \chi^{(3)} \mathbf{E}^3 + ...) \tag{2.2}$$

where $\chi^{(2)}$and $\chi^{(3)}$ represent the second and third order nonlinear susceptibility tensors. Whereas the linear polarisation oscillates with the optical frequency of the input wave, higher-order terms are responsible for the generation of new oscillation frequencies [40]. The exciting potential of this phenomenon, and the diversity of possible applications, ensured that breakthroughs came thick and fast in the immediate years following the invention of the laser. Second order nonlinear optical effects

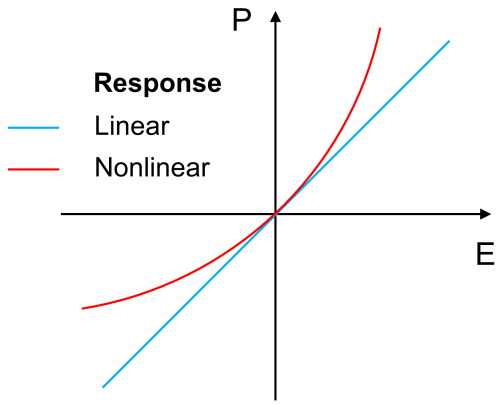

Figure 2.1: Polarisation response in the linear (blue) and nonlinear (red) optical regimes.

include second-harmonic-generation (SHG), difference-frequency generation (DFG), and optical parametric generation (OPG), while third order processes include the Kerr effect, self-phase-modulation (SPM), and four-wave-mixing (FWM). The work in this thesis is primarly concerned with $\chi^{(2)}$ nonlinearity, with third order effects playing a smaller but still significant role.

2.2 Second order nonlinear processes

In constrast to linear optics, in the nonlinear regime it is possible for electromagnetic waves of equal or different frequencies to interact with each other, while propagating through a medium. If the order of nonlinear interaction is given by n, then the number of interacting waves is $n+1$, implying that second order processes involve 3 waves. This can be shown by considering an electric field with two frequency components at ω_1 and ω_2, and the expression for second-order nonlinear polarisation, given by the second term in equation (2.2)

$$\mathbf{E}(t) = \mathbf{E}_1(t)e^{-i\omega_1 t} + \mathbf{E}_2(t)e^{-i\omega_2 t} + cc. \tag{2.3}$$

$$P^{NL} = \varepsilon_0 \chi^{(2)} \mathbf{E} \cdot \mathbf{E} \tag{2.4}$$

Substituting equation (2.3) into equation (2.4) yields the generated nonlinear polarisation, which can be expressed as a sum of frequency components

$$P^{NL} = \sum_{n=1,2} P(\omega_n) e^{-i\omega_n t} = \varepsilon_0 \chi^{(2)} (\mathbf{E}_1 \cdot \mathbf{E}_1 e^{-2i\omega_1 t} + \mathbf{E}_2 \cdot \mathbf{E}_2 e^{-2i\omega_2 t} + 2\mathbf{E}_1 \cdot \mathbf{E}_2 e^{-i(\omega_1+\omega_2)t} + 2\mathbf{E}_1 \cdot \mathbf{E}_2^* e^{-i(\omega_1-\omega_2)t} + cc) + 2\varepsilon_0 \chi^{(2)} (|E_1|^2 + |E_2|^2) \tag{2.5}$$

It can be seen that the exponents of the first two terms of equation (2.5) are proportional to twice the input frequencies, while the third and fourth are proportional to the sum and difference respectively. Physically, these represent the phenomena of second-harmonic-generation (SHG), sumfrequency-generation (SFG), and difference-frequency-generation (DFG). The final term is related to optical rectification, which will not be discussed in this work. In each process, both energy and momentum are conserved. For example, during SHG two photons of frequency, ω, combine to produce a single photon at 2ω, while DFG involves two input photons at ω_1 and ω_2 generating a third photon with frequency $\omega_3 = \omega_1 - \omega_2$, and for SFG the output photon has $\omega_3 = \omega_1 + \omega_2$. SHG is the degenerate case of SFG. The two conservation laws are expressed as

$$\omega_1 = \omega_2 + \omega_3 \tag{2.6}$$

$$k_1 = k_2 + k_3 \tag{2.7}$$

where $k_i = \frac{n(\omega_i)\omega_i}{c}$ are the respective wavevectors, and $n(\omega)$ is the frequency dependent refractive index. Equation (2.7) is often referred to as the *phase-matching* condition. An interesting corollary of equation (2.5) is that an input photon at ω_1 can spontaneously generate two photons at ω_2 and ω_3, in a process analytically identical to DFG. In the field of quantum optics, this is known as spontaneous parametric down conversion (SPDC),

however throughout this thesis it will be referred to as optical parametric generation (OPG). By convention, of the two generated photons, the one with higher frequency is termed the *signal*, and the one with lower frequency the *idler*. The term *parametric* in this case signifies that inital and final quantum states are identical [41]. For weak laser beams the OPG process is very inefficient, and only a small amount of parametric fluorescence is observed. Placing the crystal inside a Fabry-Perot resonator, consisting of mirrors coated for high reflection at the signal or idler wavelength, can greatly enhance the fluorescence intensity until a large fraction of the input photons are down-converted to signal and idler photons. This configuration is known as an optical parametric oscillator (OPO), which provides an efficient method of producing new frequencies from a single input beam [42]. For lasers operating in pulsed mode with very high pulse energies (μJ to mJ), efficient OPG can be achieved in a single pass through a nonlinear medium without requiring a resonator. However, under most circumstances, light that is continuous-wave (CW) or quasi-continuous-wave (quasi-CW, e.g. nJ pulses in a pulse train at 100 MHz) requires feedback in order to stimulate macroscopic conversion. Figure 2.2 shows a representative schematic of each process, where $\omega_1 > \omega_2 > \omega_3$.

2.3 Second order nonlinear susceptibility

Nonlinear interactions typically take place in a crystalline medium. The geometrical properties of crystals give rise to axes of symmetry, which determine the form of the susceptibility tensor, and can lead to the reduction in non-zero elements. If a crystal is centrosymmetric, i.e. its structure is invariant under a parity transformation about an inversion centre, then all tensor coefficients can vanish [43]. This can be proven by considering the second-order polarisation generated by two electric fields of the form $\mathbf{E}(t) = E(t)\hat{\mathbf{z}}$ applied in the forward (+) and reverse (-) direction

$$\mathbf{P}^{NL} = \varepsilon_0 \chi^{(2)} \mathbf{E}_1 \cdot \mathbf{E}_2 = \varepsilon_0 \chi^{(2)} E_1(t) E_2(t) \hat{\mathbf{z}} \tag{2.8}$$

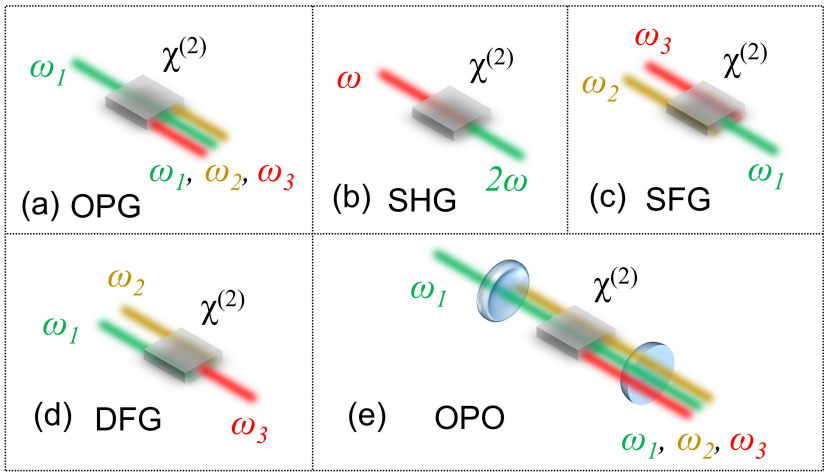

Figure 2.2: Second order nonlinear processes.

$$\mathbf{P}^{NL} = \varepsilon_0 \chi^{(2)}(-\mathbf{E}_1) \cdot (-\mathbf{E}_2) = \varepsilon_0 \chi^{(2)} E_1(t) E_2(t) \hat{\mathbf{z}} \tag{2.9}$$

Centrosymmetry implies that the polarisation must always have the same sign as the applied field, meaning that the only scenario where equations (2.8) and (2.9) make physical sense is when $\chi^{(2)} = 0$. Since a significant fraction of common media exhibit centrosymmetry, e.g. liquids, gases, glasses and some crystals, this represents the first important selection rule for second-order nonlinear effects. A comprehensive summary of all non-centrosymmetric crystal groups can be found in [44]. In order to absorb factors of $1/2$, which arise when evaluating $\mathbf{P}^{NL}$,the susceptibility tensor is redefined as

$$d_{ijk} = \frac{1}{2}\chi^{(2)}_{ijk} \tag{2.10}$$

where the indicies i, j, k represent the three spatial coordinates x, y, z. Typically the interacting waves are well within the transparency range of the medium, meaning that optical frequencies are far from any resonant frequencies. This enables Kleimann symmetry to be applied, which states that the elements of d_{ijk} are independent of frequency, are independent of frequency, and also results in the equivalence of several elements [45].

ij	11	22	33	23, 32	13, 31	12, 21
m	1	2	3	4	5	6

Table 2.1: d_{ijk} contraction

Subsequently, d_{ijk} can be reduced from a 27 element tensor to a 3×6 matrix d_{im} using the notation in Table 2.1 such that the second order nonlinear polarisation can be expressed as

$$\begin{pmatrix} P_x(\omega_3) \\ P_y(\omega_3) \\ P_z(\omega_3) \end{pmatrix} = \begin{bmatrix} d_{11} & d_{12} & d_{13} & d_{14} & d_{15} & d_{16} \\ d_{21} & d_{22} & d_{23} & d_{24} & d_{25} & d_{26} \\ d_{31} & d_{32} & d_{33} & d_{34} & d_{35} & d_{36} \end{bmatrix} \begin{pmatrix} E_x(\omega_1)E_x(\omega_2) \\ E_y(\omega_1)E_y(\omega_2) \\ E_z(\omega_1)E_z(\omega_2) \\ E_y(\omega_1)E_z(\omega_2) + E_z(\omega_1)E_y(\omega_2) \\ E_x(\omega_1)E_z(\omega_2) + E_z(\omega_1)E_x(\omega_2) \\ E_x(\omega_1)E_y(\omega_2) + E_y(\omega_1)E_x(\omega_2) \end{pmatrix} \tag{2.11}$$

Depending on the crystal class, several axes of symmetry can arise, which means that many of the matrix elements are zero or identical to others, or equal and opposite to another element.For example, the d_{im} matrix for lithium niobate ($LiNbO_3$), a birefringent crystal with point group 3m, is given by [46]

$$d_{im} = \begin{bmatrix} 0 & 0 & 0 & 0 & d_{31} & -d_{22} \\ -d_{22} & d_{22} & 0 & d_{31} & 0 & 0 \\ d_{31} & d_{31} & d_{33} & 0 & 0 & 0 \end{bmatrix} \tag{2.12}$$

where the magnitudes of individual elements are expressed in units pm/V to provide convenient notation. Here, $d_{22} = 2.4$ pm/V, $d_{31} = -4.4$ pm/V and $d_{33} = 25$ pm/V. The efficiency of a nonlinear interaction is dependent on the magnitude of the input electric fields, and the effective value of

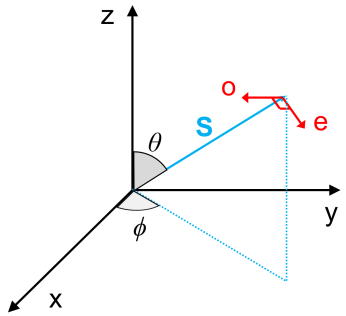

Figure 2.3: Coordinate system for calculating effective nonlinearity

	E_x	E_y	E_z
$\omega\ (e)$	$\|E(\omega)\|cos(\theta)\,cos(\phi)$	$\|E(\omega)\|cos(\theta)\,sin(\phi)$	$-\|E(\omega)\|sin(\theta)$
$2\omega\ (o)$	$\|E(2\omega)\|sin(\phi)$	$-\|E(2\omega)\|cos(\phi)$	0

Table 2.2: Electric field components for the fundamental and second harmonic beams in an SHG interaction.

nonlinearity experienced by the waves. The effective nonlinear coefficient d_{eff} is dependent on

- The direction in which the waves pass through the crystal (Poynting vector)
- The polarisation of the waves
- The tensor elements of d_{im}

Consider an SHG interaction in $LiNbO_3$, a birefringent crystal, where the fundamental input beam at ω is extraordinarily polarised with respect to the optic axis, and the second harmonic is ordinarily polarised. The electric field components can be resolved along the crystal axes, as shown in Figure 2.3, and are summarised in Table 2.2. Then, by evaluating equation (2.11) and simplifying terms, it is found that the effective second order nonlinear polarisation and resultant d_{eff} can be expressed as

$$P_{eff}(2\omega) = \varepsilon_0 \left(d_{31} sin\left(\theta\right) - d_{22} cos\left(\theta\right) sin\left(3\phi\right)\right) \left|E\left(\omega\right)\right|^2 \tag{2.13}$$

$$d_{eff} = d_{31} sin\left(\theta\right) - d_{22} cos\left(\theta\right) sin\left(3\phi\right) \tag{2.14}$$

It is observed that in this case the effective nonlinear coefficient does not contain the highest value matrix element, d_{33}, highlighting the importance of choosing the optimum polarisation for the interacting wave. In many cases, it is not possible to access the largest coefficient in a bulk crystal, due to limitations described in section 2.5.

2.4 Coupled wave equations in second order nonlinear optics

Until now, it has been discussed how intense electric fields can interact in a non-centrosymmetric medium and generate a polarisation field containing new frequencies, which in turn provides a source for new frequencies in the electric field. In order to explore the energy flow between all electric field components at different frequencies, it is necessary to solve Maxwell's equations [41]. The analysis can be greatly simplified by making the following assumptions:

- The nonlinear material is transparent for all waves involved
- The medium is non-conducting and non-magnetic
- $\chi^{(2)}$ is the dominant nonlinear term
- Anisotropy of the material is neglected

Maxwell's equations can then be expressed as

$$\nabla \times \mathbf{H} = \frac{\partial \mathbf{D}}{\partial t} \tag{2.15}$$

$$\nabla \times \mathbf{E} = -\frac{\partial \mathbf{B}}{\partial t} \tag{2.16}$$

$$\nabla \cdot \mathbf{E} = 0 \tag{2.17}$$

where the electric displacement field $\mathbf{D}$ can be written in terms of the polarisation, $\mathbf{D} = \varepsilon_0\mathbf{E} + \mathbf{P} = \varepsilon_0\mathbf{E} + \varepsilon_0\chi^{(1)}\mathbf{E} + \mathbf{P}^{NL}$, and the magnetic flux density $\mathbf{B}$ can be written in terms of the magnetic intensity field, $\mathbf{B} = \mu\mathbf{H}$, where μ is the magnetic permeability.

Differentiating (2.15), followed by substituting eqautions (2.16) and (2.17), and using a suitable vector identity, yields a wave equation which describes the evolution of the electric fields as they propagate through the nonlinear medium

$$\nabla^2\mathbf{E} = \frac{1}{c^2}\frac{\partial^2\mathbf{E}}{\partial t^2} + \frac{1}{\varepsilon_0 c^2}\frac{\partial^2\mathbf{P}^{NL}}{\partial t^2} \tag{2.18}$$

The total electric field is assumed to consist of three interacting waves propagating along the same axis, with each taking the form

$$E_i(z,t) = \frac{1}{2}A_i(z)\left(e^{i(\omega_i t - k_i z)} + cc.\right) \tag{2.19}$$

where $A_i(z)$ are the field amplitudes as a function of distance. For input fields at ω_1 and ω_2, the nonlinear polarisation is calculated from equation (2.4), yielding

$$P_3^{NL}(z,t) = \frac{1}{2}P_3(z)\left(e^{i(\omega_3 t - k_3 z)} + cc.\right) \tag{2.20}$$

After subtituting equations (2.19) and (2.20) into equation (2.18), the result can be simplfied by invoking the Slowly Varying Envelope Approximation (SVEA), which states that if the distance over which the amplitude of the electric fields varies is small compared to the wavelength, then second order derivatives can be neglected

$$\left|\frac{\partial^2 A_i}{\partial z^2}\right| \ll \left|k_i\frac{\partial A_i}{\partial z}\right| \tag{2.21}$$

Repeating the analysis for the two other possible frequency interactions, $\omega_1 + \omega_3 = \omega_2$, and $\omega_2 + \omega_3 = \omega_1$, results in the three coupled amplitude equations for each interacting wave

$$\frac{\partial A_1}{\partial z} = \frac{id_{eff}\omega_1^2}{k_1 c^2} A_2^* A_3 e^{i\Delta kz} \tag{2.22}$$

$$\frac{\partial A_2}{\partial z} = \frac{id_{eff}\omega_2^2}{k_2 c^2} A_1^* A_3 e^{i\Delta kz} \tag{2.23}$$

$$\frac{\partial A_3}{\partial z} = \frac{id_{eff}\omega_3^2}{k_3 c^2} A_1 A_2 e^{-i\Delta kz} \tag{2.24}$$

where the phase mismatch, $\Delta k = k_3 - k_2 - k_1$ has been introduced. The work presented in this thesis is based upon the optical parametric generation (OPG) process, where the labels 3, 2 and 1 represent the pump, signal and idler frequencies respectively, such that $\omega_p = \omega_s + \omega_i$. As we are concerned with maximising the conversion efficiency from ω_p to ω_s and ω_i, it is of interest to know how the efficiency varies as a function of Δk. It can immediately be seen that if $\Delta k = 0$, then the amplitude of a given wave will grow linearly, assuming the other two remain constant. To find out how this changes for $\Delta k \neq 0$, the evolution of $A_1(z)$ over a nonlinear crystal of length L is considered. The final field intensity can be obtained by integrating equation (2.22) over the crystal length, for a fixed A_2 and A_3, a valid assumption for small fields

$$I_1 = \frac{8d_{eff}^2\omega_1^2 I_2 I_3}{n_1 n_2 n_3 \varepsilon_0 c^2} sinc^2\left(\frac{\Delta kL}{2}\right) \tag{2.25}$$

where the relation $I_i = 2n_i\varepsilon_0 c\,|A_i|^2$ has been used. Equation (2.25) shows that when $\Delta k = 0$, the output intensity increases quadratically, but for a finite phase mismatch it will oscillate between zero and a maximum value. The first minimum occurs after a propagation distance such that the argument is equal to π, allowing the coherence length to be defined

$$L_c = \frac{\pi}{\Delta k} \tag{2.26}$$

which illustrates the continual forward and backward flow of energy as the waves drift in and out of phase. The following section will discuss various practical methods of achieving phase-matching in an OPO.

2.5 Phase-matching

The phase-mismatch is determined by the value of the linear refractive index for the pump, signal and idler wavelengths, and thus depends on the dispersion profile of the medium

$$\Delta k = \frac{n_p\left(\lambda_p\right)}{\lambda_p} - \frac{n_s\left(\lambda_s\right)}{\lambda_s} - \frac{n_i\left(\lambda_i\right)}{\lambda_i} \tag{2.27}$$

where the wavelength dependent refractive index is usually empirically determined and given in the form of a Sellmeier equation. Since energy conservation is automatically assured in any parametric interaction, the set of signal and idler wavelengths which are generated from a given pump wavelength are those which satisfy the phase-matching condition, $\Delta k = 0$. It follows that if the refractive index can be altered by other means, e.g. by changing the temperature of the nonlinear crystal, then the generated signal and idler wavelengths will also change. The ability to tune the output wavelengths, often across a wide spectral range of several microns, is a key advantage of OPOs over other coherent sources. One popular method of controlling the phase-matching condition is to exploit the non-isotropic properties of birefringent crystals, referred to as *birefringent phase-matching*. Another approach, referred to as *quasi phase-matching*, is to engineer the nonlinear medium such that the sign of d_{eff} is switched at each coherence length, leading to continual flow of energy from the pump to the signal and idler waves.

2.5.1 Birefringent phase-matching

A crystal can be said to be non-isotropic if its refractive index varies along the direction of each orthogonal axis, expressed generally as $n_x \neq n_y \neq n_z$. If two of the directional components are equal, e.g $n_x = n_y \neq n_z$, then the crystal contains a single optic axis in the z-direction, such that a beam polarised in the xy plane will experience the same refractive index regardless of its propagation direction. This is termed the *ordinary* ray (*o*-ray), and its orthogonal counterpart is the *extraordinary* ray (*e*-ray). The effective value

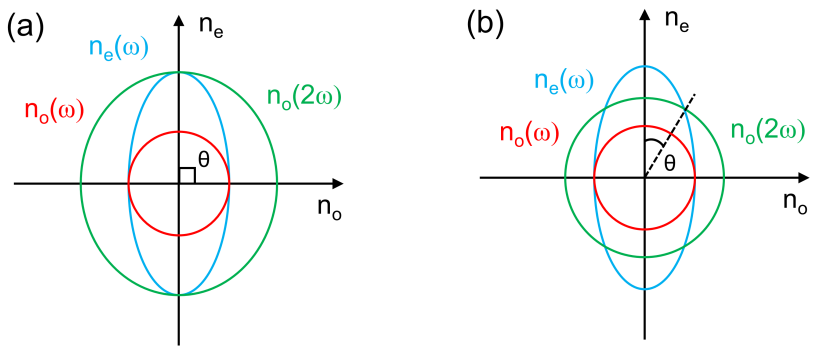

Figure 2.4: (a) Non-critical phase-matching (b) Critical phase-matching

of the refractive index experienced by the *e*-ray is dependent on the component of polarisation parallel to the optic axis, and is given by the index ellipsoid

$$\frac{1}{n_e^2(\theta)} = \frac{cos^2(\theta)}{n_o^2} + \frac{sin^2(\theta)}{n_e^2} \tag{2.28}$$

where θ is the angle between the *e*-ray polarisation and the optic axis, n_o is the ordinary refractive index, and $n_e = n_e(\theta = 0)$. If the polarisations of the interacting beams are chosen such that one or more propagate as the e-ray, then the angle θ can be adjusted until equation 2.27 is balanced, and phase-matching is achieved. This is visually represented in Figure 2.4 for an SHG interaction in a positively birefringent crystal, wherein case (a) has the phase-matching angle at $\theta = 90°$ and case (b) $0 < \theta < 90°$. The former case is known as non-critical phase-matching, as approximate phase-matching can be sustained over a larger deviation from the precise angle, compared to case (b), known as critical phase-matching.

The combination of polarisations determines the type of phase-matching, with the case for all beams of equal polarisation referred to by convention as type-0. Other possible combinations for the OPO process are listed in Table 2.3 [43].

A major drawback of critical phase-matching, is that for an e-ray prop-

Phase-matching type	Pump	Signal	Idler
0	*o*	*o*	*o*
	e	*e*	*e*
I	*e*	*o*	*o*
	o	*e*	*e*
II	*e*	*o*	*e*
	o	*o*	*e*
	e	*e*	*o*
	o	*e*	*o*

Table 2.3: Different phase-matching combinations for the OPO process.

agating in a non isotropic crystal, the flow of optical intensity, defined by the Poynting vector, will start to diverge from the direction of the k vector (direction of the wavefront). Over the length of a nonlinear crystal, this spatial walk off can be large enough that beam overlap is lost after a certain distance, reducing the effective interaction length. The walk-off angle ρ can be calculated using the equation

$$\rho = tan^{-1}\left(\frac{1}{n_e(\theta)}\frac{\partial n_e(\theta)}{\partial\theta}\right) = tan^{-1}\left(-\frac{1}{2}\left|n_e(\theta)\right|^2\left(\frac{1}{n_e^2}-\frac{1}{n_o^2}\right)sin(2\theta)\right) \quad (2.29)$$

and the effective interaction length, or aperture length L_a, is defined as

$$L_a = \frac{\sqrt{\pi}w_0}{\rho} \quad (2.30)$$

where w_0 is the beam waist radius at the focus in the crystal. Since w_0 can be as small as 10 μm, even a small walk-off angle of 5 mrad can lead to walk-off after a few mm of propagation, greatly reducing the available nonlinear gain in a parametric interaction. However it can be seen from equation 2.29, that ρ vanishes under non-critical phase-matching ($\theta = 90$), ensuring complete spatial overlap over the entire crystal length.

2.5.2 Quasi-phase-matching

A limitation of birefringent phase-matching is inflexibility in the choice of polarisations for the interacting waves, often leading to a d_{eff} much smaller than the theoretical maximum. For example, in achieving type-I phase matching in $LiNbO_3$, the resultant effective nonlinearity is only contributed to by the $d_{31} = 4.4$ pm/V tensor element. Furthermore, non-critical phase-matching is often impossible, increasing the threshold for parametric processes. An alternative solution, known as quasi-phase-matching (QPM), is to modulate the sign of d_{eff}, with a period Λ corresponding to twice the coherence length of the crystal, which applies a π phase shift to the electric fields and restores phase-matching [47, 48]. The major advantage of QPM, is that appropriate choice of the modulation period permits all three interacting waves to have the same polarisation (type-0 phase-matching), which can be chosen to match the direction of the largest tensor coefficient of d_{im}. This ensures the absence of spatial walk-off under non-critical phase-matching. The creation of domains with alternating nonlinearity can be accomplished by two methods:

- Periodic poling: Relevant for ferroelectric materials such as $LiNbO_3$, $LiTaO_3$ and $KTiOPO_4$, an intense electric field is applied directly to the crystal using precisely patterned electrodes. When the applied field exceeds the coercive field (~ 21 kV/m for $LiNbO_3$), permanent domain reversal occurs and a grating structure is formed. Periodically poled crystals are denoted with the prefix *PP*.

- Orientation patterning: Used for non-ferroelectric semiconductor crystals with high nonlinearity but low anisotropy, such as GaAs and GaP. The grating structure is photolithographically patterned onto a bulk substrate, before an epitaxial growth technique such as hydride vapour phase expitaxy (HVPE) is used to vertically extend the grating layer over several hundred μm. Orientation patterned crystals are denoted with the prefix *OP*.

The phase-matching condition for quasi-phase matching is modified from

equation 2.27 to include the QPM grating wavevector

$$\Delta k = \frac{n_p\left(\lambda_p\right)}{\lambda_p} - \frac{n_s\left(\lambda_s\right)}{\lambda_s} - \frac{n_i\left(\lambda_i\right)}{\lambda_i} - \frac{1}{\Lambda} \tag{2.31}$$

where Λ takes typical values of $\sim$ 10 μm for wavelengths in the visible range, and $\sim$ 30 μm for the near and mid-infrared. Due to the increasing difficulty of creating a uniform grating structure towards shorter periods, material quality and domain purity tend to decrease with decreasing grating period. A potential option is to employ higher order quasi-phase matching, where the π phase shift is accumulated over a harmonic m of the grating period, however this method is seldom used, since the effective nonlinearity for QPM is determined by

$$d_{eff} = \frac{2}{m\pi} d_{im} \tag{2.32}$$

such that higher order QPM is associated with lower effective nonlinearity. Therefore, for first order QPM in periodically poled $LiNbO_3$, the highest effective nonlinearity is $d_{eff} = \frac{2}{\pi} d_{33} = 16$ pm/V, 4 times higher than achievable using birefringent phase-matching. Additionally, the grating period introduces another degree of freedom with which to tune to the generated wavelengths. For this reason, the crystal is often engineered in a fan structure with a continuously varying grating period along its aperture, as illustrated in Figure 2.5. By translating the crystal laterally, the grating period can be continually adjusted and rapid wavelength tuning is possible.

Figure 2.6 shows a comparison of the evolution of the intensity of interacting waves in a parametric interaction, for birefringent phase-matching (black) and quasi-phase matching (blue). The case of $\Delta k \neq 0$ is also shown in red for comparison. Although the intensity appears to grow much more rapidly for the birefringent case, a potentially higher value of d_{eff} for QPM means this method is usually more efficient.

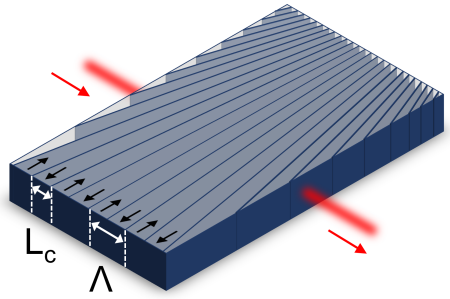

Figure 2.5: Quasi-phase matched nonlinear crystal with a fan-grating structure.

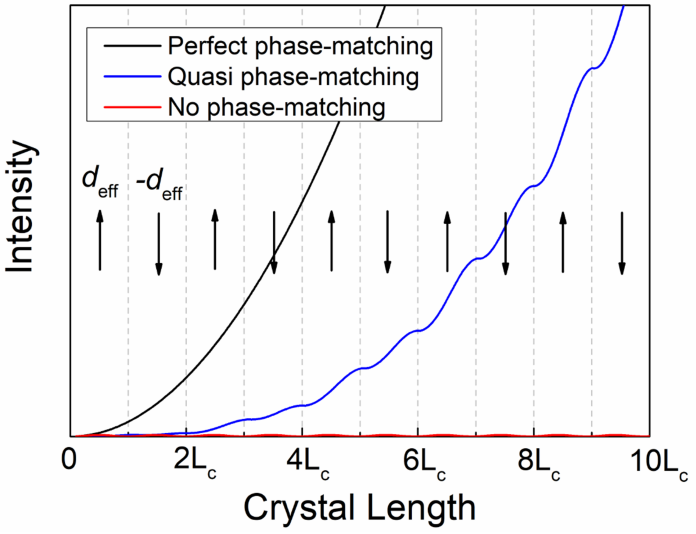

Figure 2.6: Intensity of output waves in a parametric interaction for perfect (birefringent) phase-matching in black, quasi-phase matching in blue, and no phase-matching in red.

2.6 Optical parametric oscillators

As briefly mentioned in section 1.2, an OPO is a device based on a nonlinear crystal contained within an optical resonator, which serves to amplify parametrically down-converted photons from quantum noise to macroscopic coherent beams. The source of pump photons is invariably another coherent beam, provided by a laser or another parametric source. Parametric processes are effectively instantaneous, and no energy is stored in the nonlinear crystal, and the temporal qualities of the pump beam are transferred to the signal and idler beams. This means a femtosecond pump source generates femtosecond signal and idler pulse trains. However, for femtosecond and picosecond duration pulses, the resonator round-trip time must be precisely matched to the temporal spacing of the pump pulses, in order to stimulate gain of the resonant pulses in each pass through the nonlinear crystal. Such an OPO is described as synchronously-pumped. For pulses of 100 fs duration, the synchronisation length is equal to 30 μm, highlighting the important of fine resonator length control. On the other hand, if the pump source is a nanosecond laser, then pulses are sufficiently long that the pump and signal/idler are always partially overlapped in the crystal [49]. In this case, the cavity is chosen to be as short as possible to maximise parametric gain by providing the highest number of round trips over the duration of the pump pulse. The work presented in this thesis is based on femtosecond synchronously-pumped OPOs, and analysis from this point forward will only consider the dynamics of these devices.

2.6.1 Femtosecond pump sources

A typical pump laser for femtosecond OPOs, and the source used for all experiments presented here, is the Kerr-lens mode-locked (KLM) Ti:Sapphire laser. A schematic of a modern commercial Ti:sapphire cavity design is presented in Figure 2.7. The crystal is pumped in the visible by a frequency-doubled diode-pumped solid-state laser at 532 nm, and cut at Brewster's angle to the incoming beam to ensure maximum absorption. The mode-

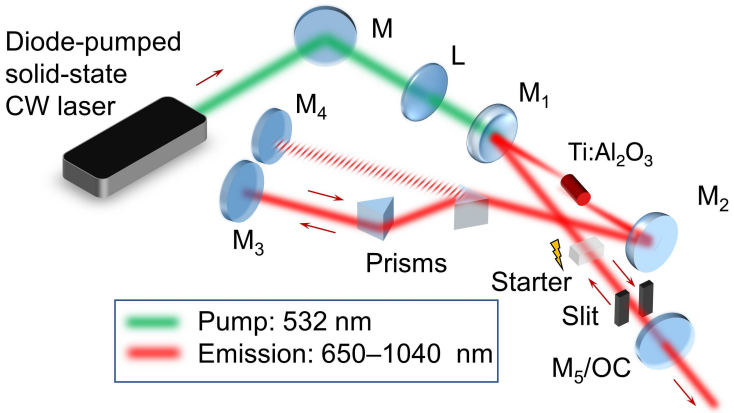

Figure 2.7: KLM Ti:sapphire cavity design.

locking procedure is based on the nonlinear Kerr effect, a $\chi^{(3)}$ process which acts to self-focus the most intense radiation, allowing the low-intensity fringes to be filtered by a physical aperture [18]. Pulsing is initiated by a piezo-controlled transparent element, which introduces rapid perturbations to the cavity length. Its emission bandwidth spans across 650–1040 nm, supporting the generation of pulses as short as a few femtoseconds with use of suitable dispersion management. An unchirped pulse from a Ti:sapphire laser has a $sech^2$ shape intensity profile in time. The laser used in this work produced 80–100 fs pulses at a repetition rate of 80 MHz, tunable across the entire emission range by means of an intracavity birefringent filter.

Alternative solid-state femtosecond lasers include those based on Yb doped crystals such as Yb:KGW, Yb:KYW and Yb:CALGO, and very high power thin-disk lasers based on Yb:YAG, which emit in the 1030–1060 nm region. In recent years, ultrafast fibre lasers have come to the fore as cheaper and more compact alternatives to the expensive Ti:sapphire laser. However, their lack of wavelength tunability and the instrinically chirped nature of their pulses, means they are yet to dislodge the Ti:sapphire as the gold standard femtosecond laser source.

2.6.2 Gain, amplification, and threshold

Like a laser, an OPO has a pump power threshold, above which runaway feedback leads to macroscopic growth of the signal and idler. Threshold is reached when the parametric gain experiences by the resonating wave(s) is equal to the round-trip losses due to absorption, reflection and output coupling. By applying appropriate dichroic coatings to the cavity mirrors, the OPO can be designed to resonate either a single wave (singly-resonant oscillator, SRO), two waves (doubly-resonant oscillator, DRO), or even all three (triply-resonant oscillator, TRO). Resonating more than one wave leads to a significantly lower threshold, for example, a femtosecond OPO can reduce its threshold from 940 mW average power in SRO configuration to 100 mW in DRO configuration [50]. However, resonating muliple waves introduces instability due to each wavelength having a different round trip time. Furthermore, controlled wavelength tuning in DRO operation is difficult, due to the device only operating at discrete resonances [51, 52]. All work presented in this thesis is based on SRO configuration, and the analysis will only consider this case. The coupled wave equations (2.22-2.24) can be solved for an OPO interaction in a crystal of length L, under the assumption that the pump wave A_p does not significantly deplete as it propagates through the nonlinear medium. The signal and idler fields at the crystal end can be expressed as [41]

$$A_s(L) = [A_s(0)\left(cosh\,(gL) - \frac{i\Delta k}{2g} sinh\,(gL)\right) + \frac{i\omega_s^2 d_{eff} A_p}{g k_s c^2} A_i^*\,(0)\,sinh\,(gL)]e^{i\Delta kL/2} \quad (2.33)$$

$$A_i(L) = [A_i(0)\left(cosh\,(gL) - \frac{i\Delta k}{2g} sinh\,(gL)\right) + \frac{i\omega_i^2 d_{eff} A_p}{g k_i c^2} A_s^*\,(0)\,sinh\,(gL)]e^{i\Delta kL/2} \quad (2.34)$$

where the gain parameter, $g = \left(\Gamma^2 - (\Delta k/2)^2\right)$ has been introduced, and $\Gamma^2 = \frac{2\omega_s\omega_i d_{eff}^2}{\varepsilon_0 n_p n_s n_i c^3} I_p$, where the relation $I_p = \frac{1}{2}\varepsilon_0 c n_p \left|A_p\right|^2$, has been used. Here, the pump intensity I_p refers to the peak intensity, which is related to the average power, P_{av}, by

$$I_p = \frac{P_p^{av}}{\pi f_{rep} \tau_p w_0^2} \tag{2.35}$$

where f_{rep} is the laser repetition rate in Hz, τ_p is the full-width half-maximum (FWHM) pulse duration, and w_0 is the pump beam radius. Considering the boundary conditions, $A_s(0) = arbitrary$ and $A_i(0) = 0$, the incremental gain for the signal wave in a single crystal pass is given by [53]

$$G_s(L) = \frac{|A_s(L)|^2}{|A_s(0)|^2} - 1 = \Gamma^2 L^2 \frac{sinh^2(gL)}{g^2 L^2} \tag{2.36}$$

For a weak pump wave, such that $\Gamma^2 < (\Delta k/2)^2$, equation 2.36 can be reduced to

$$G_s(L) = \Gamma^2 L^2 sinc^2\left(g'L\right) \tag{2.37}$$

where $g' = \left((\Delta k/L)^2 - \Gamma^2\right)$, which shows that the signal field intensity will increase proportional to the square of the crystal length. In the high gain limit, $\Gamma^2 \gg (\Delta k/2)^2$, the incremental gain becomes

$$G_s(L) = \frac{1}{4} e^{2\Gamma L} \tag{2.38}$$

showing that for an intense pump there is an exponential gain in the output fields. Until now, all analysis has assumed that the pump, signal and idler take the form of plane waves, which is clearly an unphysical scenario [54]. Since a rigourous Gaussian beam treatment of the coupled amplitude equations is highly complex, several heuristic approaches have derived simplified expressions for the incremental gain in a synchronously-pumped OPO [55, 56] with focused Gaussian beams. Reference [57] de-

rives the following, for arbitrary focusing conditions,

$$G_s\left(L_{eff}\right) = \frac{128\pi^2 d_{eff}^2 L_{eff}}{n_p n_s \lambda_i^2 \lambda_s c\varepsilon_0} P_p g_t \xi_s Re\left(h_2\right) \tag{2.39}$$

where L_{eff} is the effective interaction length (the distance over which the pump and signal remain temporally overlapped), $g_t = \sqrt{\tau_p^2 / \left(\tau_p^2 + \tau_s^2\right)}$ is the temporal coupling factor, τ_s is the signal FWHM duration, $\xi_s = L\lambda_s / 2\pi n w_0^2$ is the signal focusing parameter, and $Re\left(h_2\right)$ is the real part of an integral over the crystal, defined in [55]. By setting this expression for gain equal to the fractional signal round-trip losses α_s, the threshold pump power can be expressed as

$$P_p^{th} = \frac{\alpha_s n_p n_s \lambda_i^2 \lambda_s c\varepsilon_0}{128\pi^2 d_{eff} L_{eff} g_t \xi_s Re\left(h_2\right)} \tag{2.40}$$

The above analysis is sufficient to derive the parametric gain close to the oscillation threshold, however, it implies that the signal and idler power continually increase upon each round trip. In reality, steady-state operation is reached when the pump wave begins to significantly deplete, leading to gain saturation. To account for this, the coupled-amplitude equations must be solved numerically.

2.6.3 Phase-matching bandwidth

The phase-matching bandwidth of a parametric process is determined by the FWHM of the $sinc^2\left(g'L\right)$ function in equation 2.37, and represents how much variation can be tolerated in a parameter which influences Δk, before the efficiency drops to half its maximum value. This occurs when the argument of 2.37 is equal to 0.4429π, therefore the FWHM is covered by $2\left(0.4429\pi\right)$. If the parametric gain is low, then 2.37 is simplified to $G_s\left(L\right) = \Gamma^2 L^2 sinc^2\left(\Delta k L/2\right)$, so that the phase matching bandwidth as a function of a single variable, X, can be determined by expanding Δk as a

Taylor series about the chosen parameter [43],

$$\Delta k = \Delta k_0 + \frac{\partial(\Delta k)}{\partial X}\Delta X + \frac{1}{2}\frac{\partial^2(\Delta k)}{\partial X^2}\Delta X^2 + ... \tag{2.41}$$

where X could be any of the input wavelengths, $\lambda_{p,s,i}$, the crystal temperature, T, or the phase-matching angle, θ, as just a few examples. An important parameter, particularly when dealing with femtosecond pulses, is the spectral phase-matching bandwidth for the pump beam, also known as the pump acceptance bandwidth. A transform limited 100 fs pulse, at central wavelength of $\lambda_p = 800$ nm, covers a large bandwidth of $\Delta\lambda_p = 6.7$ nm, and to achieve efficiency frequency conversion in an OPO it is essential that phase-matching is satisfied for all wavelength components. Since the second term in equation 2.41 generally dominates, the pump acceptance bandwidth can be derived by substituting 2.41 into the expression $\Delta kL/2 = 2(0.4429\pi)$, and evaluating the derivative for $X = \lambda_p$ and $\lambda_s = constant$,

$$\Delta\lambda_p^{acc} = \frac{5.56\lambda_p^2}{2\pi L}\left(n_p - n_i + \lambda_i\frac{\partial n_i}{\partial\lambda_i} - \lambda_p\frac{\partial n_p}{\partial\lambda_p}\right)^{-1} \tag{2.42}$$

The term in brackets is equal to the mismatch in group velocities between the pump and idler waves, showing that the pump acceptance bandwidth is larger when the pump and idler propagate at the same velocity in the crystal. It is also evident that $\Delta\lambda_p^{acc}$ is inversely proportional to the crystal length, with the consequence that shorter crystals are required to efficiently down-convert a broad bandwidth pump. Further details on the impact of this result are described in chapter 3. The analagous phase-matching bandwidths for λ_s and λ_i, are called the signal and idler parametric gain bandwidths, respectively, where the alternate terminology reflects that these quantities represent the range of signal and idler wavelengths which experience gain, for a given λ_p. The signal gain bandwidth is found to be

$$\Delta\lambda_s^{gain} = \frac{5.56\lambda_s^2}{2\pi L}\left(n_i - n_s + \lambda_s\frac{\partial n_s}{\partial\lambda_s} - \lambda_i\frac{\partial n_i}{\partial\lambda_i}\right)^{-1} \tag{2.43}$$

However, it is to be noted that these equations are only valid in the low gain (LG) limit, and assume that the fixed wavelength (signal in equation 2.42, pump in equation 2.43) is a delta function in frequency. Both of these assumptions are invalid for the high intensities and broad bandwidths associated with femtosecond pulses. The signal gain bandwidth in the high gain (HG) limit can be approximated by

$$\Delta\lambda_s^{HG} = \Delta\lambda_s^{LG}\sqrt{1 + \frac{\Gamma^2 L^2}{\pi^2}} \tag{2.44}$$

and a more accurate value can be obtained by integrating equation 2.44 over the experimentally measured pump spectral envelope. Therefore both high gain and finite pump bandwidth lead to a broadening of the signal gain bandwidth.

2.6.4 Wavelength tuning

The primary motivation for using an OPO as a light source is that the output wavelengths can be continuously tuned over an extremely wide range, by controlled variation of a parameter which influences the phase-matching condition. Once the dispersion relation and thermo-optic coefficients for a crystal are known, the desired signal and idler wavelengths can be generated to a very high degree of accuracy. For a simple synchronously-pumped cavity, comprising a resonator and a nonlinear crystal, wavelength tuning can be accomplished via

- Temperature tuning: Variation of the crystal temperature. Nonlinear crystals are often maintained at a high temperature to suppress photorefractive damage.
- Birefringent tuning: As described in section 2.5.1, phase-matching is satisfied at different wavelengths by rotating the crystal orientation with respect to the electric field polarisation.

- Quasi-phase-matched grating tuning: A crystal containing multiple grating periods can be translated laterally to change Λ, and thus the phase-matched wavelengths.
- Cavity length tuning: The resonant wavelength changes according to crystal dispersion to maintain synchronisation with pump pulses. Described in more detail in section 3.3.3.

A simple and convenient method to achieve wide wavelength coverage in the near- to mid-IR is to pump a mature QPM nonlinear crystal such as MgO:PPLN (periodically poled $LiNbO_3$ doped with MgO to increase its damage threshold) with a Ti:sapphire laser at $\lambda_p \sim 800$ nm, using type-0 non critical phase-matching ($e \rightarrow ee$) to access the highest nonlinear coefficient. If the crystal is engineered to contain a fan-grating structure, as shown in Figure 2.5, then gap-free tuning of the signal and idler wavelengths between $\sim$ 1–4 μm is possible [58]. Figure 2.8(a) shows the phase-matching efficiency $sinc^2(\Delta kL/2)$ for the signal/idler wavelengths in a 1-mm-long crystal as the grating period is varied across 19–22 μm. Also plotted in Figure 2.8(b) is the signal gain bandwidth $\Delta\lambda_s$ at $\Lambda = 20.5$ μm, which is a cross-section of Figure 2.8(a) along the y-direction.

Additionally, the tunability of the Ti:sapphire pump laser can be exploited to cover the same wavelength range using a single grating period, demonstrated in Figure 2.9(a) for $\Lambda = 20.5$ μm. This time the pump acceptance bandwidth is plotted in Figure 2.9(b) (note that this calculation is performed using the low gain approximation and a single frequency pump).

Similar tuning curves can be plotted for temperature variation, and angle tuning in birefringent crystals.

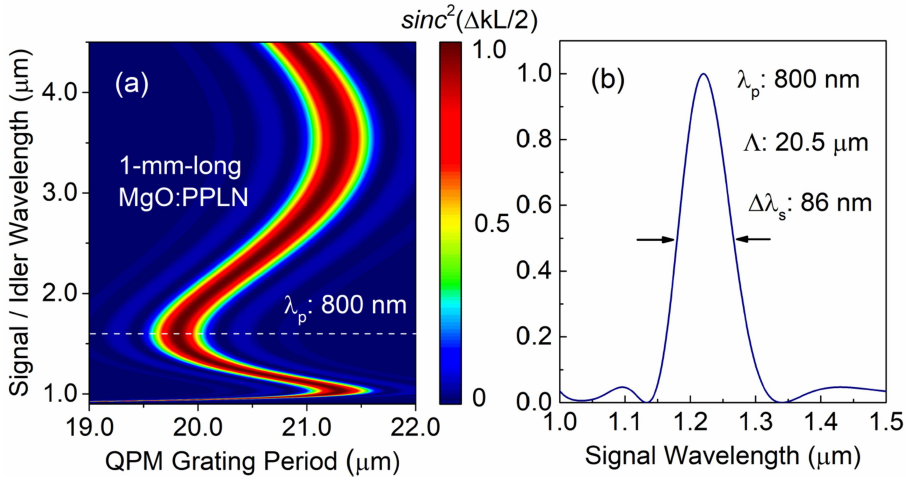

Figure 2.8: (a) QPM parametric gain efficiency for the signal and idler in a 1-mm-long MgO:PPLN crystal, at a pump wavelength of 800 nm. (b) Signal gain bandwidth evaluated at $\Lambda = 20.5$ μm.

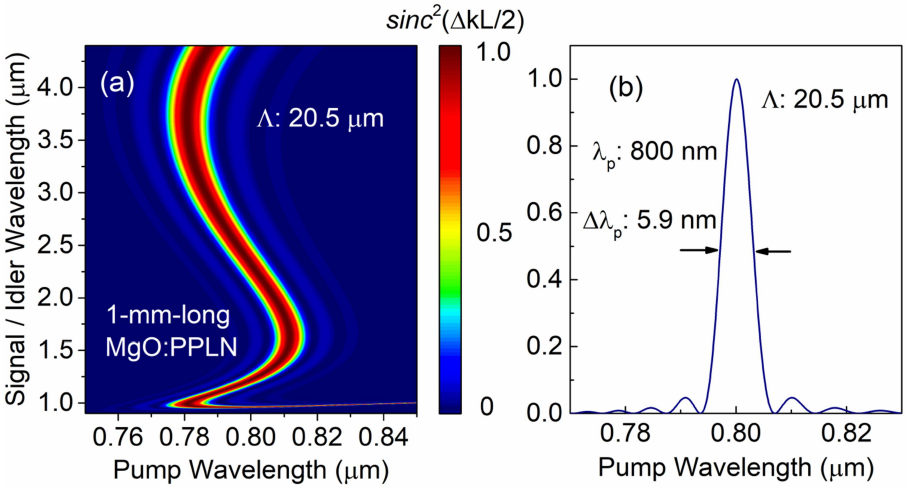

Figure 2.9: (a) Signal and idler parametric gain efficiency for pump tuning in a 1-mm-long MgO:PPLN crystal, at a fixed grating period of $\Lambda = 20.5$ μm. (b) Pump acceptance bandwidth evaluated at $\lambda_p = 800$ nm.

3 Femtosecond optical parametric oscillators

The previous section introduced the theory behind the generation of tunable light via frequency conversion in an OPO. In order to apply that theory to build a practical system, which operates with optimal efficiency and reliability, several important considerations must be made. In particular, synchronously-pumped femtosecond OPOs are especially sensitive to group velocity mismatch between the interacting waves, dispersion inside the cavity, and perturbations to the cavity length. The following section will detail how such physical phenomena influence the properties of the generated signal and idler pulses, and consequential design requirements.

3.1 Nonlinear material

Design of an OPO begins with selection of the parametric gain medium. For a material to be a strong candidate, the list of criteria which must be satisfied includes, but is not limited to

- Transparency at the desired pump, signal and idler wavelengths.
- Phase-matchability at the desired wavelengths, by means of birefringent, or quasi-phase-matching.
- Large variation in output wavelengths with a given quantity, such as phase-matching angle, temperature (preferable but not essential).
- High damage threshold, to withstand the high optical intensities at the beam foci.
- High *figure of merit*, defined as $FOM = \frac{d_{eff}^2}{n_p n_s n_i}$, a quantity proportional to the parametric gain, Γ.
- Low linear, and two-photon or multiphoton absorption.
- High thermal conductivity.

- Manufacturable to good optical quality (few defects and impurities).
- Low group-velocity mismatch between interacting waves to allow long interaction lengths for ultrafast femtosecond OPOs.
- Ideally, non-critical phase matching to eliminate spatial walk-off.

Depending on the desired output wavelengths, and the available pump sources, finding a suitable nonlinear medium to use can be straightforward or extremely challenging. For example, OPOs are well-matured in the visible and near- to mid-IR regions, due to the abundance of oxide-based nonlinear crystals with high nonlinearity and broad transmission windows, which extend to the pump wavelengths provided by high power mode-locked lasers, at 0.7–1 μm. However, the further the target wavelengths diverge from this point, the more the difficult performing efficiency frequency conversion becomes, especially in a single-stage process. To access the UV and deep-UV, a cascaded scheme of SHG is always required, with UV output powers ultimately diminishing to about an order of magnitude lower than the fundamental pump. Generating high power beyond $\sim$ 4.5 μm is an even greater task, due to limited availability of high-quality crystals with transmission extending from the near- to deep-IR. However, the recent development of $CdSiP_2$ (transparent over 1–8.5 μm) and OP-GaP (transparent over 1–12 μm) have gone some way to addressing this issue.

3.2 Damage threshold

To maximise parametric gain in a synchronously-pumped OPO, the interacting beams are focused to very small radii in the nonlinear crystal, introducing the risk of catastrophic material damage at high powers. In some cases, such as $AgGaS_2$, although sufficient parametric gain is available to surpass the oscillation threshold, poor thermal conductivity and linear absorption lead to permanent damage at high repetition rates [59]. Crystal manufacturers continually strive to improve growth procedures, as defects and impurities can lead to higher material absorption and increase

the likelihood of damage. The most mature crystals are often doped with additional compounds and maintained above room temperature (100–200°C) in order to increase their resistance to photorefractive damage [60]. MgO-doped periodically poled $LiNbO_3$ (MgO:PPLN) and $LiTaO_3$ (MgO:PPLT) can withstand intensities in excess of 10 GW/cm^2. Caution is often needed with newer crystals whose damage threshold is relatively untested, by using more loosely focused beams.

3.3 Dispersion and self-phase-modulation

3.3.1 Group-velocity mismatch

Once a suitable nonlinear crystal has been chosen, the first significant parameter to calculate is the rate at which temporal walk-off accumulates between the pump pulse and the resonating pulse inside the nonlinear crystal as a result of material dispersion, which is quantified by the group-velocity mismatch (GVM). Ultrashort pulses are represented in the frequency domain as a broadband wave-packet propagating at a common group velocity, given by

$$v_g\left(\lambda_0\right) = \frac{c}{n - \lambda_0 \frac{dn}{d\lambda}|_{\lambda_0}} \tag{3.1}$$

where λ_0 is the central, or carrier, wavelength. Since the pump, signal and idler all have different wavelengths in a non-degenerate OPO, the respective group velocities will differ, leading to loss of temporal overlap after a critical distance. The GVM between two pulses is defined as

$$GVM_{ij} = \frac{1}{v_{gi}} - \frac{1}{v_{gj}} = \frac{1}{c}\left(n_i - \lambda_i \frac{dn}{d\lambda_i} - n_j + \lambda_j \frac{dn}{d\lambda_j}\right) \tag{3.2}$$

which enables the effective temporal interaction length, L_{eff} , to be introduced

$$L_{eff}^{ij} = \frac{\Delta\tau}{GVM_{ij}} \tag{3.3}$$

Using this definition, the pump spectral acceptance bandwidth (equation 2.42) can be rewritten as

$$\Delta\lambda_p = \frac{5.56\lambda_p^2}{2\pi c(GVM_{pi})L} \tag{3.4}$$

Therefore, the consquence of GVM is to impose an upper limit on the single-pass parametric gain available in femtosecond OPOs, where wide spectral bandwidths can only be accommodated with short crystals (typically $\sim$ 1 mm for $\sim$ 100 fs pulses, but could be as short as $\sim$ 50 μm for few-cycle pulses).

3.3.2 Group velocity dispersion

For most applications employing femtosecond OPOs, such as frequency comb generation and ultrafast spectroscopy, it is desirable that the pulse duration remains as short as possible in order to support large instantaneous spectral bandwidths and maintain high temporal resolution. The wavelength dependence of group velocity infers that some wavelength components travel faster than others, leading to undesirable pulse broadening. Group velocity dispersion (GVD) is calculated using

$$GVD = \frac{d^2\omega}{dk^2} = \frac{\lambda_0^3}{2\pi c^2}\frac{d^2n}{d\lambda^2}|_{\lambda_0} \tag{3.5}$$

The GVD is also denoted as β_2, especially within the context of fibre optics. GVD is usually expressed in units fs^2/mm, and the total accumulated dispersion in a medium of length L is given by the group delay dispersion, $GDD = \beta_2 L$. Due to the large number of round trips in an OPO cavity, the effect of GVD on the resonant pulse can be quite dramatic, even for very short nonlinear crystals. The spatial evolution of the electric field of a pulse in the presence of GVD can be calculated by applying a phase-shift in the frequency domain proportional to the amount of dispersion [61]

$$E(z,t) = IFT\left[FT[E(0,t)]exp\left(\frac{i\omega^2\beta_2 z}{2} - i\omega t\right)\right] \tag{3.6}$$

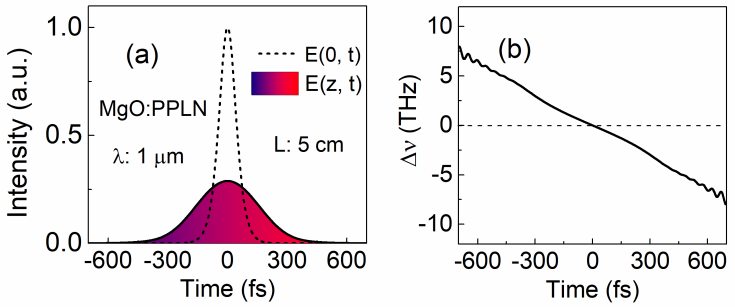

Figure 3.1: (a) An input 100 fs $sech^2$ pulse (dotted line) and the output (filled curve) after propagating through 5 cm of MgO:PPLN at 1 μm. (b) Instantaneous frequency variation across the final pulse.

where $E(0,t)$ is the initial electric field, z is the distance travelled, and FT/IFT represent the Fourier transform and inverse Fourier transform operations respectively. An example of a pulse at $\lambda = 1$ μm with an initial duration of 100 fs, and electric field, $E(z,t) = E_0(z)\, sech\left(\frac{1.763t}{\tau}\right)$, propagating through a 5-cm-long MgO:PPLN crystal, is shown in Figure 3.1(a). The initial pulse envelope $|E(z,0)|^2$ is represented by the dotted line, and the final pulse is the filled curve with a FWHM of $\sim$ 368 fs. Due to the positive GVD of MgO:PPLN at 1 μm, longer wavelengths travel faster and the wavelength varies as a function of time across the final pulse. The instantaneous frequency variation, defined by $\Delta\nu = -\frac{1}{2\pi}\frac{\partial\phi}{\partial t}$, where ϕ is the electric field phase, is plotted in Figure 3.1(b). It can be seen that the frequency/wavelength varies almost linearly with time, which is referred to as a linear chirp.

It is important to note that although the pulse has broadened in time, no new wavelengths are generated. However, a chirped pulse is more susceptible to spectral broadening via nonlinear effects, as described in the next section. Chirped pulses can be identified by measuring the product of the spectral bandwidth, $\Delta\nu$, and the pulse duration $\Delta\tau$ (time-bandwidth product). Unchirped pulses have a minimum value of the time-bandwidth product, which is limited by the uncertainty principle and depends on the

pulse shape. For $sech^2$ pulses, this is given by

$$\Delta\nu\Delta\tau \sim 0.315 \tag{3.7}$$

When this equality is satisfied, the pulse is said to be transform-limited.

3.3.3 Cavity length tuning

Dispersion in a synchronously-pumped OPO results in another method of tuning the output wavelengths. Due to the presence of the crystal in the cavity, each wavelength has a slightly different round trip time, with the oscillating wavelength being that which is exactly matched to the pump repetition rate. If the cavity length is slightly adjusted, then the wavelength matched to the new cavity length experiences gain instead. In femtosecond OPOs with short nonlinear crystals, a broad phase-matching bandwidth can allow tuning though a large wavelength range with little decrease in output power. The rate of change of wavelength with cavity length is related to the single-pass group delay dispersion by

$$\frac{d\lambda}{dL} = \frac{\lambda^2}{2\pi c^2 GDD} \tag{3.8}$$

Cavity length tuning provides a rapid and continuous method of covering spectral gaps that can appear in QPM based OPOs using discrete crystal grating periods.

3.3.4 Self-phase modulation

Focused beams in femtosecond OPOs are intense enough to stimulate additional nonlinear effects, which have their origin in the $\chi^{(3)}$ term of equation (2.2). The most apparent is self-phase modulation (SPM), a process which leads to spectral broadening in materials exhibiting third-order nonlinearity. The amount of SPM observed is dependent on the intensity of the input beam, and the magnitude of the nonlinear refractive index, defined as

$$n_2 = \frac{3}{8n} Re\left(\chi^{(3)}_{xxxx}\right) \tag{3.9}$$

where $\chi^{(3)}_{xxxx}$ is the tensor element of the third order nonlinear susceptibility corresponding to the electric field polarisation, and n is the linear refractive index. The effect of a non-zero value of n_2 is to introduce a nonlinear phase shift

$$\phi_{NL} = \frac{2\pi n_2 I(z,t)}{\lambda} z \tag{3.10}$$

where $I(z,t)$ is the beam intensity, and z is the distance travelled in the medium. The nonlinear phase shift is applied to the input field in the time domain, then a Fourier transform is performed to yield the final field in the frequency domain [61]

$$E(z,\omega) = FT\left[E(0,t)\, exp\left(i\phi_{NL}\right)\right] \tag{3.11}$$

An example of spectral broadening of a $sech^2$ pulse is shown in Figure 3.2, for a value of $\phi_{NL} = 4$. Such phase shifts are easily exceeded over many round trips in an OPO. It can be seen that a dramatic redistribution in spectral intensity has taken place and the pulse is no longer transform-limited.

3.3.5 Interaction between GVM, GVD and SPM

Realistically, neither dispersion nor nonlinearity can be treated as insignificant in a femtosecond OPO, and the two effects heavily influence each other. A pulse which has acquired chirp due to dispersion will experience greater SPM-induced spectral broadening than an unchirped pulse. As the intensity of the circulating pulse builds, it may experience distortion to its spatial and temporal profiles before it converges on a steady state. Correct treatment of femtosecond optical parametric oscillation requires the coupled wave equations to be modified to contain terms corresponding to GVM, GVD and SPM [62]

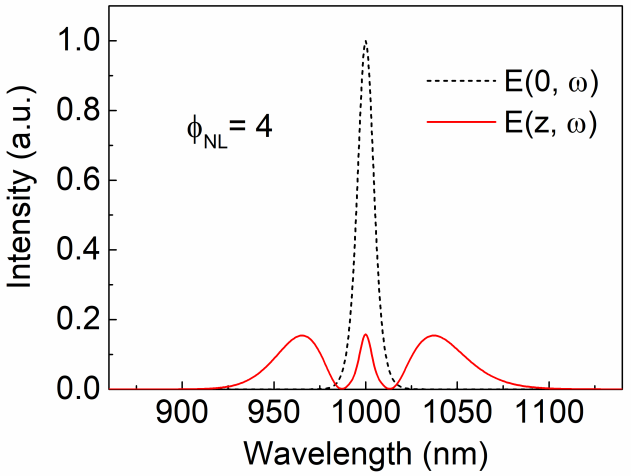

Figure 3.2: Initially transform-limited $sech^2$ pulse undergoing SPM with a nonlinear phase shift of $\phi_{NL} = 4$.

$$\frac{\partial A_1}{\partial z} + \frac{1}{v_{g1}}\frac{\partial A_1}{\partial t} - \frac{i}{2}\frac{\partial^2 k_1}{\partial \omega^2}\frac{\partial^2 A_1}{\partial t^2} + \frac{1}{2}\varepsilon_0 \omega_1 n_2 n \left|A_1\right|^2 A_1 = \frac{i d_{eff}\omega_1^2}{k_1 c^2} A_2 A_3 e^{i\Delta k z} \tag{3.12}$$

and similar for A_2 and A_3. The first term corresponds to GVM, the second GVD, and the third SPM. Analytical treatment of these equations is exceptionally difficult, and numerical approximations are computationally taxing [63]. Furthermore, the validity of the slowly varying envelope approximation used in the derivation of equation (3.12) is questionable when dealing with broadband pulses. An alternative approach is to consider all interacting waves as part of a common electric field envelope, which can be described by a single differential equation. Conforti *et al* derived the following expression to model broadband pulse evolution in $\chi^{(2)}$ media [64]

$$\frac{\partial A}{\partial z} + i\frac{\beta_2}{2}\frac{\partial^2 A}{\partial T^2} = -i\frac{d_{eff}\omega_0^2}{2kc^2}\left(1 - \frac{i}{\omega_0}\frac{\partial}{\partial T}\right)\left[A^2 e^{i\omega_0 T - i(k-\beta_1\omega_0)z} + 2\left|A\right|^2 e^{-i\omega_0 T + i(k-\beta_1\omega_0)z}\right] \quad (3.13)$$

which is referred to as the nonlinear envelope equation (NEE). Here, the time coordinate has been transformed using $T = t - \beta_1 z$ to a comoving frame at the group velocity, $b_1 = 1/v_g$, corresponding to the reference frequency, w_0. The NEE has been applied to femtosecond OPOs to yield highly accurate reproductions of experimentally observed pulse spectra [65].

3.3.6 Dispersion control

Cavity dispersion is contributed by all intracavity elements, including the nonlinear crystal and mirror reflections. In accordance with equation (3.8), as dispersion tends to zero, the sensitivity of cavity length fluctuations to wavelength changes increases. While the dispersion contribution of the crystal is usually well known from the material Sellmeier equations, contributions from the cavity mirrors are often completely unknown, leading to a complex net dispersion profile. This results in unpredictable cavity length tuning, and output pulses which are highly variable in both their duration and spectral shape, all of which are detrimental effects for practical applications.

Despite strong interplay between dispersion and nonlinearity, transform-limited output pulses can be generated from an OPO if the dispersion is suitably managed. Like in a mode-locked laser, if the net cavity GVD is negative, a steady state solitonic pulse can form with the electric field envelope given by $E = E_0 sech\left(\frac{t}{t_0}\right)$ where the pulse FWHM is $\Delta t = 1.763\tau_0$ [66]. Since the sign of GVD is usually positive for signal-resonant OPOs in the near-IR, additional intracavity elements are required to provide negative GVD. A common scheme is to insert a pair of equilateral prisms into one arm of the cavity, which exploits angular dispersion to reverse the

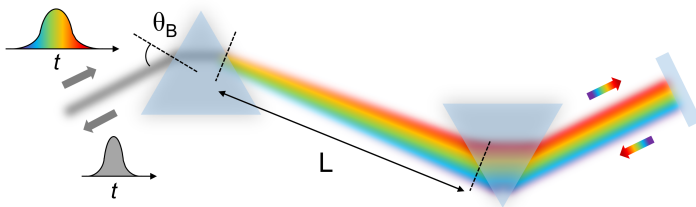

Figure 3.3: Dispersion compensation using an equilateral prism pair.

chirp accumulated in other elements [67]. Figure 3.3 illustrates how each wavelength experiences a different path length, enabling the pulse to be compressed to the transform limit.

The total GVD introduced by a prism pair is given by [67]

$$\beta_2^{PP} = \frac{\lambda^3}{2\pi c^2}\left(l\frac{d^2n}{d\lambda^2} - 4L\left(\frac{dn}{d\lambda}\right)^2\right) \tag{3.14}$$

where n is the refractive index of the prism material, l is the mean path length through the prism material, and L is the prism separation. A prism pair is an attractive choice for two reasons: the ability to finely tune dispersion without affecting beam pointing by translating a prism in a direction perpendicular to its base (to increase/decrease path length in the glass), and low insertion loss by using incidence at Brewster's angle. The prisms dominate the total cavity dispersion, leading to smooth and continuous cavity length tuning.

3.4 Resonator design

Femtosecond OPOs are generally pumped by a mode-locked laser, delivering pulse trains at a repetition rate of $\sim$ 100 MHz, corresponding to pulse-to-pulse separations of $\sim$ 10 ns. Due to the low single-pass parametric gain, it is essential that the OPO cavity length is precisely matched to this round-trip time in order for oscillation to be achieved. Furthermore, the resonator is designed such that the nonlinear crystal is placed at a focus

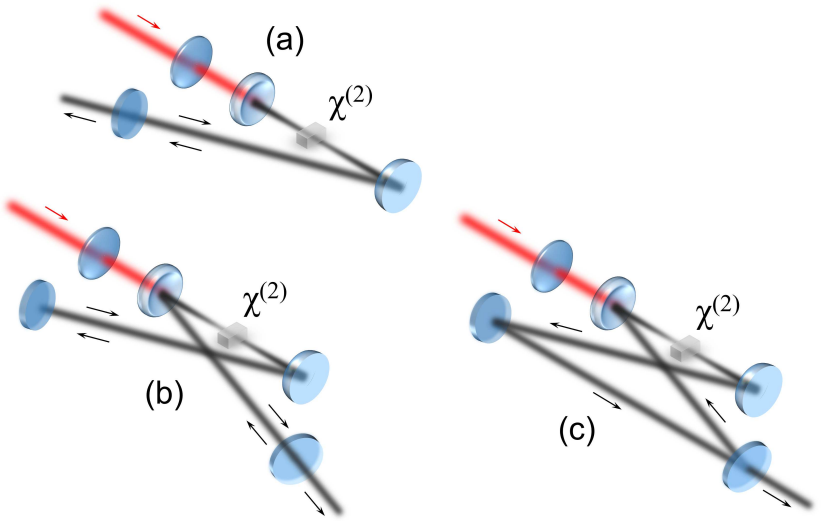

Figure 3.4: Different resonator configurations used for synchronously pumped OPOs. (a) z-cavity, (b) x-cavity, (c) Ring cavity

formed by two concave mirrors or lenses, in order to maximise gain. Some common resonator designs are shown in Figure 3.4, and a photograph of a practical setup is shown in Figure 3.5.

Figure 3.4(a) and (b) show two examples of standing wave cavities, which are often the first choice design due to their simple alignment, and because they enable two passes through a dispersion controlling element such as a prism pair. The ring cavity is advantageous in that light only propagates in one direction, removing any possible back-reflections to the pump laser, which can affect mode-locking stability. Furthermore the oscillation threshold is reduced compared to the standing wave cavity, as there is only one crystal pass per round trip. It is essential that the focusing elements of the cavity are separated by a distance which ensures a stable Gaussian mode solution, i.e. the resonating beam does not change size from one round trip to the next. Cavity stability is calculated using the well-known Gaussian beam transformation matrices, which allow each

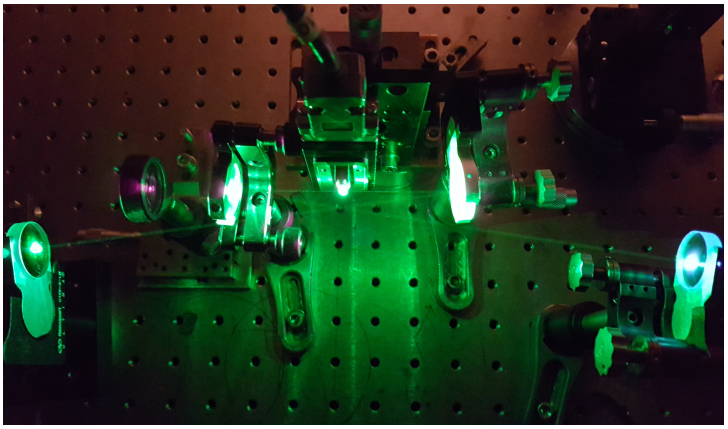

Figure 3.5: Femtosecond synchronously-pumped OPO operating in an x-cavity configuration.

optical element to be represented by a 2×2 matrix of the form $\begin{pmatrix} A & B \\ C & D \end{pmatrix}$ which act upon a Gaussian beam described by its complex q parameter, defined as

$$\frac{1}{q} = \frac{1}{R(z)} - \frac{i\lambda}{\pi n w^2(z)} \tag{3.15}$$

where $R(z)$ is the radius of curvature of the beam wavefront at position z, λ is the wavelength, n is the refractive index, and $w(z)$ is the beam radius at position z. A list of ABCD matrices for common optical elements can be found in [68].

After propagating through an optical element, the q parameter is modified according to

$$q_2 = \frac{Aq_1 + B}{Cq_1 + D} \tag{3.16}$$

Then, using equations (3.15) and (3.16), the beam radius can be calculated at an arbitrary position in a composite optical system with the formula

$$w(z) = \sqrt{\frac{\lambda}{n\pi}\left(\frac{A^2 z_0^2 + B^2}{z_0 (AD - BC)}\right)} \tag{3.17}$$

where A, B, C, and D are the cumulative matrix elements evaluated at position z, n is the refractive index, and $z_0 = \frac{\pi n w_0^2}{\lambda}$ is the Rayleigh range. In a resonator, the beam radius of the stable cavity mode can be calculated by setting the condition that the q parameter is exactly reproduced after one round trip, and solving for w [69]

$$w^2 = \frac{|B|\,\lambda}{n\pi}\sqrt{\frac{1}{1 - \left(\frac{A+D}{2}\right)^2}} \tag{3.18}$$

It can be seen from equation (3.18), that in order for w to be real, the condition $|A + D| < 2$ must be satisfied, which is often referred to as the resonator stability condition. Therefore, the focal lengths and physical separation of the cavity mirrors are carefully chosen to ensure the total ABCD matrix for the resonator corresponds to a stable cavity. In order to optimise parametric gain, it is desirable that the beam focus inside the nonlinear crystal is as close as possible to the optimum Boyd-Kleinmann focusing parameter, which has been determined for a crystal of length L to be [54]

$$\xi = \frac{L}{b} = 2.84 \tag{3.19}$$

where $b = 2z_0$ is the confocal parameter. Equation 3.19 dictates which focusing optics are likely to yield the highest conversion efficiencies. The pump focusing optics are then chosen to match the pump beam to the signal cavity mode, such the focusing parameters are approximately equal ($\xi_p = \xi_s$). These calculations are more important for longer nonlinear crystals (~ 50 mm), due to the small variation in beam size over the length of a short crystal.

3.5 Numerical simulation

Some OPO designs, particularly those producing ultra-broadband spectra, or those containing additional intracavity elements such as optical fibre (fibre-feedback OPOs), require simulations to be performed in order to better understand their pulse dynamics. The simulation may take the form of an iterative procedure, where input field is propagated around the cavity for one round trip using some form of equation (3.12) or (3.13) and then added to the next pump pulse, with the process repeated until steady-state convergence is achieved. The most convenient numerical approach used to tackle the relevant differential equations is the split-step Fourier method [61]. Here, the propagation equation is divided into its linear and nonlinear components, which are approximated to act independently over a small distance step, h. The propagation equation for a pulse in the presence of dispersion and $\chi^{(3)}$ nonlinearity is

$$\frac{\partial A}{\partial z} = \sum_{n=2}^{\infty} \frac{i^{n+1}}{n!} \beta_n \frac{\partial^n A}{\partial T^n} + i\gamma \left|A\right|^2 A = 0 \tag{3.20}$$

where $\gamma = \frac{n_2 \omega}{c A_{eff}}$, and A_{eff} is the effective beam area ($1/e^2$ intensity) in the medium. Equation (3.20) can be rewritten in terms of dispersive and nonlinear operators

$$\frac{\partial A}{\partial z} = \left(\hat{D} + \hat{N}\right) A \tag{3.21}$$

where $\hat{D} = \sum_{n=2}^{\infty} \frac{i^{n+1}}{n!} \beta_n \frac{\partial^n}{\partial T^n}$ and $\hat{N} = -i\gamma \left|A\right|^2$.

The propagation from $z = 0$ to $z = h$ is carried out in two stages; the first stage considers the effect of nonlinearity alone, and the second dispersion alone. Mathematically, the approximate solution is given by

$$A\left(z = h, T\right) \approx exp\left(h\hat{D}\right) exp\left(h\hat{N}\right) A\left(0, T\right) \tag{3.22}$$

where the dispersive exponential is evaluated in the spectral domain using equation (3.6), and the nonlinear exponential reduces to (3.11). Figure 3.6 shows a 100 fs pulse propagating through 10 cm of MgO:PPLN at at

central wavelength of $\lambda = 1.2$ μm, based on a numerical solution of equation (3.20), considering second- and third-order dispersion (β_2 and β_3), and $\gamma = 0.005$ $W^{-1}m^{-1}$. The peak power and beam radius were taken to be 15 kW and 100 μm^2, respectively. A similar method can be applied to equations (3.12) and (3.13) where simplifications cannot be made, albeit a 4th-order Runge-Kutta algorithm is necessary to integrate the nonlinear step.

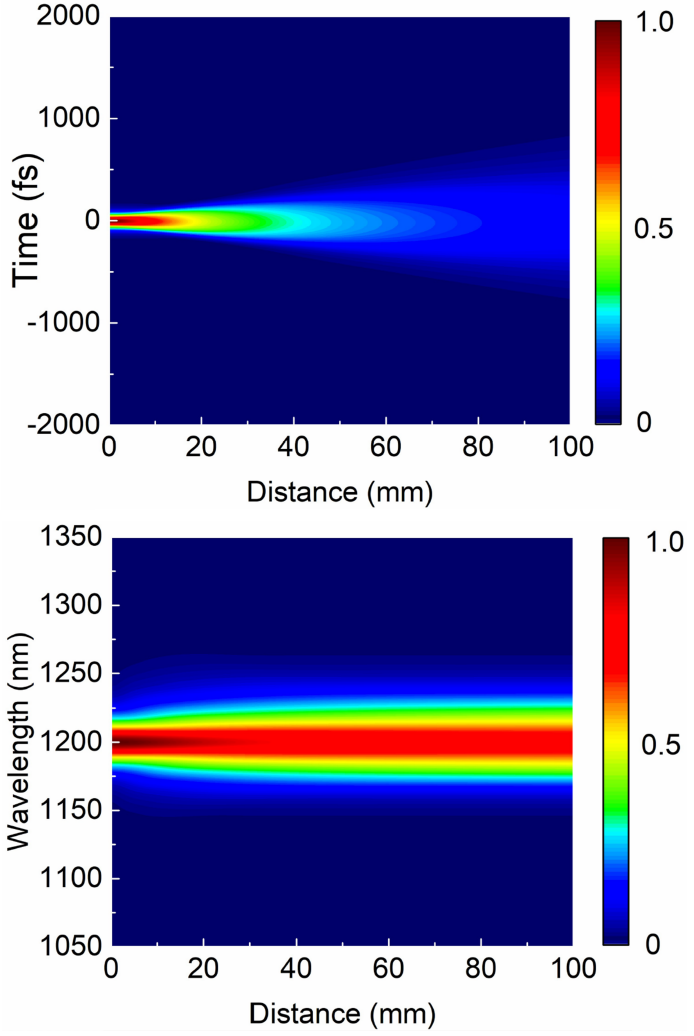

Figure 3.6: Temporal and spectral evolution of a 100 fs pulse propagating through 10 cm of MgO:PPLN.

4 Soliton fibre-feedback femtosecond optical parametric oscillator

This chapter constitutes the following publication:

1. *Generation of widely-tunable, ultra-stable, sub-100 fs solitons and dispersive pulses in a fibre-feedback optical parametric oscillator*
C. F. O'Donnell, S. Chaitanya Kumar, T. Paoletta, and M. Ebrahim-Zadeh
(To be submitted).

4.1 Background and motivation

Optical frequency conversion techniques based on $\chi^{(2)}$ nonlinear processes are heavily exploited throughout industry and academic research to generate coherent light in regions of the electromagnetic spectrum inaccessible to conventional lasers. Synchronously-pumped optical parametric oscillators (OPOs), are firmly established as the gold-standard light sources for applications requiring broadly tunable ultrafast pulses at high repetition-rates [33, 70], including molecular fingerprint spectroscopy, coherent anti-Stokes Raman scattering (CARS), stimulated Raman scattering (SRS), and high-resolution multiphoton microscopy [28, 71–73]. OPOs based on nonlinear crystals such as MgO-doped periodically poled $LiNbO_3$ (MgO:PPLN), BiB_3O_6 (BIBO), together with a new generation of non-oxide materials, have enabled complete wavelength coverage from the UV to ~12 μm in the deep-infrared, producing quasi-CW pulse trains with multi-kilowatt level peak power [26, 28, 74, 75]. Furthermore, the intrinsic phase-locked nature of degenerate synchronously-pumped OPOs has enabled them to be a driving force behind development of mid-IR frequency combs and the dawn of dual-comb spectroscopy [76–78].

From a quantum standpoint, OPOs play host to a rich variety of nonlinear effects, which have been applied to build coherent networks capable of advanced computation [31, 79]. Pulse dynamics in such devices is a com-

plex interplay of $\chi^{(2)}$ nonlinearity, dispersion, and Kerr nonlinearity, and remains an intensely studied field of research [64, 80, 81]. Despite possessing outstanding physical attributes, ensuring long-term high-quality performance of femtosecond OPOs requires careful control of intracavity dispersion and cavity length, in the form of piezoelectric actuators and feedback electronics, resulting in an expensive and unwieldly system. With understandable reluctance to invest in such a scheme, supercontinuum generation has been explored as a cheaper alternative for the near- to mid-infrared [82, 83]. However, such sources offer much lower spectral brightness and suffer from intrinsically higher background noise [84]. Another strategy is the generation of frequency-shifted solitons in a single pass through a highly nonlinear fibre. However, since the available tunability is dependent on the input peak power, powerful pump sources at >1.5 μm are required to match the tuning range of an OPO [85, 86]. In many cases, particularly at high repetition rates, the only source able to satisfy this condition is an OPO itself [87].

Since OPOs achieved technological maturity in the late 1990s, efforts to reduce their cost and complexity have been hampered by fundamental limitations imposed by long free-space cavities and synchronisation tolerances of ~100 μm. One promising template for synchronously-pumped OPOs is a fibre-feedback resonator, which has a dramatically reduced footprint, as most of the cavity length is confined inside a passive optical fibre [88]. Moreover, compared to a free-space resonator, increased intracavity group velocity dispersion (GVD) leads to remarkable insensitivity of the output power and wavelength to cavity length fluctuations, negating the requirement for active stabilisation. This cavity configuration is especially effective when using the combination of a powerful pump laser and a relatively long nonlinear crystal, yielding a large parametric gain, and requiring only a small feedback signal to sustain oscillation [89–91]. As pump pulse durations decrease towards ~100 fs, the use of long nonlinear crystals is precluded by enhanced temporal walk-off, and nonlinear as well as dispersive effects become more pronounced, leading to spectral and temporal broadening. Subsequently, the fibre-feedback concept

has not been demonstrated at such a short timescale in a tunable device, with sub-100 fs pulses, only achieved by precise dispersion engineering in a 1.03 μm pumped doubly resonant oscillator at degeneracy [92].

On the other hand, self-similar pulse evolution, in the form of solitons, dissipative solitons and similaritons, is a well-established method of ultrashort pulse generation in mode-locked lasers. Early fibre lasers, operating near ~1.5 μm, exploited the anomalous dispersion of standard silica fibres at this wavelength to generate solitons as short as ~200 fs, although maximum pulse energies were limited to $\sim$ 100 pJ as a direct result of the soliton area theorem [93, 94]. In addition, when solitonic pulses encounter periodic perturbations from gain and output coupling elements, energy is shed in the form of dispersive waves, which co-propagate in the cavity with a different group velocity and lead to the drain of power into Kelly sidebands at phase-matched wavelengths [95, 96]. Contemporary devices circumvent these issues by generating linearly chirped pulses in the normal dispersion fibres, with a grating compressor used to restore transform-limit pulses outside the cavity [97]. Conversely, bulk lasers and synchronously pumped OPOs often deploy intracavity elements, such as prism pairs, to dechirp the pulse on each round trip. Soliton formation has been observed in such OPOs near the zero dispersion wavelength, but competition between synchronisation of the dispersive and solitonic spectral components resulted in significant instability [98]. Due to the wavelength dependence of crystal dispersion, the prism pair needs to be continually translated as the wavelength is tuned, in order to maintain chirp-free pulses.

Here, we report a synchronously-pumped fibre-feedback OPO generating widely tunable <100 fs pulses at 80 MHz repetition rate in the near-infrared. Pumping with a Ti:sapphire laser at 803 nm, up to 110 mW of output power is generated with a total tuning range of 1051–1700 nm, which can be rapidly covered by a combination of cavity length variation and changing the crystal quasi-phased-matched (QPM) grating period. In the anomalous dispersion regime (λ > 1310 nm), we observe transform-limited pulses, power scaling, and hysteresis associated with

soliton formation, whereas in the presence of normal dispersion ($\lambda < 1310$ nm) chirped pulses of 80–100 fs are accompanied by Kelly sideband-like spectral features. A theoretical model based on the nonlinear Schrödinger equation is used to simulate the pulse dynamics, and provides excellent agreement with experimental results. To the best of our knowledge, this represents the first report of soliton formation in a fibre-feedback OPO, and the first observation of sideband formation in a synchronously pumped OPO. Compared to traditional femtosecond OPOs, this device offers improvements in stability, footprint, and cost, making it an attractive source for coherent spectroscopy and microscopy. The combination of high parametric gain with a passive waveguide element also offers a unique platform to study soliton behaviour, in presence of both $\chi^{(2)}$ and $\chi^{(3)}$ nonlinear processes, paving the way for future advances in tunable ultrafast sources.

4.2 Experiment

The setup for the soliton fibre-feedback OPO is shown in Figure 4.1. A KLM Ti:sapphire oscillator (Spectra Physics, *Mai Tai HP*) was used as the pump source, providing ~100 fs pulses at 803 nm at a repetition rate of 80 MHz. To minimise the risk of crystal damage, the maximum average pump power in front of M_1 was limited to ~1.3 W by a variable attenuator consisting of a half-wave plate followed by a polarising beamsplitter. After passing a second half-wave plate, the extraordinarily polarised beam was focused by lens, L_1 ($f = 75$ mm), to a waist radius of $w_0 \sim 16$ μm at the centre of a 1-mm-long MgO:PPLN crystal, for type-0 ($e \rightarrow ee$) non-critical phase-matching. The crystal contains QPM grating periods continuously varying over $\Lambda = 16$–23 μm, in a fan-out structure across the 3.4-mm-wide aperture, and both faces are anti-reflection-coated for the signal and pump wavelengths. The crystal is mounted on a temperature-stabilised oven and maintained at 50°C for the duration of the experiment. The resonator is configured as an x-cavity, enabling one mirror to be coated directly onto the end facet of the single-mode fibre (R > 97% across 1260–1625 nm). Two concave spherical mirrors, $M_{1\text{–}2}$ ($r = 100$ mm) form the

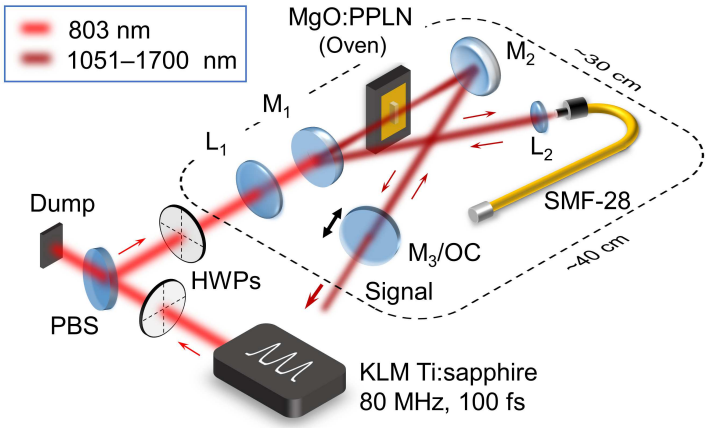

Figure 4.1: Schematic of the experimental setup for the Ti:sapphire pumped soliton fibre-feedback OPO. HWPs, half-wave plates; PBS, polarising beamsplitter; L, lenses; M, mirrors; OC, output coupler; SMF-28, single-mode fibre retroreflector.

intracavity focus, and a plane output coupler M_3/OC completes the cavity. Mirrors, $M_{1–2}$, are of fused silica substrate coated for high reflection ($R > 99.8\%$) across 980–1600 nm and high transmission ($T > 90\%$) for the pump at 803 nm. Approximately 62% of the cavity is confined within the 86-cm-long single mode fibre (SMF-28 Ultra, mode field diameter 9.2 μm at $\lambda = 1210$ nm). An adjustable focus aspheric lens, L_2 ($f = 11$ mm), with a broadband anti-reflection coating ($R < 1\%$ across 1100–1600 nm), is used to couple light into the fibre. For signal extraction, we alternate between two output couplers with $T = 5\%$ and 30%, mounted on a precision translation stage for fine control of cavity synchronisation. A photo of the laboratory experimental setup is displayed in Figure 4.2.

Figure 4.2: Photo of the soliton fibre-feedback OPO.

4.3 Experimental results

4.3.1 Wavelength tuning

Optimisation of the fibre retroreflector coupling efficiency was performed using an input beam from an external near-IR OPO, and measuring the power reflected from a pellicle beamsplitter. It was found that ~96% of the reflected beam remained horizontally polarised, implying that use of polarisation maintaining fibre would not substantially improve device efficiency. The maximum aggregate in/out coupling efficiency from the retroreflector was measured to be ~70%. Wavelength tuning of the OPO was accomplished by variation of the QPM grating period, and adjusting the cavity length. Optical spectra were recorded using a spectrum analyser with resolution ~0.7 nm, with the data shown in Figures 4.3 and 4.4. For each spectrum, the central signal wavelength was extracted using a centre-of-mass averaging algorithm. White data points in Figure 4.3 represent the signal wavelengths generated at selected QPM grating periods, superimposed on the parametric gain bandwidth for a 1-mm-long MgO:PPLN crystal, calculated using the Sellmeier equations in [99]. For each grating period, the broad signal gain bandwidth enables ~100 nm of additional tuning by changing the cavity length.

In Figure 4.4, the data points for all grating periods are plotted against the relative change in cavity length. Here, it becomes evident that dispersion shifts from the normal to anomalous regime (positive to negative)

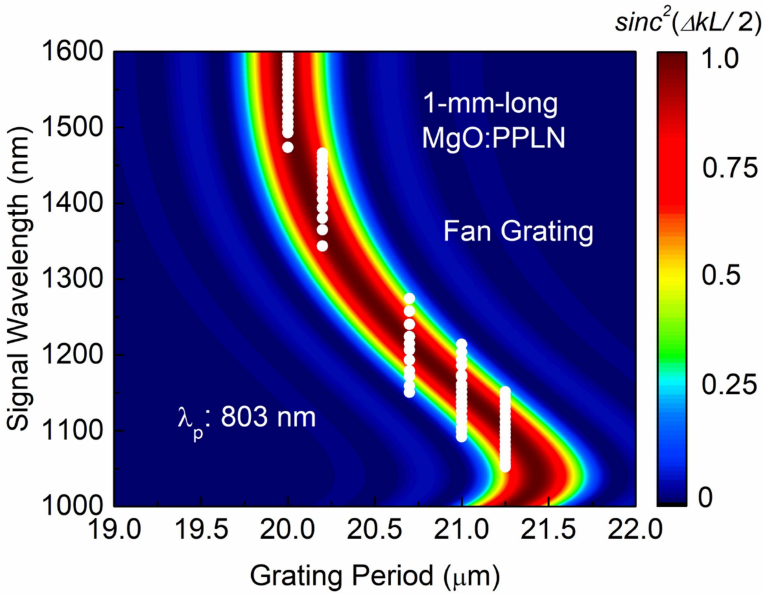

Figure 4.3: Measured signal data points (white), superimposed on the parametric gain bandwidth for 1-mm-long MgO:PPLN crystal with QPM grating periods varying from $\Lambda = 19.0$–22 μm, calculated using the sellmeier equations in [99].

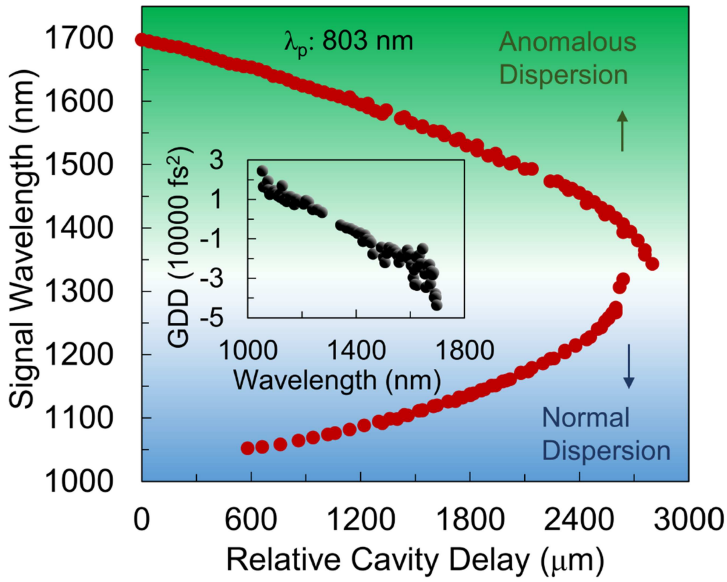

Figure 4.4: Cavity delay tuning of the OPO, with measured signal data points plotted against relative change in cavity length, normalised to the shortest possible cavity for operation; inset: calculated net cavity GDD across the tuning range.

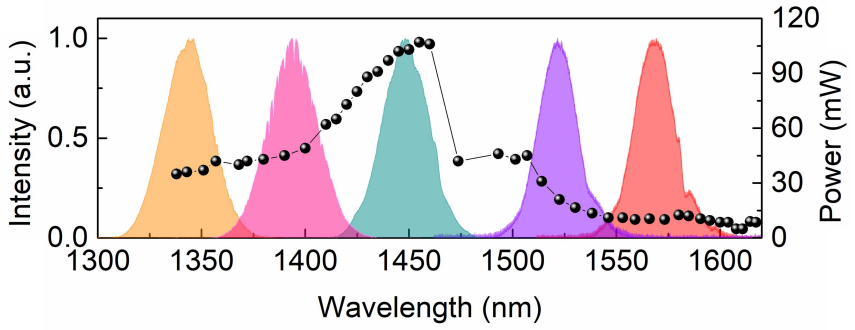

Figure 4.5: Measured signal spectra and output average power across the anomalous dispersion regime.

at a wavelength of $\lambda_s \sim 1310$ nm, consistent with the expected zero dispersion wavelength (ZDW) of single-mode silica fibres. Choice of shorter or longer grating periods determines operation in the normal and anomalous dispersion regimes, respectively. Close to the ZDW, the signal spectra are instantaneously broad and unstable, characteristic of synchronously-pumped OPOs with negligible GVD [100]. The total tuning range was recorded to be 1051–1700 nm, which included a transition through degeneracy at $\lambda_s \sim 1606$ nm ($\lambda_p = 803$ nm), and the group delay dispersion (GDD) was calculated to vary from 3.46×10^4 fs^2 at 1051 nm, to -6.69×10^4 fs^2 at 1700 nm, using the measured rate of cavity length tuning, $d\lambda_s/dL$, and the expression

$$GDD\,(\lambda) = \frac{\lambda_s^2}{2\pi c^2}\left(\frac{d\lambda_s}{dL}\right)^{-1} \tag{4.1}$$

where the tuning rate was approximated using $d\lambda_s/dL \approx \Delta\lambda_s/\Delta L$ for small intervals of 80 μm. The behaviour and output characteristics in each dispersion regime are discussed separately in the following sections.

4.3.2 Anomalous dispersion characteristics

The anomalous dispersion regime refers to all wavelengths longer than $\lambda_s \sim 1310$ nm, and wavelength tuning in this regime is achieved using grating periods of $\Lambda < 20.3$ μm. Here, the net negative GVD acts to oppose nonlinear effects, primarily self-phase modulation (SPM), which are associated with ultrashort pulse propagation in optical fibres. Figure 4.5 shows that across this region spectra exhibit a symmetric shape. With the 30% output coupler in place and the grating period set to $\Lambda = 20.2$ μm, output power steadily increases with cavity delay from 40 mW to reach a maximum of 110 mW at 1460 nm. Beyond this wavelength, oscillation abruptly ceases, and can only be achieved at $\lambda_s > 1460$ nm if the output coupling is reduced, and the grating period is decreased to $\Lambda = 20.0$ μm. Interestingly, once the OPO switches off, it is observed that to recover the maximum power at 1460 nm, the cavity length must first be positively detuned to the mirror position equivalent to $\lambda_s \sim 1350$ nm to restart oscillation, and then negatively detuned to its original position, i.e. the cavity length tuning displays hysteresis. It is also found that while the oscillation threshold at 1350 nm is ~700 mW, at 1460 nm it is ~900 mW. Using a 5% output coupler, the device could be freely tuned between 1470–1700 nm using the $\Lambda = 20.0$ μm grating period with output powers between 10–40 mW. At 1606 nm, corresponding to degeneracy, the spectrum and power were observed to rapidly fluctuate, as the OPO alternated between singly- and doubly-resonant operation. Beyond degeneracy, singly-resonant operation is resumed, albeit with the signal now at a longer wavelength than the idler. Due to the limited range of the spectrum analyser, no signal spectra could be recorded beyond 1650 nm, however the idler at $\lambda_i < 1606$ nm could be viewed.

Signal pulse durations were recorded using interferometric autocorrelation, with a typical measurement of ~106 fs (assuming a $sech^2$ shape), and its corresponding spectrum, as shown in Figure 4.6. The spectral FWHM of $\Delta\lambda_s \sim 21$ nm yields a time-bandwidth product of $\Delta\nu\Delta\tau \sim 0.316$, very close to the transform limit. Across the range 1330–1460 nm,

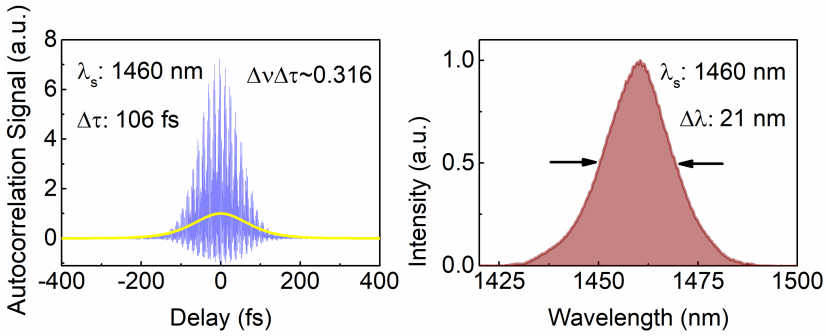

Figure 4.6: Typical interferometric autocorrelation at 1460 nm, and simultaneous signal spectrum.

repeated measurements confirm 95–110 fs pulses with pedestal-free autocorrelation traces, indicating minimal chirp. Figure 4.7 and its inset show the excellent passive power and wavelength stability, recorded over periods of 30 minutes and 20 minutes, respectively. During this time, rms power fluctuations were measured to be 0.26%, and central wavelength fluctuations to be 0.016%, in strong agreement with previous reports [88, 91]. For clarity, the central wavelength and FWHM bandwidth stability are also plotted separately in Figure 4.8.

4.3.3 Normal dispersion characteristics

When operating in the normal dispersion regime ($\Delta\lambda_s < 1310$ nm), interaction between positive GVD and nonlinear effects, primarily self-phase modulation (SPM), act to enhance the spectral and temporal broadening effects experienced by the intracavity pulses. A measure of the relative importance of dispersion and nonlinearity across the operating bandwidth is given by the quantity N, defined as

$$N^2 = \frac{L_d}{L_n} = \frac{\gamma(\omega) P_0 T_0^2}{|\beta_2(\omega)|} \tag{4.2}$$

where L_d and L_n are the characteristic dispersive and nonlinear lengths,

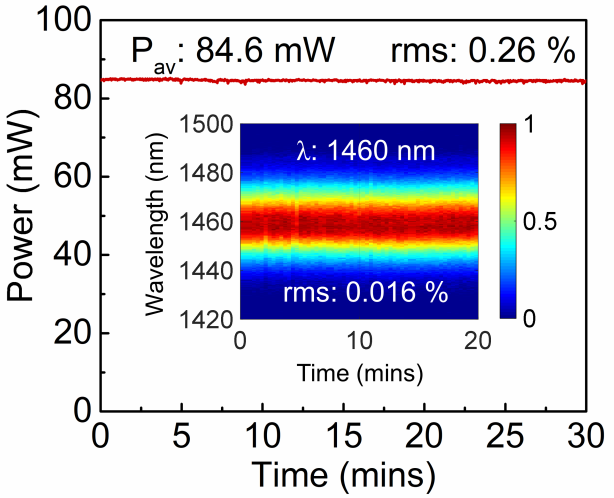

Figure 4.7: Power stability measurement at $\lambda_s \sim 1455$ nm over a period of 30 minutes, inset: spectral stability measurement over a period of 30 minutes.

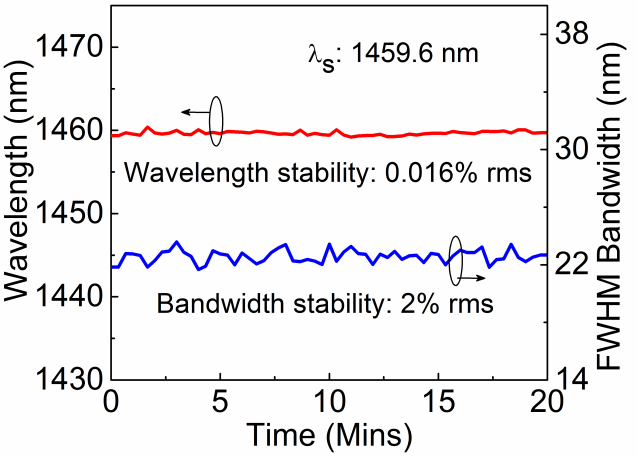

Figure 4.8: Rms fluctuations in central wavelength and FWHM bandwidth over 20 minutes.

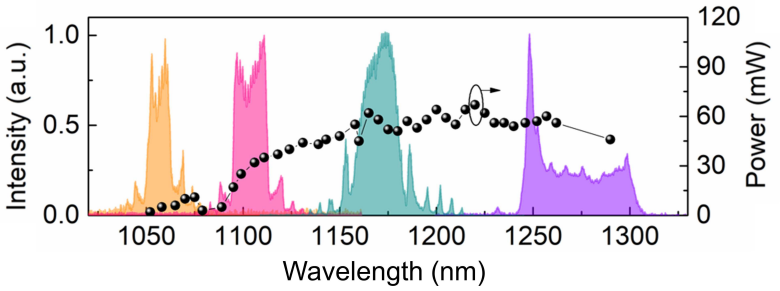

Figure 4.9: Measured signal spectra and output average power across the normal dispersion regime.

$\gamma(w) = \omega_0 n_2 / c A_{eff}$ is the nonlinear coefficient, $n_2 = 2.6 \times 10^{-20}$ m^2/W is the nonlinear refractive index of single-mode fibre, $A_{eff} = 75$ μm^2 is the effective mode area, P_0 is the peak power, and T_0 is related to the pulse FWHM by $\Delta\tau_{FWHM} = 1.763 T_0$. Using these values, along with an average power in the fibre of 100 mW, $\Delta\tau_{FWHM} = 100$ fs, and $\beta_2(\omega)$ determined from Figure 4.4, yields a value of N_2 varying from ~8 at 1050 nm to ~40 at 1270 nm. This suggests that the cavity is heavily dominated by SPM, in particular when operating close to the ZDW, where spectral bandwidths of up to 60 nm FWHM are measured.

By tuning to shorter wavelengths, corresponding to increasing β_2, we observe the spectrum evolving through distinct phases, shown in Figure 4.9. Also plotted is the extracted power across the tuning range, which remains in the range 60–70 mW over 1150–1300 nm, before trailing off with increasing dispersion. Beginning at $\lambda_s \sim 1230$ nm, well-defined spectral sidebands emerge in the wings of the pulse. These resemble Kelly sidebands often produced in mode-locked lasers operating in the anomalous dispersion regime, in that their wavelength offset is proportional to $m^{0.5}$, where m is the order of the sideband. Finally, at the shortest wavelengths, the main spectral lobe acquires steep square sides and deep modulations across the central part. This is consistent with the phenomenon of optical wave breaking, where normal dispersion causes the red-shifted spectral components of a chirped pulse to overtake the slower travelling blue-

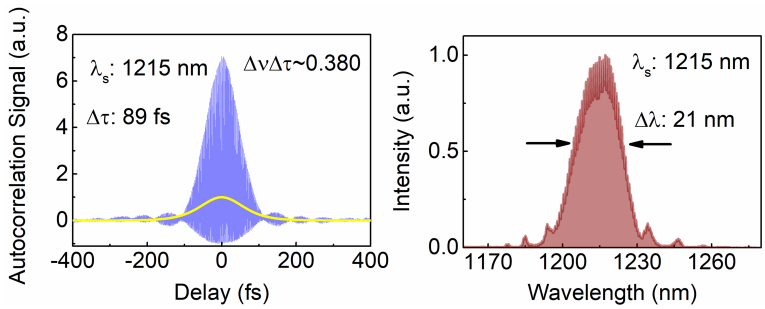

Figure 4.10: Typical interferometric autocorrelation at 1215 nm and simultaneous signal spectrum.

shifted components, leading to the formation of an oscillatory interference structure [101].

A typical interferometric autocorrelation at $\lambda_s \sim 1215$ nm and its corresponding spectrum are shown in Figure 4.10, revealing a pulse duration of 89 fs, shorter than that of the pump. However, the time-bandwidth product of $\Delta\nu\Delta\tau \sim 0.380$ is 1.2 times over the $sech^2$ transform limit, confirming the chirped nature of the pulses. A typical power scaling measurement, plotted in Figure 4.11, shows an oscillation threshold of ~800 mW and a slope efficiency of $\eta \sim 13$ %, with no evidence of saturation, indicating that use of stronger output coupling could further increase output power. This threshold is slightly higher than that measured in the anomalous dispersion regime.

The excellent spatial TEM_{00} beam quality exhibited by resonating signal, recorded using a pyroelectric camera, is displayed in the inset to Figure 4.11. Finally, the spectral stability measurement in Figure 4.12 at 1171 nm reveals similarly low fluctuations of the central wavelength to the anomalous dispersion region, and indicates that the sidebands remain invariant in position over time.

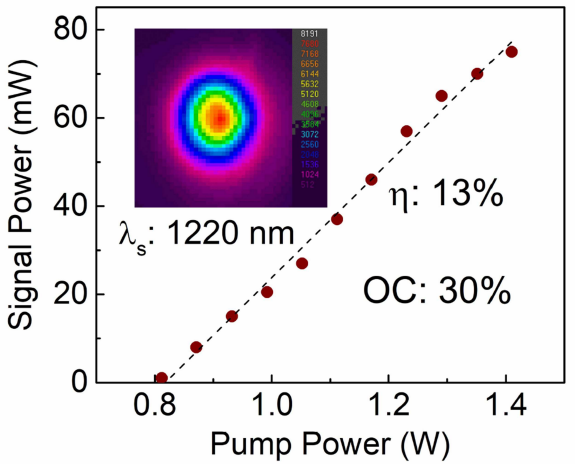

Figure 4.11: Power scaling measurement at 1220 nm, inset: signal beam profile.

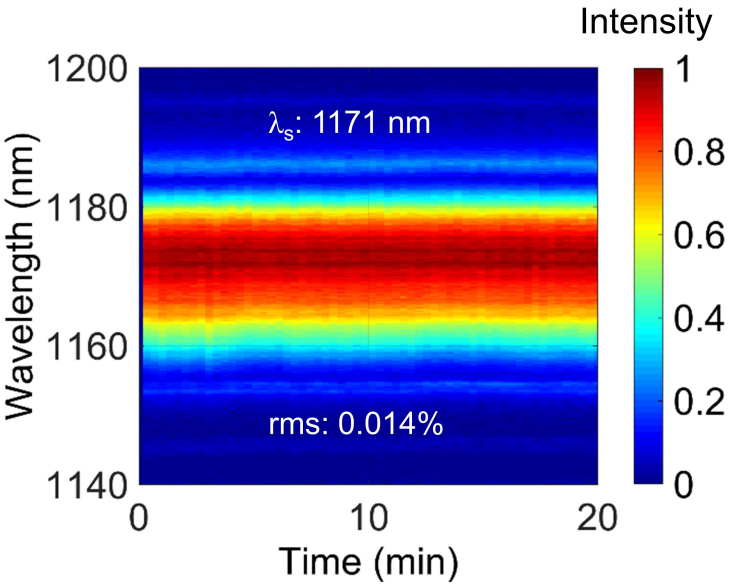

Figure 4.12: Spectral stability measurement at 1171 nm over a period of 20 minutes.

4.4 Pulse dynamics

4.4.1 Numerical model

Certain behaviour, including spectral sidebands in the presence of normal dispersion, and cavity delay hysteresis in the anomalous dispersion regime, are not characteristic of standard femtosecond OPOs and hint at alternative pulse dynamics. Since intracavity powers are many times higher than the soliton energy, it is expected that soliton effects are heavily influential. In order to study pulse evolution inside the OPO, we performed numerical simulations considering the interplay between dispersion, nonlinearity, and parametric gain. The evolution of a resonating signal pulse inside the cavity can be described by the 1D generalised nonlinear Schrödinger equation (GNLSE) for the signal field, E_s:

$$i\frac{\partial E_s}{\partial z} - \sum_{n=2}^{\infty} \frac{i^{n+1}}{n!}\beta_n \frac{\partial^n E_s}{\partial T^n} + \gamma(\omega)\left(1 + \frac{i}{\omega_0}\frac{\partial}{\partial T}\right)\left(E_s(z,T)\int_0^{\infty} R(T')\left|E_s(T-T')\right|^2 dT'\right) = i\frac{g(T)}{2}E_s \tag{4.3}$$

which has been normalised such that $P_0 = |Es|^2$ is the peak power, $T = t - z/v_g(\omega_0)$ is the retarded time, $R(T')$ is the Raman response function, and $g(T)$ is a time-dependent parametric gain function. Dispersion parameters from 2^{nd} to 4^{th} order were calculated using a fit to the data in Figure 4.4. An approximation for $g(T)$ is given by the single-pass parametric gain in the low-gain regime, assuming no pump depletion and a $sech^2$ pump pulse shape:

$$g(T) = \sqrt{\frac{8\pi d_{eff}^2 P_p^{av} g_s g_\tau sech^2\left((T + \Delta T_s)/T_p\right)}{1.763\lambda_s\lambda_i n_p n_s n_i c\varepsilon_0 w_p^2 f_{rep} T_p}} \tag{4.4}$$

where d_{eff} is the effective nonlinearity of MgO:PPLN, P_p^{av} is the average pump power, g_s and g_t are the spatial and temporal coupling coefficients,

Quantity	d_{eff}	P_p^{av}	g_s	g_τ	T_p	$n_{p,s,i}$	w_p	f_{rep}
Value	16	1.3	~0.5	~0.7	~57	~2.1	16	80
Unit	pm/V	W	-	-	fs	-	μm	MHz

Table 4.1: Quantities contributing to parametric gain. Refractive indices are calculated from [35].

$1.763T_p$ is the pump pulse duration, ΔT_s is the temporal offset from perfect synchronisation, $\lambda_{s,i}$ are the signal and idler wavelengths, $n_{p,s,i}$ are the refractive indices experienced by pump, signal and idler, w_p is the pump beam radius at the focus, and f_{rep} is the repetition rate. The frequency-dependent nonlinear coefficient is given by

$$\gamma(\omega) = \frac{\omega n_2}{c A_{eff}} \tag{4.5}$$

where the effective mode area is $A_{eff} = 75\ \mu\text{m}^2$, and the nonlinear refractive index is $n_2 = 2.6 \times 10^{-20}\ \text{m}^2/\text{W}$.

The Raman response function has the form

$$R(T) = (1 - f_R)\,\delta(T) + f_R h_R(T) \tag{4.6}$$

where $\delta(T)$ is a Dirac delta function, and

$$h_R = \left(\tau_1^{-2} + \tau_2^{-2}\right) \tau_1 e^{-T/\tau_2} sin\left(T/\tau_1\right) \tag{4.7}$$

and the constants have values of $f_R = 0.18$, $\tau_1 = 12.2$ fs, and $\tau_2 = 32$ fs [61]. The spatial and temporal coupling constants are expressed as $gs = w_p^2 / \left(w_p^2 + w_s^2\right)$ and $g_t = T_p^2 / \left(T_p^2 + T_s^2\right)$, where the signal pulse duration T_s was assumed to be the same as the pump, and the signal beam focus w_s was calculated using ABCD resonator analysis (chapter 3) to be $w_s = 16$ μm. Typical values for the quantitites used in the above equations, are listed in Table 4.1.

The structure of the numerical model is visually represented in Figure 4.13, and can be summarised as follows:

1. Initial signal field is defined as random noise.

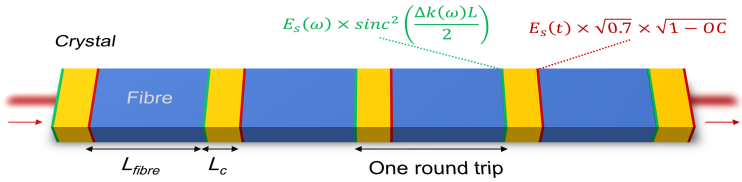

Figure 4.13: Schematic of the simplified model considered in the simulations. OC represents the fractional output coupler transmission (5% or 30%).

2. Signal field is convolved with parametric gain bandwidth in frequency domain (see Figure 4.3).

3. Propagation through nonlinear crystal (gain given by equation 4.4).

4. Signal field multipled by a constant corresponding to bulk fractional loss at output coupler and fibre coupling.

5. Passive propagation through fibre (gain set to zero).

6. Final field used as input to next round trip, with steps 2 to 6 repeated until steady state is reached.

Equation (4.3) was solved using the split-step Fourier method with a 4^{th} order Runge-Kutta algorithm applied for the nonlinear step, and initial perfect synchronisation of the signal to the cavity round-trip time was assumed [102]. As the dispersive and $\chi^{(3)}$ nonlinear effects are two orders of magnitude lower for the 2-mm-long nonlinear crystal section, compared to the 172-mm-long fibre section, dispersive and nonlinear terms were neglected over the crystal section when evaluating equation (4.3). Spectral and temporal grids contained 2^{11} data points, corresponding to a resolution of 4.2 fs in the time domain, and 1 nm in the spectral domain.

In a physical situation, pump depletion is significant and should also be considered, however, this model provided excellent agreement with experimental measurements.

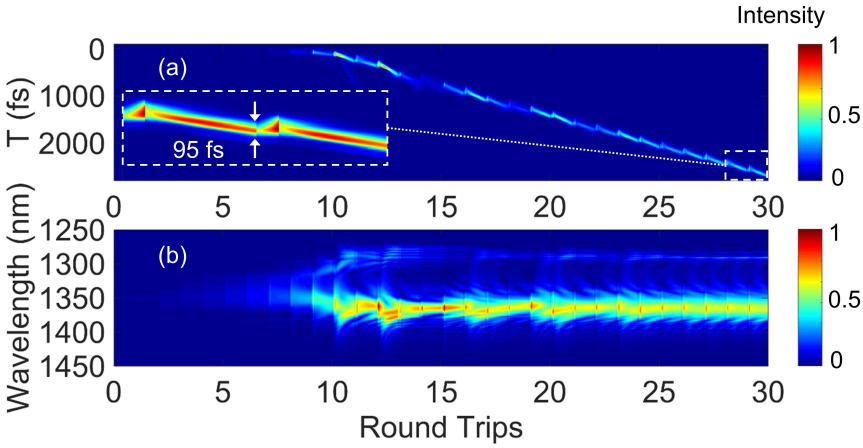

Figure 4.14: Simulation of a soliton pulse evolving from noise at an initial wavelength of 1350 nm, with ΔT_s free to adapt to the changing group velocity. Inset: Close-up of the final two round-trips at steady state, showing a pulse duration of 95 fs. (b) Corresponding spectral evolution showing the soliton self-frequency shift after 10 round trips.

4.4.2 Anomalous dispersion simulations

The simulation was first performed for an initial signal wavelength of $\lambda_s = 1350$ nm and a grating period of $\Lambda = 20.2$ μm. It was observed that once the fibre-coupled power surpassed a critical value, the spectrum broadened significantly and a fundamental soliton was emitted on the trailing edge of the pulse. The critical power was found to be that which exceeds the value for an $N^2 = 4$ at the given wavelength. The soliton is redshifted to a longer wavelength, λ_s', and propagates in the fibre at a slower group velocity relative to the 'cold-cavity' wavelength λ_s, subsequently falling out of synchronisation with the pump. If the cavity length is slightly shortened, i.e. by increasing the offset parameter, ΔT_s from zero, the pump pulse can resume synchronisation to this soliton at λ_s'.

Steady state is reached when ΔT_s is such that λ_s' and the intracavity power remain constant on consecutive round trips. The magnitude of ΔT_s required for a steady-state solution was found by initiating the simula-

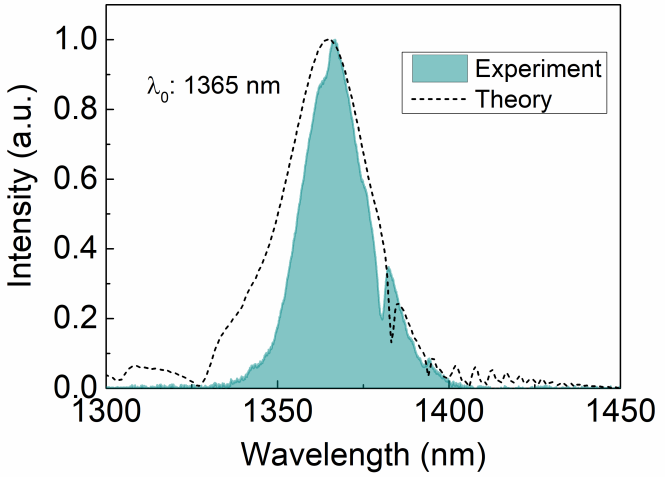

Figure 4.15: Comparison of steady state simulated spectrum, to the experimentally measured spectrum at the same wavelength.

tion with ΔT_s as a free parameter, with the resultant temporal and spectral evolution profiles shown in Figure 4.14(a) and (b), respectively. When the intracavity power surpasses the soliton threshold after 10 round trips, ΔT_s adjusts to match the new round-trip time, converging on a value of $\Delta T_s \sim$ 120 fs, which corresponds to a wavelength shift from 1350 nm to 1364 nm. Repeating the simulation at various wavelengths across $\lambda_s \sim$ 1300–1380 nm yields values of $\Delta T_s =$ 118–125 fs. The final field exhibits a $sech^2$ shape in the temporal domain. The steady state simulated spectrum shows close agreement with a typical experimental measurement, as shown in Figure 4.15, including fine modulation structure in the long wavelength wing. A temporal delay of $\Delta T_s = 120$ fs indicates an offset of $\Delta z \sim 36$ μm from the cold-cavity length, or a translation of M_3 by 18 μm. A schematic of the pulse evolution is shown in Figure 4.16. As the cavity is further shortened, the signal wavelength increases in accordance with increasing anomalous dispersion, suggesting that the offset from the cold-cavity wavelength remains constant.

Since the magnitude of β_2 increases almost linearly with wavelength,

Figure 4.16: Schematic of stable soliton formation: (1) Pulse builds from noise, (2) Pulse undergoes self-frequency shift (arrow indicates deceleration), (3) Cavity is delayed to resume synchronisation, (4) Synchronisation at λ_s' with a temporal offset ΔT_s from the cold cavity round-trip time.

the power contained within a fundamental soliton also increases linearly with wavelength. Furthermore, the soliton redshift and resultant temporal delay are known to be approximately proportional to the fibre-coupled power, for given dispersion and nonlinearity [61]. In order to determine the expected intracavity power as a function of wavelength, a simulation was performed using initial pulses corresponding to intracavity peak powers between 0 and 40 kW for wavelengths across 1300–1500 nm, and the steady-state spectral and temporal shifts identified. The resultant soliton central wavelength, λ_s', and physical cavity length offset, Δz, are plotted in Figure 4.17, which shows that for a fixed intracavity power, towards longer wavelengths the soliton temporal delay and required Δz rapidly decrease towards zero. Alternatively, for a fixed Δz, the intracavity power must increase in order to maintain synchronisation. The spots represent the experimental limits of tuning and the positions at which 2 kW intervals are crossed for a constant $\Delta z \sim 36$ μm.

Using the known losses at the output coupler and fibre coupling, these data points are compared to the experimentally measured peak power in Figure 4.18. Strong quantitive agreement is seen at shorter wavelengths, including the increase in power beyond ~1380 nm. The discrepancy at longer wavelengths could be explained by an increase in output coupler transmission, or reduced fibre attenuation. Also displayed is the experimentally observed hysteresis loop, with the blue shaded area representing wavelengths at which oscillation could be recovered. From Figure 4.3, it is seen that for a grating period of $\Lambda = 20.2$ μm, peak parametric efficiency occurs for wavelengths close to 1350 nm and falls to ~0.6 at 1460 nm. Therefore, the loss of oscillation beyond 1460 nm is attributed to insufficient gain to sustain the required intracavity power for synchronisation at $\Delta z = 36$ μm.

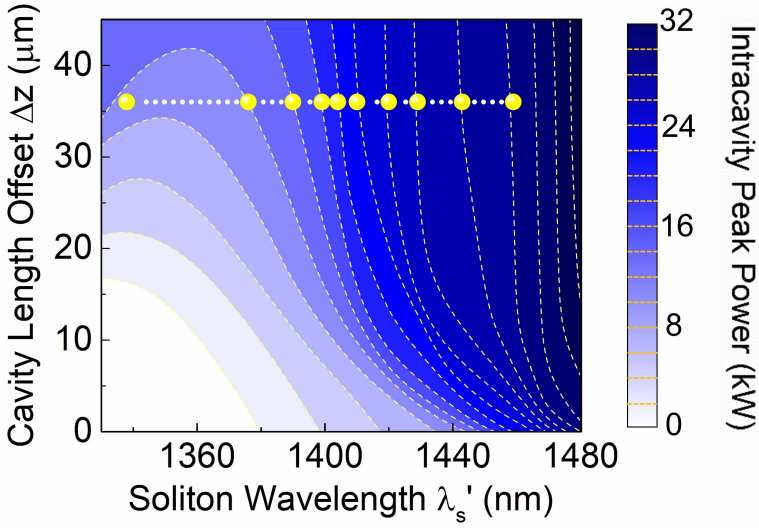

Figure 4.17: Cavity length offset Δz from the cold cavity length as a function of the shifted soliton wavelength λ_s', as a function of intracavity peak power between 0 and 32 kW. Yellow spots represent points at which 2 kW contours are crossed for $\Delta z = 36$ μm.

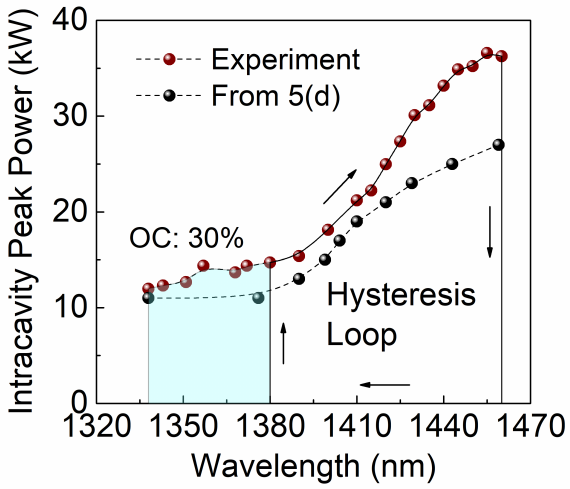

Figure 4.18: Experimentally measured intracavity peak power vs wavelength when tuning by cavity delay for a grating period of 20.2 μm, compared to values taken from Figure 4.17. Arrows represent observed power hysteresis loop, the blue zone represents wavelengths at which oscillation is recovered.

Once interrupted, the lower parametric efficiency and higher soliton threshold prevents the signal pulse train from recovering its previous power without first tuning the cavity length to synchronise to a wavelength in the blue zone. It is noted that oscillation is achieved without hysteresis across 1400–1700 nm for $\Lambda = 20.0$ μm, albeit with significantly reduced powers, suggesting that the offset from the cold-cavity length is negligible when oscillation is achieved on this grating period.

4.4.3 Spectral interference near degeneracy

Close to degeneracy, the cavity optical coatings ensure that both signal and idler are coupled into the fibre, although only the signal wave is synchronised to the cavity length. Simultaneously viewing both signal and idler spectra on a spectrum analyser revealed deep modulations in the idler spectrum, with the modulation period decreasing as the signal and idler separate from degeneracy. By varying the cavity length for a fixed grating period, the variation in spectral modulation as a function of wavelength can be observed. Figure 4.19(a) shows the idler spectrum as a function of cavity length, recorded beyond the degeneracy point, where the idler now corresponds to the shorter-wavelength pulse. Modulation arises a result of GVM between the signal and idler, leading to a temporal delay between the two pulses upon exiting the fibre. The Fourier transform of two closely spaced coherent pulses contains an interference term proportional to $cos(2\pi\nu t)$, where the modulation frequency, ν, is related to the pulse separation τ_{del} by $\nu = 1/\nu_{del}$. Such modulations are often observed in mode-locked fibre lasers supporting soliton molecules [103–105].

For two identical pulses with a well-defined phase relationship, the modulation depth is expected to be 100%. However, the position of the spectrum analyser (after the OC) allowed the detection of both a single-pass idler (not modulated) and a double-pass fibre-coupled contribution. By measuring the modulation period, $\Delta\lambda$, we were able to calculate the group delay between the two pulses and compare to that predicted by the dispersion relation of the fibre.

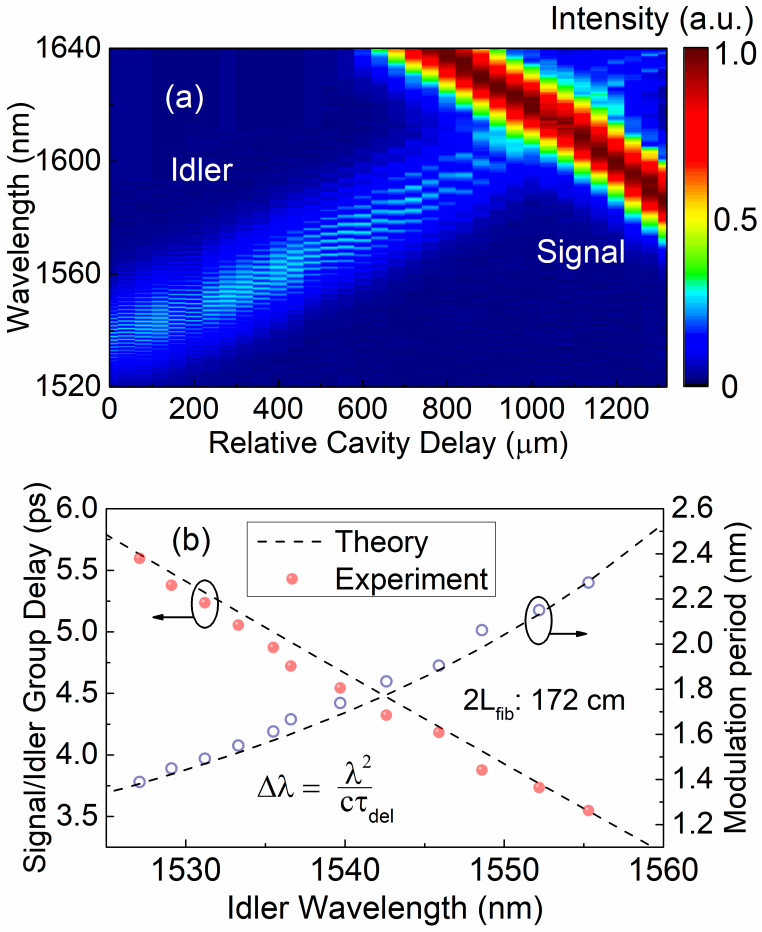

Figure 4.19: (a) Idler spectra recorded from $\lambda_i \sim 1527$ nm to degeneracy at ~1606 nm, showing the increase in modulation period $\Delta\lambda$. The signal spectrum also becomes visible as degeneracy is approached. (b) Comparison of experimentally determined $\Delta\lambda$, and relative signal/idler group delay, with the theoretical predictions.

In the absence of a full sellmeier equation for the fibre material, we calculated the effective group index as a function of wavelength using data from Figure 4.4, and considering the known fibre length of 86 cm, a cavity round trip time of 12.4998 ns, and quoted values of n_g(1310 nm) = 1.4676 and n_g(1550 nm) = 1.4682. The experimental data for group delay and modulation period as a function of wavelength is plotted against the theoretical prediction in Figure 4.19(b), where the additional delay from L_2, the output coupler, and 3 crystal passes was also considered. The GVD causes $\Delta\lambda$ to vary over the bandwidth of one pulse. So, the average value was extracted from the peak oscillation in the Fourier transform of each spectrum. The signal spectrum was not observed to be modulated, which we attribute to the washing out of fringes by parametric gain. In addition to the spectral interference, two co-propagating pulses of different wavelengths are also predicted to induce temporal modulation, however, we were unable to obtain autocorrelations at such low powers.

4.4.4 Normal dispersion simulations

Finally, we performed simulations of pulse evolution at wavelengths in the normal dispersion region, with an example at $\lambda_s \sim 1104$ nm shown in Figure 4.20(a) and (b). Steady state is obtained within ~25 round trips, and spectral sidebands are immediately evident after the first round trip. By comparing the simulated spectrum at the output coupler to an experimentally measured spectrum at the same wavelength, it can be seen in Figure 4.21(a) that the main features are accurately reproduced, including the wavelength offset of each sideband and the dip in the centre of the main lobe.

While Kelly sidebands in an anomalous dispersion fibre laser are produced by a phase-matched four-wave mixing process between co-propagating dispersive radiation and a periodically amplified soliton, here the finite temporal duration of each input pump pulse selectively amplifies certain spectral components of the resonating signal [96]. With fibre-coupled peak powers up to 18 kW across the normal dispersion region, the signal expe-

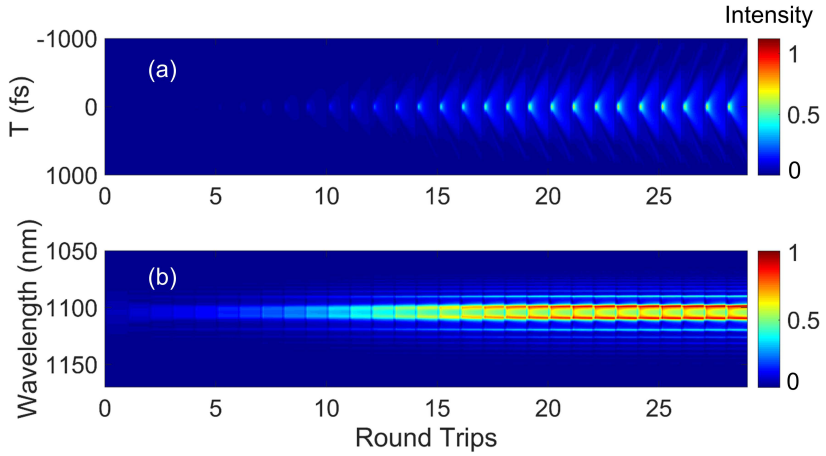

Figure 4.20: (a) Simulated temporal and (b) spectral evolution of a femtosecond pulse from noise in the OPO at a central wavelength of 1104 nm.

riences nonlinear phase shifts of up to 20π in each round trip, inducing a large chirp which in turn leads to temporal broadening of the pulse from ~100 fs to ~500–700 fs. Since only the central part of the broadened signal pulse experiences gain, the wavelengths contained within the central section of the pulse are selectively amplified. Therefore, the sideband separation is dependent on the pump pulse duration and the accumulated round trip dispersive and nonlinear phase shifts, which both increase at shorter wavelengths.

After amplification, the signal pulse resembles a narrow peak superimposed on a weak background of dispersive radiation. Comparison of experimental and simulated autocorrelation traces, shown in Figure 4.21(b) and (c) reveal a similar structure with estimated pulse durations of ~77 fs and ~85 fs respectively. The slight discrepancy can be attributed to the uncertainty of the experimental pulse shape, for which a $sech^2$ fit was applied.

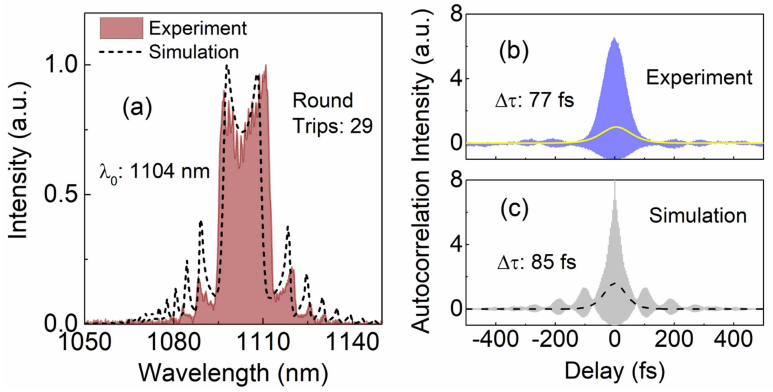

Figure 4.21: (a) Comparison of the steady state simulated spectrum with an experimentally measured spectrum at the same wavelength, (b) experimentally measured autocorrelation, and (c) simulated autocorrelation at the same wavelength.

4.5 Conclusions

We have demonstrated a compact, cost-effective and stable femtosecond laser source, generating tunable near-IR sub-100 fs pulses of up to 110 mW average power, by exploiting fibre-based soliton formation for the first time in a $\chi^{(2)}$ OPO. Using the rapid tuning methods of quasi-phase-matching and cavity length tuning, we achieved spectral coverage across 1051–1700 nm, enabling device characterisation in the presence of continually varying dispersion and nonlinearity. In the anomalous dispersion regime, transform-limited ~100 fs $sech^2$ pulses have been generated, while in the normal dispersion regime chirped pulses of ~80 fs were measured, and accompanied by rich spectral features.

The use of an off-the-shelf single-mode fibre with an integrated mirror reduced the required optics, enabled a footprint of only 30 × 40 cm, and led to passive power and wavelength rms fluctuations better than 0.3% and 0.015% respectively. Using a suitable dichroic mirror in place of M2, the mid-IR idler across 1.6–3.4 μm could also be extracted, which could be extended to even longer wavelengths using mid-IR non-oxide nonlin-

ear crystals such as $CdSiP_2$ and orientation patterned GaP. Practically, the device represents an attractive source for tabletop spectroscopy, nonlinear microscopy and seeding optical parametric amplifiers. Compared to a single pass soliton generation setup, no delay line is required to compensate for changing pulse delay with wavelength. In principle, the output power can be scaled arbitrarily by using looser crystal focusing, combined with stronger pumping and output coupling to ensure relatively low powers are returned through the fibre.

We have performed simulations based on the GNLSE to successfully recreate experimental observations, in both dispersion regimes. Future work will exploit fibres with varying dispersion profiles and higher nonlinearity, in order to further investigate power and hysteresis effects in the soliton regime, and even the possibility of intracavity supercontinuum generation. It is expected that a more rigorous theoretical analysis considering additional effects, such as pump depletion and group velocity mismatch, will yield even closer quantitive agreement with spectral features, and enable analytical expressions for pulse duration and sideband positions to be derived in the normal dispersion regime.

5 Low threshold, high efficiency, group velocity-matched mid-IR OPO

This chapter constitutes the following publication:

1. *Low threshold, highly efficient, tunable mid-infrared optical parametric oscillator exploiting group-velocity matching in MgO:PPLN* **C. F. O'Donnell**, S. Chaitanya Kumar, and M. Ebrahim-Zadeh (To be submitted).

5.1 Background

Mid-infrared femtosecond laser sources are of great interest across many research fields, including frequency comb generation, pump-probe spectroscopy, and materials science [106–108]. In the high-repetition-rate regime (~100 MHz), devices based on nonlinear frequency conversion, such as synchronously-pumped optical parametric oscillators (OPOs) are unrivalled in their ability to generate kW level pulse trains of quasi-CW light across 1–12 μm, with pulse durations able to reach as short as a few optical cycles [28, 33, 109]. The atmospheric transmission window covering 3–5 μm coincides with onset of the molecular fingerprint region, which contains strong vibrational resonances of hazardous gases such as CH_4, SO_2 and CO. Across this spectral region, OPOs are mature technology, capable of producing watt-level average power by pumping nonlinear crystals such as MgO-doped periodically poled $LiNbO_3$ (MgO:PPLN) and $KTiOPO_4$ (KTP) with well-established Ti:sapphire oscillators and Yb fibre lasers [110].

In spite of this, femtosecond OPOs struggle to reach the conversion efficiencies of their picosecond and CW counterparts, primarily due to more pronounced temporal walk-off between the pump, signal and idler pulses, which propagate with mismatched group-velocities through the nonlinear crystal. In the spectral domain, this is manifested as a narrow acceptance window for pump frequencies which can be efficiently down-converted to the signal and idler frequencies. While this does not pose a problem for

relatively narrowband picosecond lasers, a transform-limited 100 fs pulse at 1064 nm spans a FWHM bandwidth of $\Delta\lambda \sim 12$ nm, far greater than the pump acceptance bandwidth afforded by most nonlinear crystals longer than a few mm. However, exceptions to this general rule arise in several crystals, where the dispersion profile is such that the pump and idler group velocities are equal at wavelengths which satisfy phase-matching [111]. The pump acceptance bandwidth, $\Delta\lambda_p$, can be calculated for a crystal of length L by using a Taylor expansion of the phase-matching condition and retaining terms to second order

$$\frac{2\pi cL\left|GVM_{pi}\right|}{\lambda_p^2}\Delta\lambda_p + \frac{L}{2}\frac{\partial^2(\Delta k)}{\partial\lambda_p^2}\Delta\lambda_p^2 = 5.56 \tag{5.1}$$

When the pump-idler group-velocity mismatch, GVM_{pi}, is zero, the crystal length has a weaker influence on the pump acceptance bandwidth ($\Delta\lambda_p \propto L^{-1/2}$ rather than $\propto L^{-1}$), relaxing the restriction of narrowband pumps for long crystals.

Figure 5.1 shows the calculated signal parametric gain map for a 42-mm-long MgO:PPLN crystal with four quasi-phase matched (QPM) grating periods of $\Lambda = 28.5$ μm, 29 μm, 29.5 μm, and 30 μm, calculated using the Sellmeier equations in [99] at a fixed temperature of 100°C. The dashed lines represent pump and signal wavelengths corresponding to pump and idler pulses with zero group velocity mismatch (GVM) for each grating period. It is evident that $\Delta\lambda_p$ rapidly increases to 14 nm (FWHM) as the signal moves towards the critical wavelength (the inflection points), whereas elsewhere it is >1 nm. Conversely, at the zero GVM points, the signal parametric gain bandwidth, $\Delta\lambda_s$, becomes narrow, implying that the pump bandwidth is primarily transferred to the idler.

A CW OPO exploiting this principle was reported, using a 8.3 nm linewidth Yb fibre laser at 1064 nm to pump a 50-mm-long MgO:PPLN crystal containing a quasi-phase-matched (QPM) grating period of $\Lambda = 30$ μm, heated to 100°C, leading to the generation of 5.3 W of broadband mid-IR light centred at 3454 nm and spanning 76 nm at FWHM [111]. In addition, studies of an ultrafast MgO:PPLN OPO synchronously pumped by

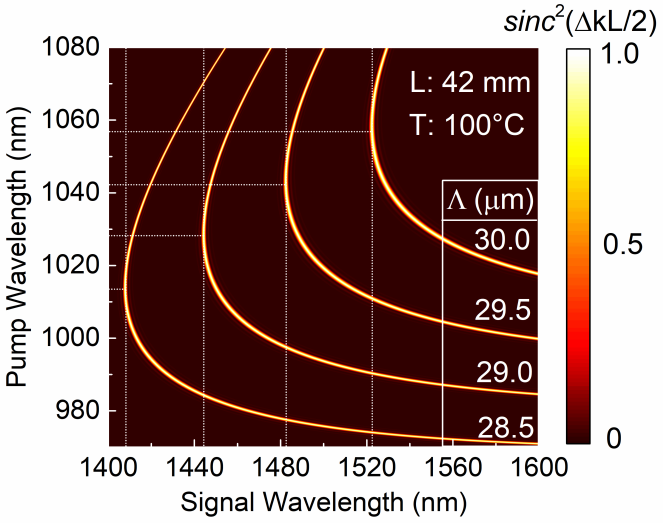

Figure 5.1: Parametric gain map for a 42-mm-long MgO:PPLN crystal at 100°C containing 4 QPM grating periods. Dashed lines represent the pump and signal wavelengths corresponding to group velocity matching between the pump and idler waves.

spectrally broadened 4 ps pulses at 1.047 μm confirmed that when operating in the zero GVM regime, spectral information is transferred from the pump to idler with high fidelity [112]. Similarly, the broad acceptance bandwidth enabled highly chirped 3 ps pulses from an Yb fibre amplifier to be used to directly pump an OPO based on a 25-mm-long MgO:PPLN crystal, without spectral pre-compression [113]. Finally, it was demonstrated that under group-velocity matched conditions, a 50-mm-long MgO:PPLN crystal could be pumped with 220 fs pulses from a 5 W, 78 MHz Yb fibre laser to produce up to 0.54 W tunable across 3342–4229 nm in a single-pass optical parametric generation (OPG) setup [114].

Here we report, to the best of our knowledge, the first widely tunable femtosecond OPO based on the principle of group-velocity matching in a 42-mm-long MgO:PPLN crystal, where we exploit a tunable femtosecond laser to pump at all wavelengths of maximum spectral acceptance, shown in Figure 5.1. In doing so, we observe lower oscillation thresholds and higher conversion efficiencies as compared to conventional devices, due to utilising a far longer interaction length than possible under normal conditions. The ability to rapidly tune across the mid-IR using pump wavelength variation is exploited to perform transmission spectroscopy of methane in the 3.3 μm spectral region.

5.2 Experimental setup

The experimental setup for the group-velocity matched femtosecond OPO is shown in Figure 5.2. A tunable femtosecond laser system (Radiantis, *Blaze*), consisting of an integrated Ti:sapphire laser and synchronously-pumped OPO, is used as the pump source, providing transform-limited 80–100 fs pulses at 80 MHz across 990–1550 nm in the near-IR with up to 500 mW average output power [115]. For this experiment, only wavelengths across 997–1070 nm were used. The beam is focused using an $f = 100$ mm lens to a waist radius of $w_0 \sim 22$ μm in the centre of a 42-mm-long MgO:PPLN crystal cut at $\theta = 90°$ for type-0 ($e \rightarrow ee$) phase-matching, corresponding to equal confocal parameters for the pump and

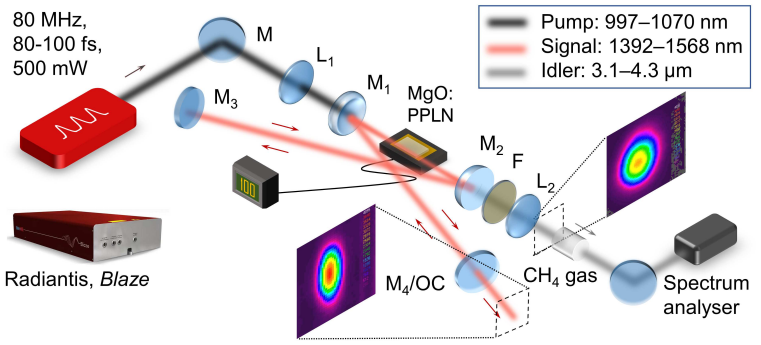

Figure 5.2: Experimental setup of the group-velocity-matched femtosecond OPO. M: mirrors, L: lenses, F: long-pass filter, OC: output coupler.

signal ($b_p \sim b_s$). The crystal contains 7 separate channels across its transverse aperture with QPM grating periods increasing from $\Lambda = 28.5$ μm to 31.5 μm in steps of 0.5 μm, and is mounted on a temperature-stabilised oven (stability 0.1°C). Since the anti-reflection coating is optimised for 1064 nm pumping, single-pass pump transmission losses vary from ~50% at 1000 nm to < 1% at 1070 nm, whereas for the signal $T > 99\%$ across all wavelengths. Two concave spherical mirrors M_{1-2} ($r = 100mm$) form the intracavity focus, M_3 has $R > 99.9\%$ across 1300–1650 nm, and M_4 is a 5% signal output coupler mounted on an electronic translation stage for fine control of synchronisation. M_1 is coated for high transmission of the pump ($T > 90\%$ at 1000 nm, $T \sim 70\%$ at 1070 nm), and high reflection of the signal ($T > 99\%$ across 1300–1500 nm). M_2 is coated for high reflection of the signal ($T > 99\%$ across 1300–1500 nm), and high transmission of the idler ($T > 90\%$ across 3000–5000 nm), ensuring singly-resonant operation for the signal. The single-pass idler is collimated by a second $f = 100$ mm lens, L_2, before transiting through a long-pass (> 2.4 μm) filter, F, then a 5-cm-long methane gas cell, followed by entering an optical spectrum analyser.

5.3 Results

5.3.1 Cavity length tuning

After alignment, the OPO was characterized for each grating period from $\Lambda = 28.5$ μm to 31.5 μm by measuring the signal and idler power as a function of pump wavelength and cavity detuning. Figure 5.3 shows plots of the signal and idler power (triangles) as the cavity length was adjusted, while operating at the optimum pump wavelength for each grating period. Also plotted is the signal central wavelength (circles), extracted from each individual spectrum using a centre-of-mass averaging algorithm. The dotted lines represent signal wavelengths corresponding to points of inflection in Figure 5.1. Remarkably, the observed signal remains locked in good agreement with this wavelength for the majority of the synchronisation length, during which time the signal and idler powers steadily increase. This is in contrast to standard femtosecond OPOs, where the wavelength continually adjusts according to crystal dispersion in order to match perfect synchronisation, but consistent with previous observations near zero GVM [113]. After translating M_4 a critical distance, the wavelength begins to follow the cavity dispersion profile, accompanied by a rapid decrease in output power and an increase in signal bandwidth. Since significant GVM exists between the pump and signal ($GVM_{ps} = 109$ fs/mm for $\lambda_p = 1030$ nm, $\lambda_s = 1450$ nm), the effective interaction length for the two pulses is ~4.6–5 mm depending on wavelength, such that the signal pulse walks through the pump inside the crystal. For a shorter cavity, this interaction length occurs near the beginning of the crystal, but maximum efficiency is achieved when overlap coincides with the beam focus. Detuning beyond this position causes the wavelength to shift in order to preserve synchronisation at the focus.

5.3.2 Pump tuning

The zero GVM condition can be adjusted by variation of crystal temperature, however this is a slow process. A faster tuning method is to vary the

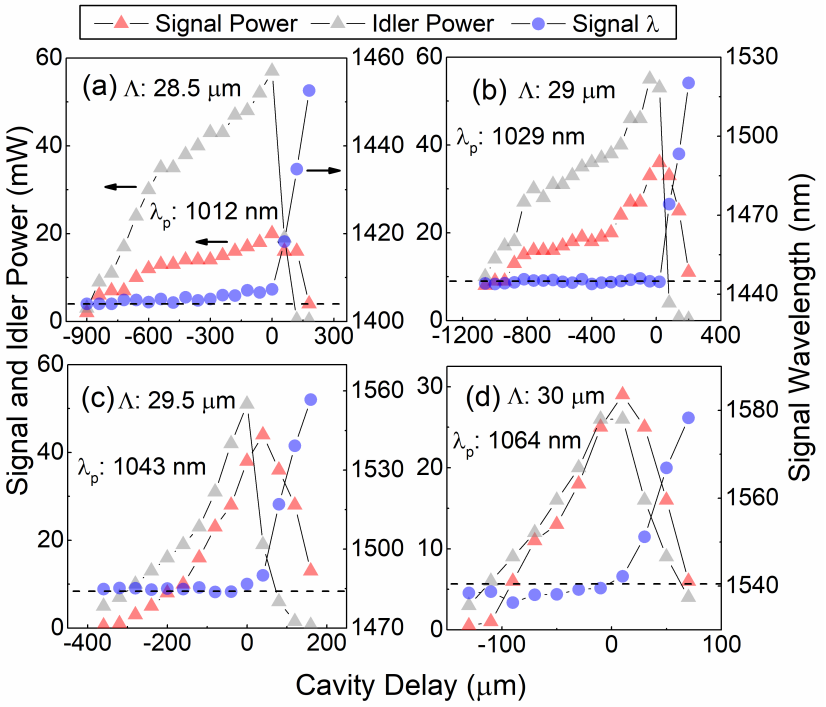

Figure 5.3: Cavity delay tuning of the OPO for grating periods of (a) 28.5 μm, (b) 29 μm, (c) 29.5 μm, and (d) 30 μm, with the signal and idler powers plotted as triangles and the signal wavelength as circles. Dotted lines represent calculated signal wavelengths corresponding to zero GVM between the experimentally determined optimum pump wavelength (shown on figure) and the idler.

pump wavelength, which leads to a linear variation in the idler wavelength, as the signal wavelength is found to remain fixed at the value which yields the maximum pump acceptance bandwidth. The dependence of the idler power and wavelength on the pump wavelength is plotted in Figure 5.4 for $\Lambda = 28.5$ μm, where it is seen that maximum power of 57 mW is generated for λ_p close to the value calculated in Figure 5.1, indicated by the dotted line. The idler central wavelength can be rapidly tuned across 3439–4087 nm at T = 100 °C, extending to 4273 nm at T = 25°C. Using the $\Lambda = 30$ μm grating period at T = 200°C, the pump tuning window could be shifted to 3132–3420 nm. With a grating period of $\Lambda = 28$ μm, it would be possible to reach 4500 nm, a region difficult to access in conventional MgO:PPLN OPOs. Power is limited on the short wavelength side by poor transmission of M_1 for $\lambda_p > 1070$ nm. The optimum pump wavelength does not always correspond to the exact value predicted by the Sellmeier equations, likely due to a combination of wavelength dependence of pump laser power, and the optical coatings of M_1 and the crystal.

5.3.3 Power and efficiency

A major advantage of utilizing a long nonlinear crystal is improvement in conversion efficiency, which we measured by performing power scaling measurements, a typical example of which is shown in Figure 5.5. We observed oscillation thresholds as low as 5 mW, even with round trip signal losses of ~30%. Signal and idler slope efficiencies were found to be 11.1% and 15.4% respectively, where the pump power was corrected for transmission loss through M_1 only. With 419 mW at 1023 nm incident on the crystal, the pump depletion was determined to be 78%, and 61 mW of idler power at 3369 nm was measured, equivalent to a quantum conversion efficiency of 47.9%. Using the Manley-Rowe relation and the pump depletion value, it is calculated that 71 mW of idler is produced, and residual losses contributed by M_2, L_2, and the long-pass IR filter account for the discrepancy. For comparison, a typical femtosecond OPO based on a

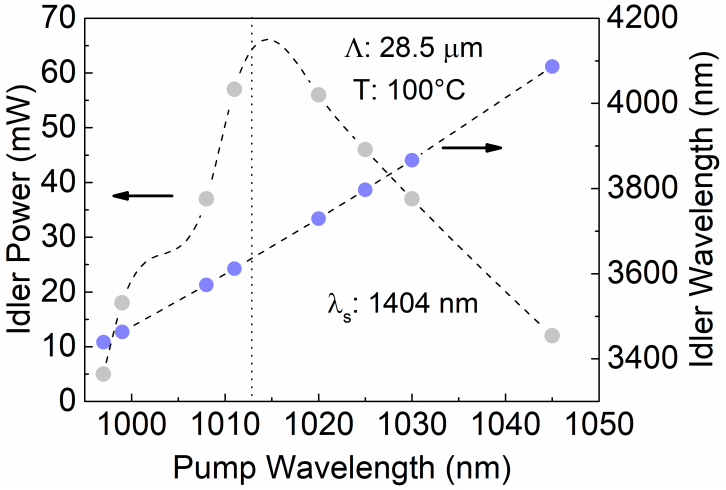

Figure 5.4: Power and idler wavelength dependence on pump wavelength for $\Lambda = 28.5\ \mu$m, with predicted optimum pump wavelength indicated by dotted line.

1-mm-long MgO:PPLN crystal has a threshold of ~50 mW and an idler slope efficiency of ~12 %, meaning the group-velocity matched provides a twofold improvement in output power at a pump power of 419 mW [110]. The signal power could be increased to 76 mW at the expense of the idler by increasing the output coupling from 5 % to ~13 %. Due to the large parametric gain, it is likely that the OPO could support far higher signal output coupling, however we were unable to characterise this due to a lack of suitable output couplers. Also shown in the inset to Figure 5.5 is the pump spectrum recorded while the OPO was on (shaded area) and off (dotted line), indicating that depletion occurred over the entire spectral bandwidth. We recorded a maximum idler power of 65 mW at 3610 nm, with 20 mW available at 3231 nm and 12 mW at 4180 nm.

Furthermore, the device operated with high long-term passive power stability, with rms fluctuations of 0.81 % and 0.76 % measured over 1 hour for the signal and idler respectively, as displayed in Figure 5.6. This is a result of the device preferentially operating at the group-velocity-matched

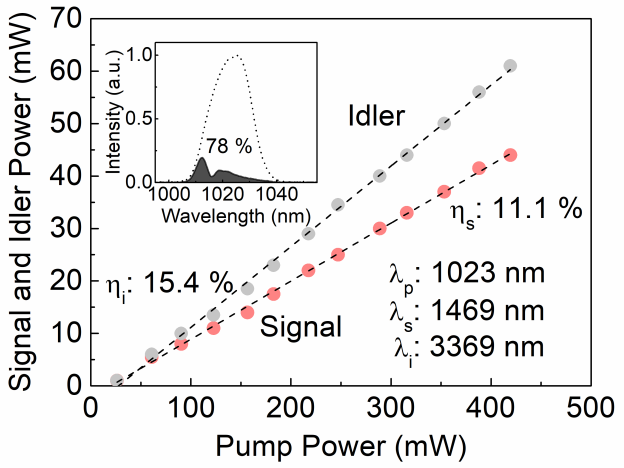

Figure 5.5: Power scaling of the device with signal and idler wavelengths of 1469 nm and 3369 nm, respectively.

wavelengths, even when the cavity length is subject to significant perturbation (as presented in Figure 5.3).

5.3.4 Spectral and temporal characteristics

Pulse durations of the pump and signal, determined using interferometric autocorrelation, are shown in Figure 5.7(a) and (c), respectively. The corresponding spectra are shown in Figure 5.7(b) and (d), with the calculated phase-matching bandwidths also plotted as dotted lines. When calculating the pump acceptance bandwidth in Figure 5.7(b), a $sech^2$ signal pulse of 3 nm bandwidth at 1459 nm was assumed, and likewise to calculate the signal gain bandwidth in (d) the measured pump bandwidth of 13.8 nm was used. Lying in the range ~400–600 fs, signal pulses are significantly broader than the pump, due to a combination of pump-signal GVM, self-phase-modulation (SPM), and group delay dispersion ($GDD = 14793$ fs^2 at 1300 nm, 7463 fs^2 at 1600 nm). Despite this, it is clear that the signal spectrum is constrained by the gain bandwidth, resulting in pulses close to the transform limit ($\Delta\nu\Delta\tau \sim 0.315$). Without access to a suitable mid-IR

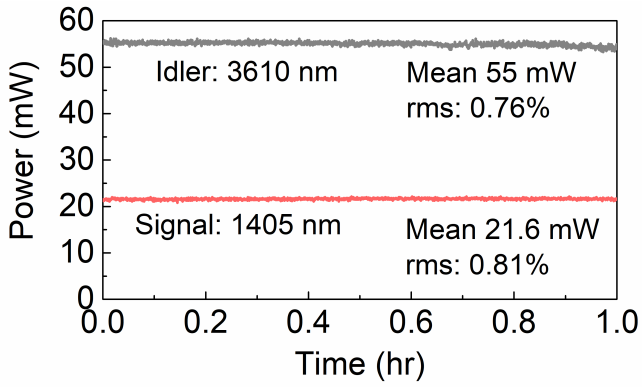

Figure 5.6: Passive signal and idler power stability over one hour.

autocorrelator, we were unable to measure the idler pulse durations. However, an estimation can be made based on a convolution integral between the signal and idler fields, which yields a duration in the range 440–630 fs.

The idler spectrum was measured using a He-Ne calibrated Fourier-transform wavemeter with resolution ~3 nm. As shown in Figure 5.8, the FWHM was measured to be within the range 140–180 nm, dependent on the bandwidth of the pump. Note the shortest-wavelength idler spectrum exhibits strong asymmetry, due to the corresponding pump wavelength containing similar SPM induced features [112]. Using the pump and signal data from Figure 5.7(b) and (d), in conjunction with the Manley-Rowe relation, yields a calculated idler bandwidth of 151 nm, in strong agreement with the measured value of 164 nm from a simultaneously recorded idler spectrum. The lack of idler spectral broadening is indicative of negligible GVM between the pump and idler waves.

5.3.5 Spectroscopy

Finally, we demonstrate the suitability of our source for spectroscopy, by performing transmission measurements of a 5-cm-long gas cell containing CH_4/N_2 partial pressures of 10%/90%, respectively. The broadband nature of the idler enables multiple vibrational modes to be probed simul-

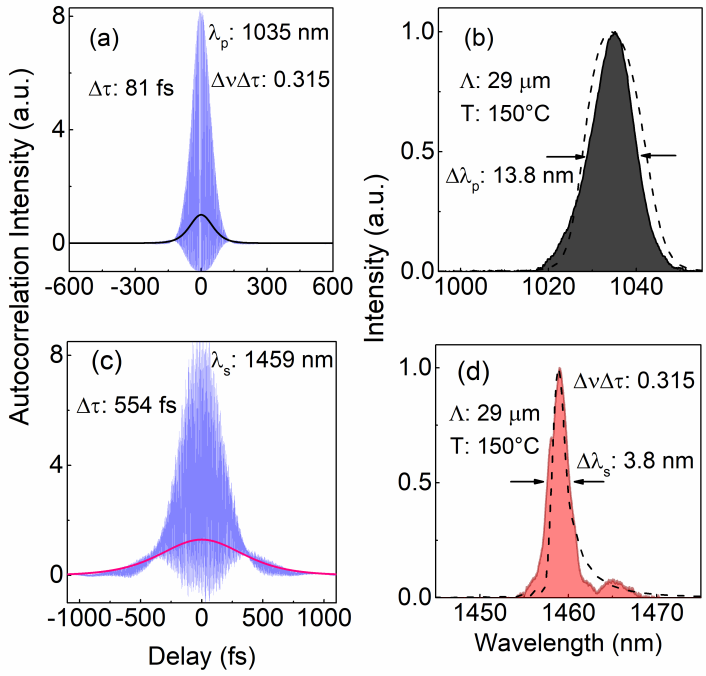

Figure 5.7: (a) Pump autocorrelation trace at $\lambda_p = 1035$ nm, (b) corresponding spectrum, compared to the calculated acceptance bandwidth (dashed line), (c) signal autocorrelation trace at $\lambda_s = 1459$ nm, (d) corresponding spectrum compared to the parametric gain bandwidth.

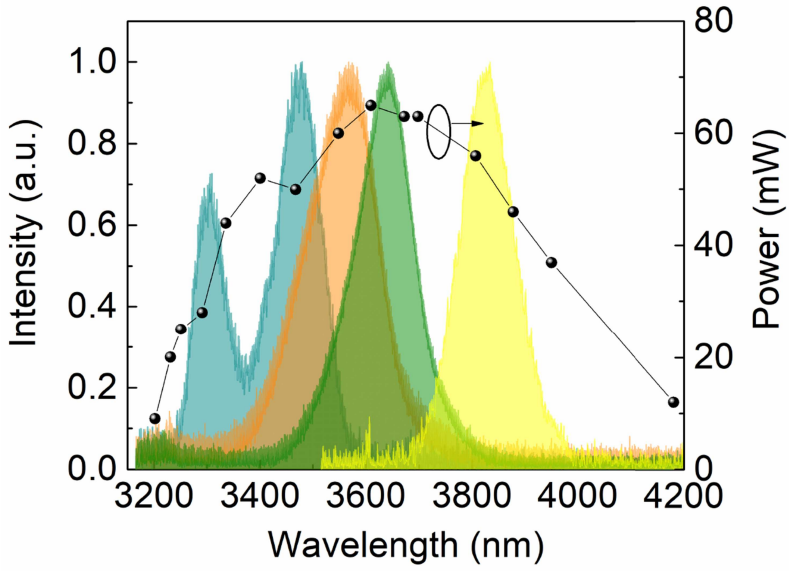

Figure 5.8: Idler spectra and average power across the tuning range.

taneously, as shown in Figure 5.9, where data recorded from the spectrum analyser at a fixed central idler wavelength (blue), is compared to the HITRAN database (red). Scanning the pump wavelength enables the full region of interest to be covered in a few seconds.

5.4 Conclusions

In summary, we have demonstrated an efficient femtosecond OPO, tunable across 1392–1568 nm in the near-IR and 3132–4273 nm in the mid-IR, based on the novel concept of group-velocity matching between pump and idler pulses in a 42-mm-long MgO:PPLN crystal. The device produces up to 65 mW average mid-IR power at 80 MHz repetition rate in sub-picosecond pulses, with FWHM bandwidths of 140–180 nm, depending on the bandwidth of the pump. By ensuring three-wave interact over an extended crystal length, we achieve quantum conversion efficiencies up to 47.9% from the near-IR to mid-IR. The low threshold of ~5 mW and high

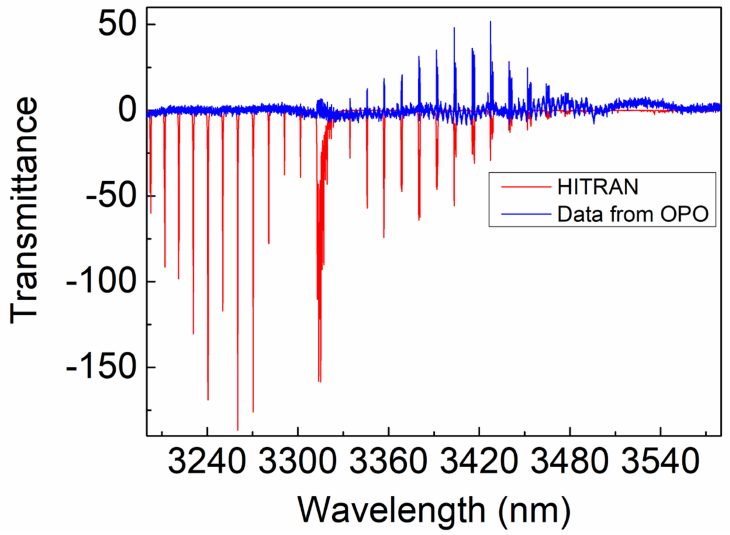

Figure 5.9: Transmission spectroscopy of CH_4 using OPO idler output, compared to the HITRAN database.

slope efficiency allows the possibility of direct pumping with low-power femtosecond fibre seed oscillators, to generate a tunable mid-IR seed for optical parametric amplifiers. The device is found to preferentially operate at the zero GVM condition over a large cavity synchronisation length, leading to high passive power and wavelength stability.

Signal pulses are measured to be transform-limited, due to restricted gain bandwidth, which facilitates effective parametric transfer to the idler. Wavelength flexibility of the pump enabled optimisation of output power for each grating period, and also rapidly tune across mid-IR spectral regions, which we exploited to perform simple spectroscopy of methane. Efficiency could be further improved using optimised optical coatings, and alternative cavity mirrors, in order to achieve the ideal Boyd-Kleinmann focusing parameter of $\xi = 2.84$. Further experiments will study pumping alternative nonlinear crystals, such as periodically poled $LiTaO_3$ and orientation-patterned GaP, in a group-velocity matched configuration, in

order to achieve boosted efficiency at challenging wavelengths in the deep mid-IR.

6 Single-stage Ti:sapphire pumped OPO based on $CdSiP_2$

This chapter constitutes the following publications:

1. *Critically phase-matched Ti:sapphire-laser pumped deep-infrared femtosecond optical parametric oscillator based on $CdSiP_2$*
   C. F. O'Donnell, S. Chaitanya Kumar, K. T. Zawilski, P. G. Schunemann and M. Ebrahim-Zadeh
   Optics Letters **43**, 1507–1510 (2018).

2. *Single-Stage Ti:Sapphire-Pumped Deep-Infrared Optical Parametric Oscillator Based on $CdSiP_2$*
   C. F. O'Donnell, S. Chaitanya Kumar, K. T. Zawilski, P. G. Schunemann and M. Ebrahim-Zadeh
   IEEE Journal of Selected Topics in Quantum Electronics **24**, 1–9 (2018).

6.1 Background and motivation

For as long as infrared spectroscopy has been practised, the spectral region from 4–12 μm in the mid-infrared (mid-IR) to deep-infrared (deep-IR) has been of utmost interest due to the presence of strong absorption peaks corresponding to the fundamental vibrational modes of numerous common molecules [116]. Where these peaks coincide with the atmospheric transmission windows across 3–5 μm and ~7.5–12 μm, there exists the possibility to easily and unambiguously identify the concentrations of individual compounds through the strength of their molecular fingerprint. Today, there is a wide range of applications based upon this principle, including microscopy, security, medical imaging and surgery [117–120]. The workhorse for such applications has long been Fourier Transform Infrared Spectroscopy (FTIR), involving the illumination of a sample using a broadband IR source such as a globar. Although spectral coverage is broad, the

diffuse and incoherent nature of the light source places limitations on the achievable spatial resolution and signal-to-noise ratio [121].

In the absence of conventional solid-state lasers at these wavelengths, a variety of different approaches towards the development of high-power coherent mid-IR and deep-IR sources have been explored. The high average power and spectral brightness of a synchrotron source is one solution, but with the disadvantage of large size, requirement for in-situ measurements, and restricted beam time. Quantum cascade lasers are available across the mid-IR and deep-IR, however, the inability to generate pulses shorter than a few nanoseconds limits their peak power, and the attainment of wide tunability requires multiple laser chips [122]. Broad spectral coverage can be obtained from supercontinuum sources, albeit at low spectral intensity, while reaching the crucial wavelengths requires powerful pump sources in the mid-IR, increasing cost and complexity [123].

On the other hand, nonlinear parametric down-conversion techniques can exploit well-established near-IR solid-state and fibre laser technology to generate powerful coherent radiation far into the infrared [33]. Furthermore, the temporal qualities of the pump laser are transferred to the down-converted beams, enabling high-repetition-rate quasi-continuous-wave pulse trains with kW-level peak power. Such sources are most commonly realised using difference-frequency-generation (DFG), optical parametric generation (OPG) or optical parametric oscillators (OPOs) based on suitable mid-IR nonlinear crystals. In such processes, varying the crystal refractive index or input beam wavelength enables single device tuning over a very broad spectral range. The DFG process has the advantage of a single-pass arrangement, but two pump sources closely spaced in wavelength are required to reach the deep-IR. By performing DFG between the signal and idler of OPOs synchronously pumped by Ti:sapphire or Yb fiber laser, or using seeded optical parametric amplifiers (OPAs), milliwatt-level average power femtosecond pulses have been produced across 4–12 μm [124, 125]. However, this method incorporates two frequency conversion stages, leading to a costly setup and low overall efficiency.

While commercial OPOs are capable of directly producing hundreds of milliwatts of average power up to ~4.5 μm in the mid-IR, efforts to advance their wavelength access into the deep-IR have been hampered by stringent nonlinear crystal requirements. The necessary material properties include a high nonlinear coefficient, d_{eff}, resistance to damage at high optical intensities, bulk transparency, and ability to be phase-matched at the desired pump, signal and idler wavelengths. The search for nonlinear crystals which simultaneously satisfy all criteria has been challenging; oxide-based crystals (e.g., $LiNbO_3$, $KTiOPO_4$, $RbTiOAsO_4$, $CsTiOAsO_4$) perform well when pumped by ~1 μm lasers, but are limited to output below ~4.5 μm by multiphonon absorption. On the other hand, almost all highly nonlinear non-oxide crystals (e.g., $AgGaSe_2$, GaAs, $ZnGeP_2$) have narrow optical bandgap resulting in strong two-photon absorption below ~1.5 μm. In general, there has been shown to be a negative correlation between the size of the bandgap and the magnitude of d_{eff} [126]. The breakthrough finally came by the successful development of cadmium silicon phosphide, $CdSiP_2$ (CSP), a chalgocenide crystal which was first grown to sufficient optical quality in 2010 [36]. With a nominal transparency across 1–7 μm, thermal conductivity of 13.6 W/m·K, and $deff \sim 84$ pm/V, it enables single-stage conversion from 1.06 μm to the mid-IR and deep-IR [127]. Moreover, its nonlinear figure of merit ($FOM = d_{eff}^2/n^3$) ranks among the highest of all existing nonlinear crystals. The potential of CSP was first demonstrated through picosecond OPG and OPOs at low repetition rates [128–130], before high-repetition-rate femtosecond OPOs were subsequently reported [27, 131–133]. Figure 6.1(a) shows the group velocity mismatch (GVM) between the interacting pump, signal and idler waves, and the signal group velocity dispersion (GVD) across the range 1100–1200 nm, relevant for OPOs pumped near 1 μm.

The GVM between pump and signal varies over 134–312 fs^2/mm, implying that the effective temporal interaction length is 0.4–1 mm for ~130 fs pulses. In such short crystals, the parametric gain remains very high, due to the large d_{eff} and high peak intensities involved. As a birefringent crystal, under type-I critical phase-matching ($e \rightarrow oo$), the extraordinarily

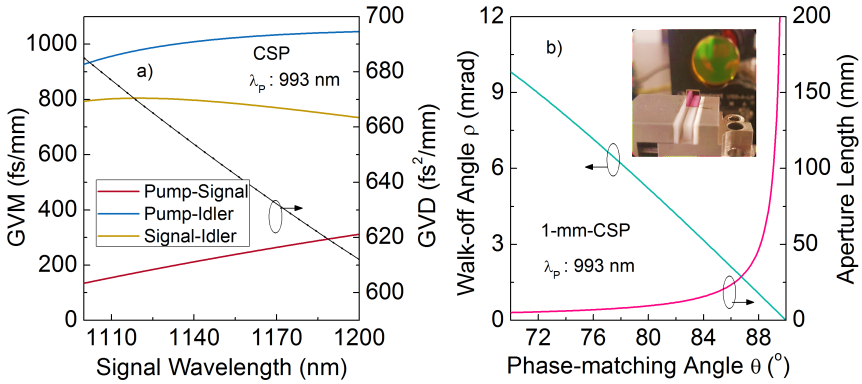

Figure 6.1: (a) GVM between the pump at 993 nm, signal and idler, and GVD across 1100–1200 nm. (b) Spatial walk-off and aperture length for a phase-matching angle from θ = 70° to 90°.

polarised wave will experience a spatial walk-off at angle ρ, leading to an effective parametric interaction length (aperture length) of $l_a = \sqrt{\pi} w_0/\rho$, where w_0 is the beam waist. The magnitude of ρ and l_a for a focused pump beam waist of w_0 = 28 μm, are shown in Figure 6.1(b), as a function of phase-matching angle, θ, for a 1-mm-long crystal under type-I phase-matching ($e \rightarrow oo$) pumped at λ = 993 nm. As the phase-matching angle is reduced from θ = 90° to 70°, the aperture length decreases down to ~5 mm. Therefore, even at large crystal rotation angles, the spatial walk-off does not become a limiting factor for parametric generation.

6.2 Single-stage femtosecond parametric sources beyond 4 μm

The emergence of femtosecond mode-locked Yb, Er, and Tm fiber lasers at ~1 μm, ~1.56 μm and ~2 μm, respectively, has greatly expanded the repertoire of suitable pump sources, finally enabling direct pumping of the established IR crystals, $AgGaSe_2$ and OP-GaAs. Together with the genesis of CSP, and even more recently, orientation-patterned GaP (OP-GaP), the

past few years have seen numerous breakthroughs in the field of single-stage deep-IR frequency conversion, the extent of which are summarised in Table 6.1.

In this work, we add another important milestone to this list, by demonstrating a deep-IR femtosecond OPO based on CSP, pumped directly at by a Kerr-lens-mode-locked (KLM) Ti:sapphire laser, for the first time. In doing so, we show that deep-IR radiation can be generated in a single conversion stage using a well-established ultrafast pump laser technology. The deployment of the KLM Ti:sapphire laser also offers the important advantage of pump wavelengths <1 μm, which enables the generation of longer idler wavelengths in the deep-IR. This is illustrated in Figure 6.2, where the signal and idler wavelength tuning as function of the CSP phase-matching angle under critical type-I ($e \rightarrow oo$) phase-matching for various discrete pump wavelengths of interest, from Yb-based solid-state and fibre lasers down to the Ti:sapphire laser, is presented. As can be clearly seen, for all phase-matching angles (including $\theta = 90°$ at NCPM), longer deep-IR idler wavelengths can be generated by deploying shorter pump wavelengths in the Ti:sapphire laser tuning range. The versatility of the KLM Ti:sapphire pump laser, in combination with the excellent optical properties of CSP, enable us to achieve deep-IR tuning across 6654–8373 nm using a combination of pump wavelength tuning, angle tuning under type-I critical phase matching, and cavity delay tuning. We have been able to generate up to 20 mW of deep-IR average power at 7314 nm at 80.5 MHz pulse repetition rate, in TEM_{00} spatial beam quality. Moreover, up to 37 mW is also available in the near-IR signal, with pulse durations measured from 259 to 319 fs. To the best of our knowledge, these results represent the first demonstration of practical powers beyond >7 μm fromany Ti:sapphire-laser-pumped OPO with no intermediate frequency conversion stage, and the longest wavelengths generated using CSP to date.

Pump	Rep. rate (MHz)	Crystal	Tuning method[a]	Idler (μm)[b]	Pump power (**W**) (Wavelength (nm))	Idler power (**mW**) (Wavelength (μm))[c]	Idler duration (fs)	Ref.
Ti:sapphire	80	CSP	P, A, C	6.7–8.4	**0.83** (993–1011)	**20** (7.3), 7 (8.1)	∼300 (est.)	This work
Yb:KGW	43	CSP	C	6.8–7.0	**5** (1029)	**110** (7.0)	∼500 (est.)	[27]
Er Fibre laser	100	$AgGaSe_2$	A	4.8–6.0	**0.3** (1560)	**18** (5.0)	∼180	[135]
Ti:sapphire	84	MgO:PPLN	Q, C	2.8–6.8	**1.5** (810)	**11** (5.3), **0.2** (6.5)	∼150 (est.)	[136]
Yb fibre laser	100	OP:GaP	Q	5.0–12	**2** (1040)	**55** (5.0), **15** (8.5), **7.5** (12)	≥150	[28]
Tm fibre laser	75	OP:GaAs	-	4.1 (2.6–6.1) bandwidth	**1** (2050)	**37** (2.6–6.1 bandwidth))	≥93	[134]

Table 6.1: Femtosecond mid-IR and deep-IR single-stage OPOs. [a]Tuning methods: P: Pump tuning, A: Angle tuning, C: Cavity delay tuning, Q: QPM grating tuning. [b]Range defined relative to weighted centre of most extreme recorded spectra, not 10 dB limit. [c]Maximum idler power and power at selected wavelengths of interest.

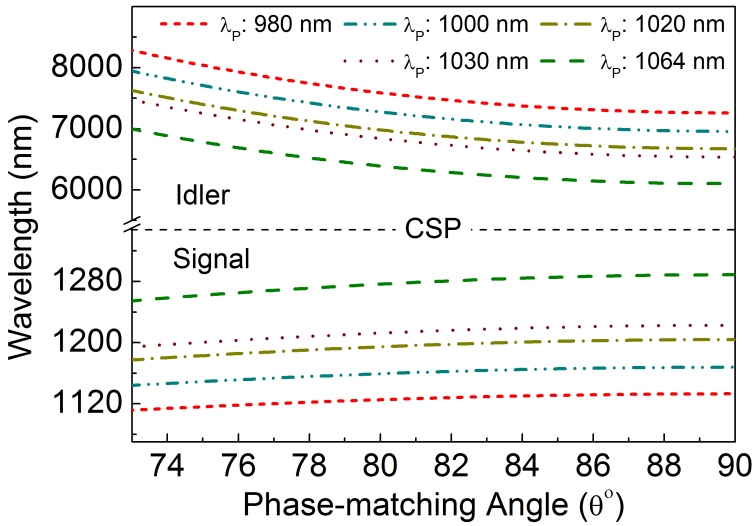

Figure 6.2: Signal and idler tuning curves for type-I ($e \rightarrow oo$) critical phase-matching as a function of the CSP internal angle for various pump wavelengths in the range so far used to pump CSP OPOs.

6.3 Experiment

6.3.1 Experimental setup

The configuration of the deep-IR CSP femtosecond OPO is depicted in Figure 6.3. The pump source is a KLM Ti:sapphire laser (Spectra-Physics *Mai Tai HP*), providing near transform-limited ultrashort pulses at a repetition rate of 80.5 MHz. To reduce any two-photon absorption, we operated the laser close to the upper limit of its tuning range (640–1040 nm), where the average output power is >700 mW, comfortably higher than the reported threshold in a CSP OPO pumped close to 1 μm [133]. Using a half-wave plate, we adjusted the polarisation to that required for type-I ($e \rightarrow oo$) phase-matching in the CSP crystal. The 1-mm-long crystal was cut at θ = 90° (ϕ = 45°) for noncritical phase-matching (NCPM) at normal incidence, and mounted on a precision rotation stage to enable angle tuning. A lens, L_1, of focal length, f = 100 mm, was used to focus the pump beam to a waist

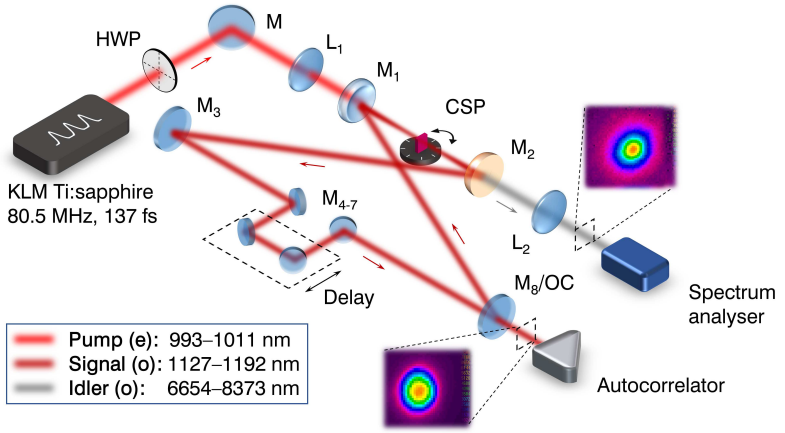

Figure 6.3: Schematic of the experimental setup for the Ti:sapphire-pumped CSP femtosecond OPO. HWP: Half wave plate, M: Mirrors, OC: Output coupler, L: Lenses.

radius of $w_0 \sim 28$ μm, ensuring optimal parametric interaction with the signal without the risk of crystal damage. The OPO cavity is configured in a ring comprising two planoconcave mirrors, M_{1-2} (r = 100 mm), and six plane mirrors, M_{3-8}, with M_{5-6} mounted on a translation stage, forming a delay line to allow precise control of synchronisation. All cavity mirrors were coated to ensure singly-resonant OPO operation for the near-IR signal, and efficient single-pass extraction of the deep-IR idler through M_2. Full details of optical coatings are summarised in Table 6.2. M_8 was alternatively used as a signal high-reflector to achieve maximum idler power, and a 5% output coupler was used to enable characterisation of the signal. A lens, L_2, collimates the idler for alignment into a spectrum analyser, while the output-coupled signal is directed to an intensity autocorrelator.

The characteristics of the KLM Ti:sapphire laser used in this experiment over the range 990–1015 nm are shown in Figure 6.4. Also shown are the smooth pump spectra and a sample interferometric autocorrelation recorded at 997 nm. The resultant de-convolved pulse duration is 137 fs, which we measured to be constant across the tuning range used

Optic	Substrate	High-reflection (nm)	Anti-reflection (nm)
L_1	NBK7	-	650–1050 (**>99%**)
L_2	CaF_2	-	6000–8500 (**>60%**)
M_1	CaF_2	1100–1300 (**>99%**)	990–1015 (**>70–83%**)
M_2	ZnSe	1100–1300 (**>97%**)	6500–9000 (**>94%**)
M_{3-7}	NBK7	1100–1300 (**>99.8%**)	-
M_8/OC	NBK7	1100–1300 (**>95%**)	-
Crystal	CSP		950–1080 (**>99%**) 1100–1200 (**>99%**) 7000–8500 (**>93%**)

Table 6.2: Optics and coatings.

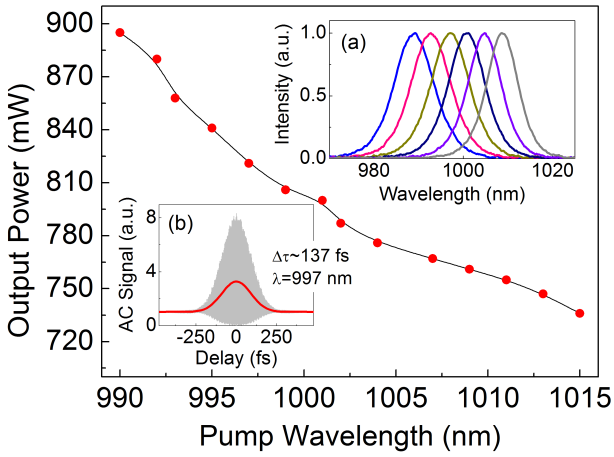

Figure 6.4: Ti:sapphire power across 990–1015 nm. Insets: (a) spectra across tuning range, (b) typical interferometric autocorrelation.

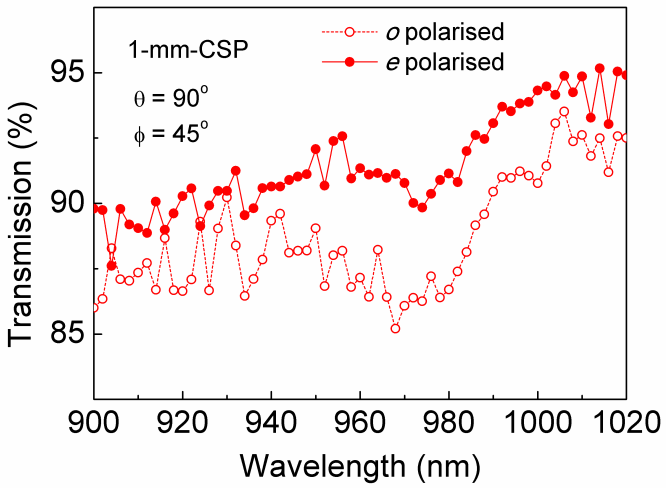

Figure 6.5: Transmission of the 1-mm-long CSP across 900–1020 nm for both *ordinary (o)* and *extraordinary (e)* polarisations.

in the experiment. The time-bandwidth product of $\Delta\nu\Delta\tau \sim 0.44$ is ∼1.4 times higher than the transform limit for $sech^2$ pulses, this slight chirp is thought to accumulate due to the distance of several metres between autocorrelator and laser aperture, with bounces from several unchirped mirrors. To determine the optimum wavelength for pumping the OPO, transmission measurements of the 1-mm-CSP crystal were performed by focusing the pump beam to a waist radius of $w_0 \sim 36$ μm, with an average power of 500–600 mW, corresponding to a peak intensity of 1.1–1.3 GW/cm^2. Using a power meter and spectrum analyser, we measured the transmitted power as a function of Ti:sapphire wavelength for both ordinary and extraordinary polarisations. The data was recorded over the range 900–1020 nm, with the results shown in Figure 6.5. A significant drop in transmission is noted below ∼993 nm, in agreement with previous literature which lists the short-wavelength edge as ∼1 μm [36]. The pump wavelength choice for the most efficient deep-IR performance is, therefore, a trade-off between absorption losses and pump power, both of

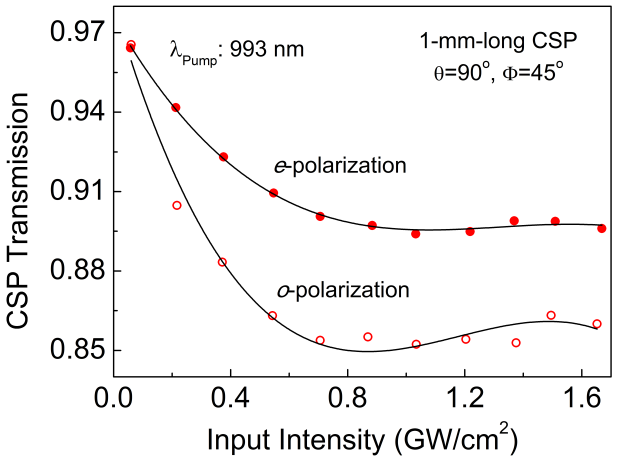

Figure 6.6: Transmission measurements of the 1-mm-long CSP crystal at 993 nm for both *ordinary (o)* and *extraordinary (e)* polarisations, at increasing intensities.

which increase towards shorter wavelengths.We found that although the crystal transmission remains ∼90% below 993 nm, the subsequent increase in pump power did not enable oscillation. The lower wavelength limit for OPO operation was thus 993 nm, while the upper limit was 1011 nm, beyond which the combination of lower pump power and coating losses in M_1 reduced the available power below threshold. Therefore, in this experiment, we were able to pump tune the OPO over 18 nm across 993–1011 nm.

6.3.2 Nonlinear absorption

CSP is known to exhibit detrimental two-photon absorption effects when pumped at high intensities near ∼1 μm [27, 131]. To assess the magnitude of these effects, we focused the beam to a waist radius of $w_0 \sim 37$ μm, and recorded the crystal transmission as the pump power was steadily The CSP transmission was recorded as a function of input intensity for both *ordinary (o)* and *extraordinary (e)* polarisations, with the results at the pump

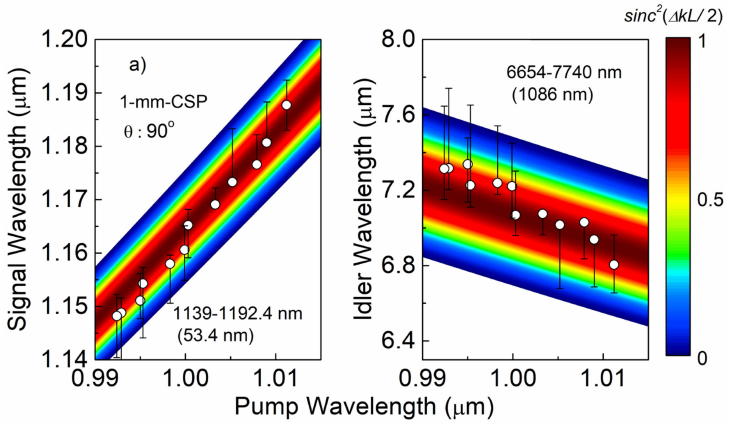

Figure 6.7: Pump tuning of the OPO across 993–1011 nm, superimposed on the parametric gain bandwidth for a 1-mm-long crystal.

wavelength of 993 nm shown in Figure 6.6. From the polynomial fit to the experimental data, it can be seen that for both polarisations the relationship becomes increasingly nonlinear at higher input intensities. Although the ratio of the CSP bandgap energy (2.45 eV) to the pump laser photon energy (1.25 eV) results in a value of ∼0.51, indicating major contribution from two-photon absorption, the experimental data show additional nonlinear effects, requiring confirmation through further investigation.

6.3.3 Device tuning

Operation of the OPO was achieved by assembling the cavity as shown in Figure 6.2, and synchronisation was obtained by fine adjustment of the delay line. We first performed characterisation by recording the output signal spectrum at different pump wavelengths across the available tuning range using a spectrum analyser. Figure 6.7 shows the experimental data for pump tuning superimposed on the parametric gain map, calculated using the Sellmeier equations reported in [36]. For each pump wavelength we set the OPO to perfect synchronisation by maximising the output power with minute adjustments to the cavity length, and recorded the

corresponding signal wavelength. In addition, spectra were recorded at the extremes of cavity length detuning, at the positions where oscillation ceased. Since the spectra in each case were highly asymmetric, the central wavelength was determined using a centre-of-mass averaging algorithm. White dots in Figure 6.7 represent the positions at which the highest output power was observed, while the vertical error bars show the extent of additional cavity delay tuning. The data points for the corresponding idler were calculated using energy conservation. We were able to achieve rapid tuning over 1139–1192.4 nm in the signal, and across 6654–7740 nm in the idler, using this method. There is generally good agreement between the phase-matching bandwidth and the available cavity delay tuning, however, additional factors that influence the maximum detuning range include cavity dispersion, circulating power, and beam misalignment. In order to generate the longest idler wavelengths, type-I critical phase-matching was employed in the form of crystal rotation from θ = 90° to 74°. For each phase-matching angle, the signal spectrum at perfect synchronisation was recorded, and the corresponding deep-IR idler was calculated from the centre wavelength using energy conservation. The results are shown in Figure 6.8, where it can be seen that the near-IR signal wavelength could be tuned across 1126.7–1153.8 nm, with the idler covering a spectral range of 6923–8373 nm in the deep-IR, for two pump wavelengths at 993 nm and 1000 nm. The measured values are also compared to the Sellmeier predictions, with the observed offset accredited to strong self-phase modulation (SPM) redistributing the spectral density towards shorter wavelengths. It is expected that introducing dispersion control in the form of intracavity prisms or the use of optimised chirped mirrors for the OPO will reduce the discrepancy between the experimental tuning data and the calculations.

As seen in Figures 6.7 and 6.8, the relatively wide parametric gain bandwidth of CSP enables wavelength tuning by variation of cavity length. This is a convenient method for rapid tuning across a large idler bandwidth. An example of cavity delay tuning from this OPO at a pump wavelength of 993 nm and phase-matching angle of 90° is shown in Figure 6.9.

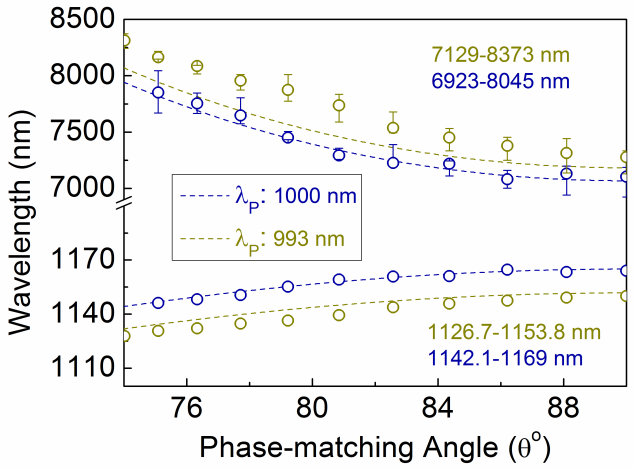

Figure 6.8: Idler and signal tuning as a function of the internal phase-matching angle in the CSP crystal, for pump wavelengths of 993 nm and 1000 nm, compared to the wavelength tuning curves predicted using the Sellmeier equations in [36]. Error bars represent additional cavity delay tuning.

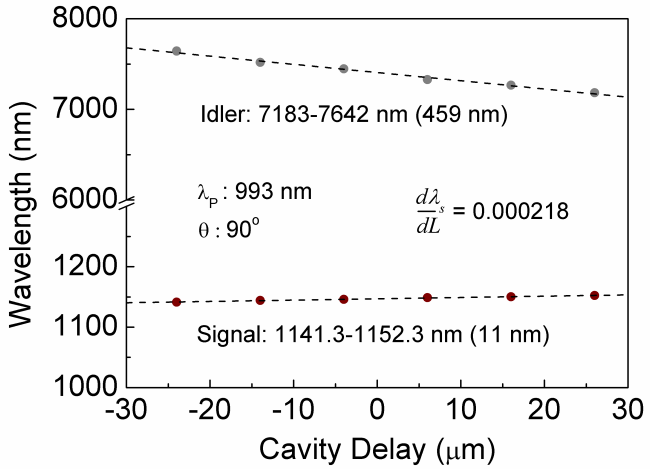

Figure 6.9: Cavity delay tuning at normal incidence for a pump wavelength of 993 nm.

For a singly-resonant OPO, the rate of change of signal wavelength can be used to acquire an estimate for the total cavity group delay dispersion (GDD), using the relation

$$GDD = \beta_2 L = \frac{\lambda_s^2}{2\pi c^2}\left(\frac{d\lambda_s}{dL}\right)^{-1} \tag{6.1}$$

where β_2 is average cavity GVD, L is the total cavity length, λ_s is the signal wavelength, c is the velocity of light, and $d\lambda_s/dL$ is the gradient from Figure 6.9. Evaluating equation (6.1) for the experimentally measured value of $d\lambda_s/dL$ = 0.000218 yields an estimated total GDD of ∼10700 fs^2. This value is much greater than the expected contribution from the 1-mm-long CSP crystal, which at 1.15 μm is calculated to be ∼646 fs^2, indicating that other cavity elements, such as the uncompensated mirrors, M_1, M_2 and M_8, contribute significantly to the total GDD value. Further investigation is required to determine the dominant cause of dispersion.

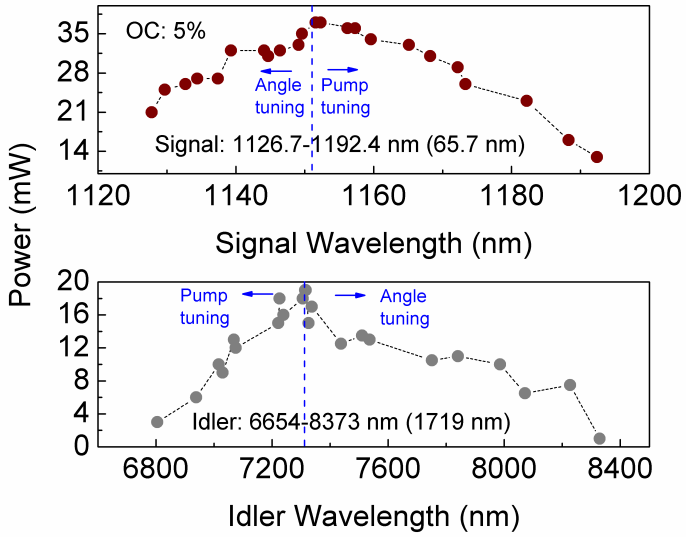

Figure 6.10: Signal and idler average powers measured across the total tuning range, using a 5% output coupler to extract the signal.

6.3.4 Output power

The signal and idler output powers across the tuning range of the CSP femtosecond OPO are displayed in Figure 6.10. Data points below ~7300 nm were acquired using pump tuning with a pump power varying from 430 mW at 1011 nm to 690 mW at 993 nm, after transmission through M_1, while those above were acquired using angle tuning at 993 nm for a fixed pump power of 690 mW. We extracted deep-IR idler average powers of >10 mW across >65% of the tuning range, with a maximum of 20 mW at 7314 nm and >6 mW available up to 8227 nm. This is equivalent to a peak idler quantum conversion efficiency of 21.3%. Furthermore, with a 5% output coupler in place, we measured signal powers up to 37 mW at 1152 nm. The drop-off in power towards long idler wavelengths is primarily due to Fresnel losses at large crystal rotation angles, while at lower wavelengths it is caused by a reduction in available pump power. It is

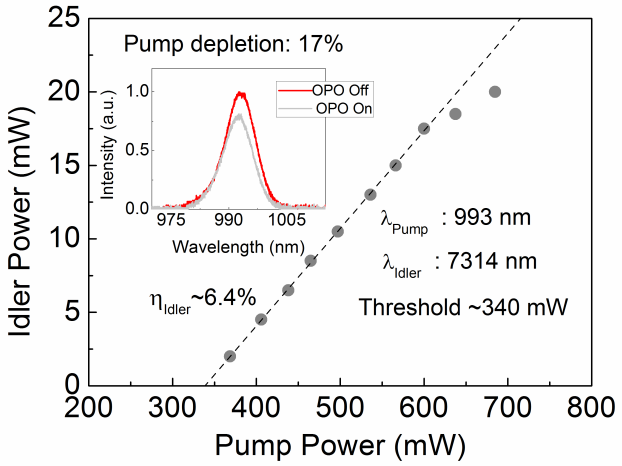

Figure 6.11: Power scaling of the idler extracted from the CSP femtosecond OPO. Inset: Input pump spectrum and depleted pump spectrum while the OPO is operating at maximum power.

noted that data here is not corrected for losses in the crystal, mirrors M_2 and M_8, filters F_{1-2}, and a ∼40% transmission loss through L_2. We investigated idler power scaling of the OPO, using a high reflector in place of M_8 to maximise the deep-IR power, with the results shown in Figure 6.11. The pump power is corrected for a ∼83% transmission loss through M. At a pump wavelength of 993 nm, the OPO threshold was measured to be ∼340 mW, and the idler slope efficiency is ∼6.4%, with a pump depletion of ∼17%. As the threshold is higher than the theoretically calculated value (see [56] for method), it is clear that absorption processes in the crystal, including two-photon absorption, play a role in increasing the cavity losses. The passive power stability of signal and idler is shown in Figure 6.12. At an idler wavelength of 7571 nm, the stability is estimated to be 3.2% rms over 1 hour, while the corresponding signal at 1143 nm exhibits a stability of 2.2% rms over the same period.

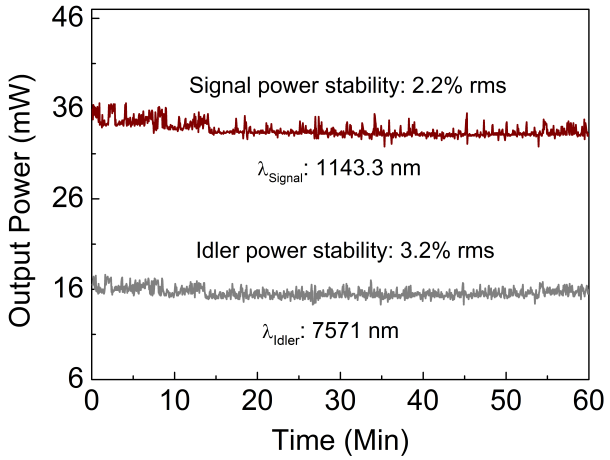

Figure 6.12: Passive power stability of signal and idler at 1143.3 nm and 7571 nm, respectively, measured over 1 hour.

6.3.5 Spectrum and pulse durations

Figure 6.13 shows the spatial beam profiles of the signal and idler output from the OPO, recorded using a pyroelectric camera. As can be seen, both beams exhibit high spatial quality with single-peak TEM_{00} Gaussian distribution.

We characterised the detailed spectral quality of the signal and idler using two spectrum analysers for the near-IR and deep-IR with resolutions of 0.7 nm and ∼4 nm, respectively. The signal spectra were found to be highly asymmetric, containing an SPM-induced long-wavelength tail, as expected for a cavity with a large net positive GVD. In contrast, idler spectra were measured to be almost symmetric with evidence of atmospheric water absorption at shorter wavelengths in the form of deep modulations. In order to compare the relative brilliance of the OPO to other deep-IR sources, we calculated the spectral brightness as defined in [137], using data from Figure 6.10 and Figure 6.14, for an idler with waist radius w_{0i} = 18.0 μm and average power of 20 mW at 7314 nm. The calculation yields a value of 6.68×10^{20} photons s^{-1} mm^{-2} sr^{-1} 0.1% BW^{-1}, comparable to

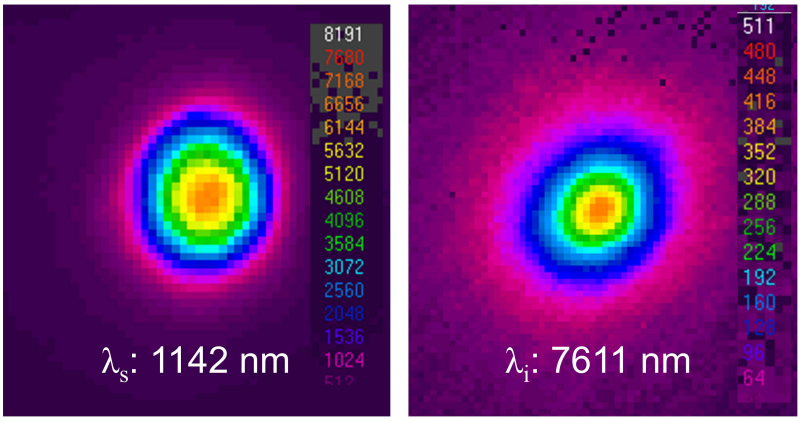

Figure 6.13: Spatial beam profiles of the idler and signal at 7611 nm and 1142 nm, respectively.

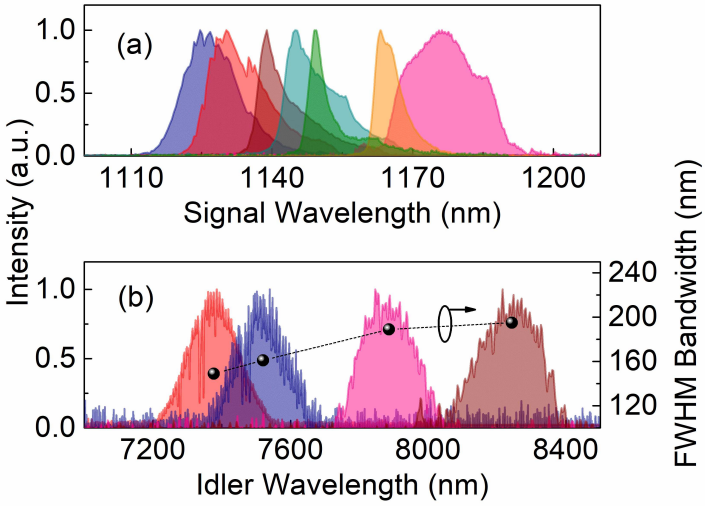

Figure 6.14: Signal and idler spectra, with idler FWHM bandwidths across the tuning range of the OPO.

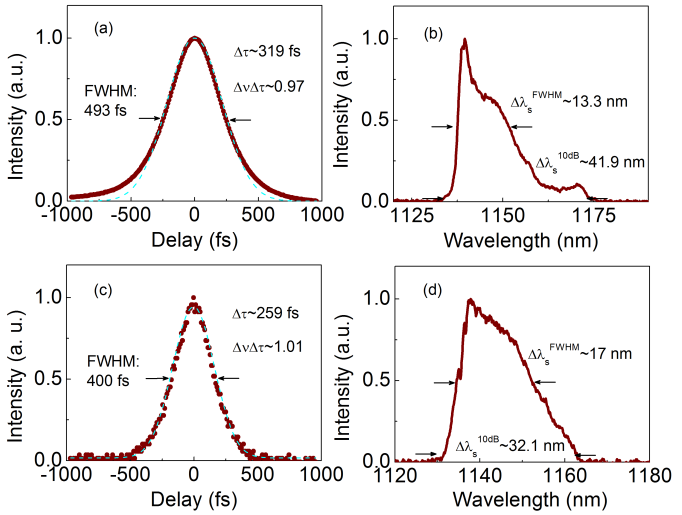

Figure 6.15: Signal intensity autocorrelation at (a) perfect cavity synchronisation, with (b) corresponding spectrum. (c) Signal intensity autocorrelation with the cavity detuned, with (d) corresponding spectrum.

the record value from a mid-IR centred supercontinuum, and 2 orders of magnitude greater than a typical synchrotron facility [138, 139]. The pulse duration was measured experimentally using an intensity autocorrelator, confirming strongly chirped pulses.

Figure 6.15 shows signal autocorrelation profiles and corresponding spectra at perfect synchronisation, (a) and (b), and when the cavity is slightly negatively detuned, (c) and (d). The autocorrelation measurements confirm durations of 319 and 259 fs, respectively, with corresponding spectra having approximate 10 dB bandwidths of 41.9 nm and 32.1 nm. When the signal and pump pulses are not perfectly temporally overlapped, the reduced intracavity power induces a smaller nonlinear phase shift and results in a weaker pulse chirp. Therefore, since a strongly chirped pulse broadens rapidly under the influence of GVD, a shorter measured pulse duration away from synchronisation is consistent with intuition. This is also reflected in the respective corresponding spectra, of which the measurement at perfect synchronisation shows a wider 10 dB band-

width, indicating stronger SPM effects. The results of Figure 6.15(c) are compared to those predicted using a simple theoretical model of a signal pulse propagating in the presence of GVD, with higher order dispersion and nonlinear effects neglected. In this case, the final pulse envelope is given by

$$E(z,t) = \frac{1}{2\pi}\int_{-\infty}^{\infty} E(0,\omega) exp\left(\frac{i\omega^2 GDD}{2} - i\omega t\right) d\omega \qquad (6.2)$$

where $E(0,\omega)$ is the Fourier transform of the initial pulse envelope $E(0,t)$, which is assumed to have an intensity distribution of the form $P(0,t) \equiv |E(0,t)|^2 = P_{peak} sech^2(t/\tau_0)$, where τ_0 is related to the pulse FWHM by $\tau_0 = \Delta\tau/1.763$. If the initial signal pulse duration is set equal to that of the pump ($\Delta\tau_p \sim 137$ fs), evaluating equation (6.2) gives a final signal pulse duration of $\Delta\tau_s \sim 263$ fs, in strong agreement with the experimental observations in Figure 6.15(c). A more realistic model could be obtained by applying the nonlinear Schrödinger equation (NLSE) to the circulating signal pulses. The general NLSE considers multiple-order dispersion, SPM, intrapulse Raman scattering, and self-steepening of the temporal profile [61]. However, in order to calculate the magnitude of the nonlinear effects, knowledge of the Kerr refractive index, n_2, of CSP is required, which, to the best of our knowledge, has not yet been determined. It is expected that including this term in our calculations would bring the predicted final pulse width closer to the experimentally measured value. Alternatively, deploying suitable intracavity dispersion compensation in the form of chirped mirrors, or a four prism compressor, would bring the time-bandwidth product closer to the transform limit.

6.4 Conclusions

In conclusion, we have demonstrated a high-spectral brilliance, high-repetition-rate femtosecond source of coherent radiation for the deep-IR using a single frequency conversion stage pumped by a KLM Ti:sapphire laser. By exploiting the wide transparency window of CSP, we have been able to

achieve successful operation of a deep-IR femtosecond OPO directly using a KLM Ti:sapphire laser, for the first time. In doing so, we have produced up to 20 mW of average power at 7314 nm, equivalent to a spectral brightness of 6.68×10^{20} photons s^{-1} mm^{-2} sr^{-1} 0.1% BW^{-1}, with up to 37 mW generated in the near-IR signal. We have used three separate tuning methods; type-I critical phase-matching, pump wavelength tuning, and cavity delay tuning, to generate coherent radiation across 1127–1192 nm and 6654–8373 nm (1194–1503 cm^{-1}) in the signal and idler, respectively, with typical FWHM spectral bandwidths of 140–180 nm in the deep-IR. In particular, exploiting the tunable properties of the Ti:sapphire laser has permitted rapid tuning of the deep-IR idler wavelength over key spectral regions, including the amide III band, of great interest for medical imaging. The signal and idler beams exhibit excellent TEM_{00} spatial quality and passive long-term power stability of 2.2% and 3.2% rms over 1 hour, respectively. Spectral and temporal characterisation of the signal has revealed chirped pulses with a time-bandwidth product, $\Delta\nu\Delta\tau \sim 1$. Both the pulse durations and 10 dB spectral bandwidths were observed to be broader at higher intracavity powers, indicating strong intracavity self-phase modulation, which could be reduced using appropriate intracavity dispersion management. With high average power at a high repetition rate, this OPO represents an attractive source for low-noise spectroscopy, frequency comb generation and medical diagnostics in the 6.5–8.5 μm spectral region, using a simplified pumping method based on established ultrafast KLM Ti:sapphire laser technology.

7 Summary and outlook

In this thesis, we have demonstrated novel femtosecond OPOs in the infrared, covering a total spectral range of 1–8.4 μm. All devices are widely tunable, singly-resonant oscillators (SROs) pumped using KLM Ti:sapphire laser technology at 0.8–1.08 μm.

1. First we developed a compact, rapidly tunable near-IR OPO based on MgO:PPLN, which, to the best of our knowledge, is the first tunable fibre-feedback device producing sub-100 fs pulses. Furthermore, in a previously unreported mechanism, it generates transform-limited pulses by soliton formation in the optical fibre. Detailed simulations were performed using a numerial model based on nonlinear pulse propagation, yielding excellent agreement with experimental data. Output powers up to 110 mW (pump power 1.3 W) were measured, with passive power and wavelength fluctuations of 0.26% and 0.014% rms, respectively.

2. Secondly, we exploited group-velocity matching in MgO:PPLN to build a synchronously-pumped OPO based on a 42-mm-long crystal. The long nonlinear interaction length led to 78% pump depletion, and a quantum conversion efficiency of 48% from the near- to mid-IR. With a threshold of only 5 mW, and high passive stability, this device is ideal for spectroscopic applications, which we explored by performing broadband transmission spectroscopy of methane.

3. Finally, we deomnstrated an OPO based on the new nonlinear material $CdSiP_2$ (CSP), producing about 20 mW of average power in the deep-mid IR across 6.6–8.4 μm, equivalent to a peak power of 1 kW (~300 fs pulses). Idler FWHM bandwidths were measured to be 160–200 nm across the tuning range. This source exceeds the spectral brightness offered by supercontinuum and synchrotron sources across the equivalent wavelength regions.

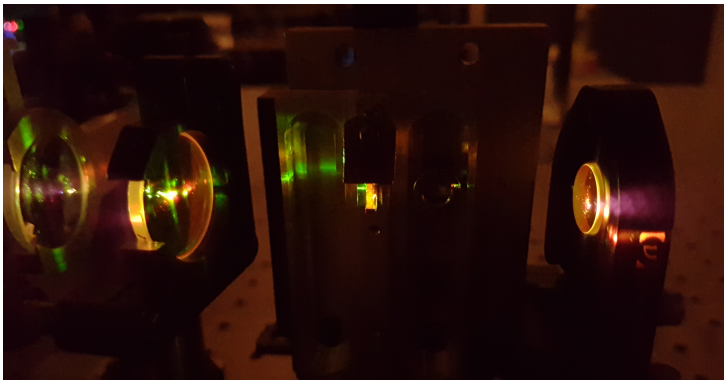

Figure 7.1: Photo of synchronously-pumped OP-GaP OPO operating with idler ~7 μm. Visible light is non-phase-matched SHG of the resonant signal at ~1.2 μm.

7.1 Future directions

Further to the work presented in this thesis, we have also investigated the recently developed semiconductor crystal, orientation-patterned GaP (OP-GaP), for frequency conversion from ~1 mm sources to the mid and deep mid-IR. A synchronously-pumped OPO was successfully realised (see photo in Figure 7.1) by pumping three 1-mm-long OP-GaP crystals containing QPM grating periods of 18 μm, 21.5 μm, and 24.5 μm, with the same tunable femtosecond laser described in chapter 5. Preliminary results suggest idler wavelength tuning across ~3.5–8 μm, confirming that the favourable dispersion and transmission properties of OP-GaP make it an excellent choice for broadly tunable infrared generation. The oscillation threshold was measured to be ~300 mW at a pump wavelength of 1.03 μm, suggesting that the OPO could also be pumped directly with the KLM Ti:sapphire laser, as demonstrated with CSP in chapter 6.

In addtion, OP-GaP has the potential to be deployed in a group-velocity matched OPO, analagous to the device presented in chapter 5. Pump/idler group-velocity matching could be achieved if a crystal with grating period of Λ = 86 μm is pumped at 1.95 μm (Thulium fibre emission wavelength), which could yield efficient generation at 10.3 μm through the use of a long

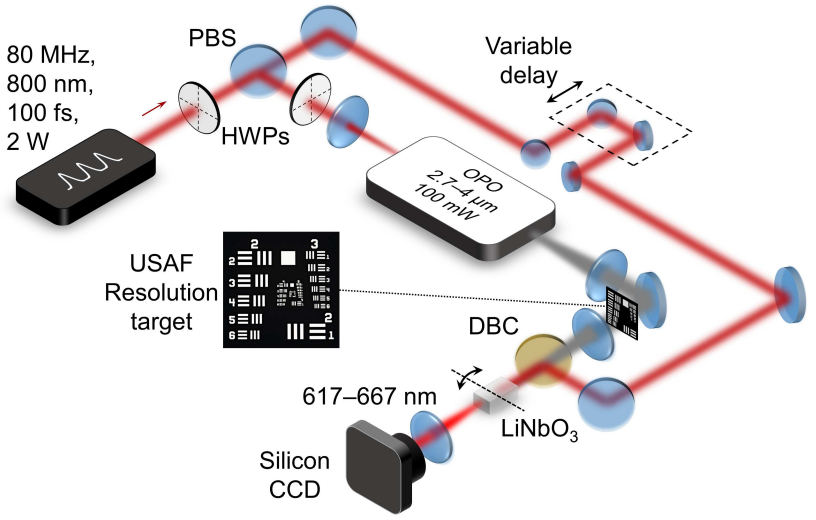

Figure 7.2: Experimental setup used for mid-IR femtosecond synchronous upconversion imaging. PBS: Polarising beam splitter, HWPs: Half-wave plates, DBC: Dichroic beam combiner.

crystal. Alternative crystals with deeper IR transparency include $AgGaSe_2$ (AGSE), and the newly developed $BaGa_4Se_7$ (BGSE) and $BaGa_2GeSe_6$ (BGGSE), the latter two of which can extend tuning to ~20 μm with the correct choice of phase-matching angle.

The sub-100 fs fibre-feedback OPO presented in chapter 4 has potential for a great variety of applications, ranging from practical use as a stable source for spectroscopy and microscopy, to deeper theoretical investigations of nonlinear solitonic pulse dynamics. Work is currently underway to transfer this technology to the picosecond timescale, and also to develop robust, stable sources for imaging applications. The spectral region across 6–8 μm is especially attractive for medical purposes, as the strong absorption of biological tissue in this region can be exploited to perform hyperspectral imaging of cancerous tumors.

In a parallel study to the work presented here, an imaging technique based on upconversion of mid-IR light to visible wavelengths, was inves-

tigated. This enables low-noise, room temperature silicon cameras operating in the visible and near-IR to be used to perform gas analysis and medical diagnostics in the mid-IR. The mid-IR light was provided by the idler from a femtosecond OPO, as shown in Figure 7.2, where sum-frequency-generation was performed with a portion of the fundamental pump beam, in a bulk $LiNbO_3$ crystal, to produce visible light across 617–667 nm. The results, presented in an upcoming publication, show that using this setup we were able to successfully resolve the smallest element (70 μm) of a US Air Force resolution target.

Bibliography

[1] http://laserfest.org/lasers/pioneers/nobel.cfm

[2] T. H. Maiman, Stimulated optical emission in ruby, Nature 187, 493–494 (1960).

[3] https://www.laserfocusworld.com/articles/print/volume-54/issue-01/features/annual-laser-market-review-forecast-lasers-enabling-lasers.html

[4] https://www.statista.com/statistics/289212/sales-of-lasersworldwide-by-application/

[5] K. König, Multiphoton microscopy in life sciences, Journal of microscopy, 200, 83–104 (2000).

[6] A. Schliesser, N. Picqué, and T. W. Hänsch, Mid-infrared frequency combs, Nat. Photon. 6, 440 (2012).

[7] R. C. Gray, The Rev. John Kerr, F.R.S., Inventor of the Kerr Cell, Nature 136, 245–247 (1935).

[8] C. V. Raman and K. S. Krishnan, A new type of secondary radiation, Nature 121, 501–502 (1928).

[9] E. Schrödinger, Nonlinear optics, Proc. Royal Irish Academy 47 A, 77–117 (1942).

[10] P. A. Franken, A. E. Hill, C. W. Peters, and G. Weinreich, Generation of optical harmonics, Phys. Rev. Lett. 7, 118–119 (1961).

[11] J. A. Armstrong, N. Bloembergen, J. Ducuing, and P. S. Pershan, Interaction between light waves in a nonlinear dielectric, Phys. Rev. 127, 1918–1939 (1962).

[12] J. A. Giordmaine, Mixing of light beams in crystals, Phys. Rev. Lett. 8, 19–20 (1962).

[13] A. W. Smith and N. Braslau, Observation of an optical difference frequency, J. Appl. Phys. 34, 2105–2106 (1963).

[14] J. A. Giordmaine and R. C. Miller, Tunable coherent parametric oscillation in $LiNbO_3$ at optical frequencies, Phys. Rev. Lett. 14, 973–976 (1965).

[15] R. L. Byer, M. K. Oshman, J. F. Young, and S. E. Harris, Visible cw parametric oscillator, Appl. Phys. Lett. 13, 109–111 (1968).

[16] T. Kushida, Y. Tanaka, and M. Ojima, Tunable picosecond pulse generation by optical parametric oscillator, Jap. J. Appl. Phys, 16, 2227 (1977).

[17] R. L. Fork, B. I. Greene, and C. V. Shank, Generation of optical pulses shorter than 0.1 psec by colliding pulse mode locking, Appl. Phys. Lett. 38, 671–672 (1981).

[18] D. E. Spence, P. N. Kean, and W. Sibbett, 60-fsec pulse generation from a self-mode-locked Ti:sapphire laser, Opt. Lett. 16, 42–44 (1991).

[19] D. C. Edelstein, E. S. Wachman, and C. L. Tang, Broadly tunable high repetition rate femtosecond optical parametric oscillator, Appl. Phys. Lett. 54, 1728–1730 (1989).

[20] S. Matsumoto, E. J. Lim, H. M. Hertz, and M. M. Fejer, Quasi phase-matched second harmonic generation of blue light in electrically periodically-poled lithium tantalate waveguides, Electron. Lett. 27, 2040–2042 (1991).

[21] Q. Fu, G. Mak, and H. M. Van Driel, High-power, 62-fs infrared optical parametric oscillator synchronously pumped by a 76-MHz Ti:sapphire laser, Opt. Lett. 17, 1006–1008 (1992).

[22] J. M. Dudley, D. T. Reid, M. Ebrahim-Zadeh, and W. Sibbett, Characteristics of a noncritically phase-matched Ti:sapphire pumped fem-

tosecond optical parametric oscillator. Opt. Commun. 104, 419–430 (1994).

[23] K. C. Burr, C. L. Tang, M. A. Arbore, and M. M. Fejer, Broadly tunable mid-infrared femtosecond optical parametric oscillator using all-solid-state-pumped periodically poled lithium niobate, Opt. Lett 22, 1458–1460 (1997).

[24] M. Ghotbi, A. Esteban-Martin, and M. Ebrahim-Zadeh, BiB_3O_6 femtosecond optical parametric oscillator, Opt. Lett. 31, 3128–3130 (2006).

[25] M. Ghotbi, A. Esteban-Martin, and M. Ebrahim-Zadeh, Tunable, high repetition-rate, femtosecond pulse generation in the ultraviolet, Opt. Lett. 33, 345–347 (2008).

[26] S. Marzenell, R. Beigang, and R. Wallenstein, Synchronously pumped femtosecond optical parametric oscillator based on $AgGaSe_2$ tunable from 2 μm to 8 μm, Appl. Phys. B 69, 423–428 (1999).

[27] S. Chaitanya Kumar, J. Krauth, A. Steinmann, K. T. Zawilski, P. G. Schunemann, H. Giessen, and M. Ebrahim-Zadeh, (2015). High-power femtosecond mid-infrared optical parametric oscillator at 7 μm based on $CdSiP_2$, Opt. Lett. 40, 1398–1401 (2015).

[28] L. Maidment, P. G. Schunemann, and D. T. Reid, Molecular fingerprint-region spectroscopy from 5 to 12 μm using an orientation-patterned gallium phosphide optical parametric oscillator, Opt. Lett. 41, 4261–4264 (2016).

[29] T. Steinle, F. Mörz, A. Steinmann, and H. Giessen, Ultra-stable high average power femtosecond laser system tunable from 1.33 to 20 μm, Opt. Lett. 41, 4863–4866 (2016).

[30] J. H. Sun, B. J. S. Gale, and D. T. Reid, Composite frequency comb spanning 0.4-2.4 μm from a phase-controlled femtosecond

Ti:sapphire laser and synchronously pumped optical parametric oscillator, Opt. Lett. 32, 1414–1416 (2007).

[31] A. Marandi, Z. Wang, K. Takata, R. L. Byer, and Y. Yamamoto, Network of time-multiplexed optical parametric oscillators as a coherent Ising machine, Nat. Photon. 8, 937 (2014).

[32] Q. Ru, N. Lee, X. Chen, K. Zhong, G. Tsoy, M. Mirov, S. Vasilyev, S. B. Mirov, and K. L. Vodopyanov, Optical parametric oscillation in a random polycrystalline medium, Optica 4, 617–618 (2017).

[33] M. Ebrahim-Zadeh and I. T. Sorokina, Mid-Infrared coherent sources and applications, 1st ed. (Springer, 2007).

[34] Radiantis, Inspire (http://www.radiantis.com/inspire-hf.html).

[35] D. N. Nikogosyan, Nonlinear Optical Crystals: A Complete Survey, Springer, New York, 2005.

[36] K. T. Zawilski, P. G. Schunemann, C. T. Pollak, D. E. Zelmon, N. C. Fernelius, and F. K. Hopkins, Growth and characterization of large $CdSiP_2$ single crystals, J. Cryst. Growth 312, 1127 (2010).

[37] P. G. Schunemann, K. T. Zawilski, L. A. Pomeranz, D. J. Creeden, and P. A. Budni, (2016). Advances in nonlinear optical crystals for mid-infrared coherent sources. J. Opt. Soc. Am. B 33, D36–D43 (2016).

[38] D. S. Chemla, Nonlinear optical properties of organic molecules and crystals (Vol. 1). Elsevier (2012).

[39] N. Bloembergen, Nonlinear optics, World Scientific (1996).

[40] P. A. Franken, and J. F. Ward, Optical harmonics and nonlinear phenomena, Rev. Mod. Phys. 35, 23 (1963).

[41] R. W. Boyd, Nonlinear Optics, Academic Press, San Diego, USA (2007).

[42] M. Ebrahim-Zadeh and M. H. Dunn, Optical parametric oscillators, Handbook of optics, 2nd ed. (Optical Society of America, Washington, D.C.), Chapter. 22 (2000).

[43] R. L. Sutherland, Handbook of nonlinear optics, second edition, Marcel Dekker, Inc., (1996).

[44] R.W. Munn and C. N. Ironside, Principles and Applications of Nonlinear Optical Materials, CRC Press (1993).

[45] D. A. Kleinman, Nonlinear dielectric polarization in optical media, Physical Review, 126, (1962).

[46] F. Zernike and J. E. Midwinter, Applied nonlinear optics, Wiley (1973).

[47] J. A. Armstrong, N. Bloemberger, J. Ducuing and P.S. Pershan, Interactions between light waves in a nonlinear dielectric, Phys Rev. 127, 1918–1939 (1962).

[48] M. M. Fejer, G. A. Magel, D. H. Jundt, and R. L. Byer, Quasi-phasematched second harmonic generation: Tuning and tolerances, IEEE J. Quantum Elect. 28, 2631–2654 (1992).

[49] S. Brosnan, and R. L. Byer, Optical parametric oscillator threshold and linewidth studies, IEEE J. Quantum. Electr. 15, 415–431 (1979).

[50] O. H. Heckl, B. J. Bjork, G. Winkler, P. B. Changala, B. Spaun, G. Porat, T. Q. Bui, K. F. Lee, J. Jiang, M. E. Fermann, and P. G. Schunemann, Three-photon absorption in optical parametric oscillators based on OP-GaAs, Opt. Lett. 41, 5405–5408 (2016).

[51] R. Smith, A study of factors affecting the performance of continuously pumped doubly resonant optical parametric oscillator, IEEE J. Quantum Electr. 9, 530–540 (1973).

[52] L. E. Myers, R. C. Eckardt, M. M. Fejer, R. L. Byer, W. R. Bosenberg, and J. W. Pierce, Quasi-phase-matched optical parametric oscillators

in bulk periodically poled $LiNbO_3$, J. Opt. Soc. Am. B 12, 2102–2116 (1995).

[53] R. L. Byer, Parametric oscillators and nonlinear materials, in Nonlinear Optics, P. G. Harper and B. S. Wherrett, eds., Academic Press, New York (1977).

[54] G. D. Boyd and D. A. Kleinman, Parametric interaction of focused Gaussian light beams, J. Appl. Phys. 39, 3597–3639 (1968).

[55] S. Guha, Focusing dependence of the efficiency of a singly resonant optical parametric oscillator, Appl. Phys. B 66, 663–675 (1998).

[56] M. J. McCarthy and D. C. Hanna, All-solid-state synchronously pumped optical parametric oscillator, J. Opt. Soc. Am. B 10, 2180 (1993).

[57] D. C. Hanna, M. V. O'Connor, M. A. Watson, and D. P. Shepherd, Synchronously pumped optical parametric oscillator with diffraction-grating tuning, J. Phys. D 34, 2440–2454 (2001).

[58] P. E. Powers, T. J. Kulp, and S. E. Bisson, Continuous tuning of a continuous-wave periodically poled lithium niobate optical parametric oscillator by use of a fan-out grating design, Opt. Lett. 23, 159–161 (1998).

[59] W. Ruderman, J. Maffetone, D. E. Zelman, and D. M. Poirier, Laser damage studies of silver gallium sulfide single crystals, MRS Online Proceedings Library Archive, 484 (1997).

[60] D. A. Bryan, R. Gerson, and H. E. Tomaschke, Increased optical damage resistance in lithium niobate, Appl. Phys. Lett. 44, 847–849 (1984).

[61] G.P. Agrawal, Nonlinear Fiber Optics, 4th edition, Academic Press, New York, (2007).

[62] J. C. Diels and W. Rudolph, Ultrashort laser pulse phenomena, 2nd edition, Academic Press, 2nd ed.

[63] A. V. Smith, R. J. Gehr, and M. S. Bowers, Numerical models of broad-bandwidth nanosecond optical parametric oscillators, J. Opt. Soc. Am. B 16, 609–619 (1999).

[64] M. Conforti, F. Baronio, and C. De Angelis, Nonlinear envelope equation for broadband optical pulses in quadratic media, Phys. Rev. A, 81, 053841 (2010).

[65] D. T. Reid, Ultra-broadband pulse evolution in optical parametric oscillators. Opt. Express 19, 17979–17984 (2011).

[66] P. S. Jian, W. E. Torruellas, M. Haelterman, S. Trillo, U. Peschel, and F. Lederer, Solitons of singly resonant optical parametric oscillators, Opt. Lett 24, 400–402 (1999).

[67] R. L. Fork, O. E. Martinez, and J. P. Gordon, Negative dispersion using pairs of prisms, Opt. Lett. 9, 150–152 (1984).

[68] J. T. Verdeyen, Lasers Electronics, Third Ed., Prentice Hall, Englewood Cliffs, New Jersey (1995).

[69] A. E. Siegman, Lasers, University Science Books (1986).

[70] M. H. Dunn and M. Ebrahim-Zadeh, Parametric generation of tunable light from continuous-wave to femtosecond pulses, Science 286, 1513–1517 (1999).

[71] I. Rocha-Mendoza, W. Langbein, P. Watson, and P. Borri, Differential coherent anti-Stokes Raman scattering microscopy with linearly chirped femtosecond laser pulses, Opt. Lett. 34, 2258–2260 (2009).

[72] V. Andresen, S. Alexander, W. M. Heupel, M. Hirschberg, R. M. Hoffman, and P. Friedl, Infrared multiphoton microscopy: subcellular-resolved deep tissue imaging, Curr. Opin. Biotech. 20, 54–62 (2009).

[73] J. Herz, V. Siffrin, A. E. Hauser, A. U. Brandt, T. Leuenberger, H. Radbruch, F. Zipp, and R. A. Niesner, Expanding two-photon intravital microscopy to the infrared by means of optical parametric oscillator, Biophys. J. 98, 715–723 (2010).

[74] M. Ebrahim-Zadeh, Efficient ultrafast frequency conversion sources for the visible and ultraviolet based on BiB_3O_6, IEEE J. Sel. Top. Quantum Electron. 13, 679–691 (2007).

[75] S. Chaitanya Kumar, P. G. Schunemann, K. T. Zawilski, and M. Ebrahim-Zadeh, Advances in ultrafast optical parametric sources for the mid-infrared based on $CdSiP_2$, J. Opt. Soc. Am. B 33, D44–D56 (2016).

[76] Y. Kobayashi, K. Torizuka, A. Marandi, R. L. Byer, R. A. McCracken, Z. Zhang, and D. T. Reid, Femtosecond optical parametric oscillator frequency combs, J. Optics 17, 094010 (2015).

[77] I. Coddington, N. Newbury, and W. Swann, Dual-comb spectroscopy, Optica 3, 414–426 (2016).

[78] Y. Jin, S. M. Cristescu, F. J. M. Harren, and J. Mandon, Femtosecond optical parametric oscillators toward real-time dual-comb spectroscopy, Appl. Phys. B 119, 65–74 (2015).

[79] P. L. McMahon, A. Marandi, Y. Haribara, R. Hamerly, C. Langrock, S. Tamate, T. Inagaki, H. Takesue, S. Utsunomiya, K. Aihara, and R. L. Byer, A fully programmable 100-spin coherent Ising machine with all-to-all connections, Science 354, 614–617 (2016).

[80] R. Hamerly, A. Marandi, M. Jankowski, M. M. Fejer, Y. Yamamoto, and H. Mabuchi, Reduced models and design principles for half-harmonic generation in synchronously pumped optical parametric oscillators, Phys. Rev. A 94, 063809 (2016).

[81] M. Jankowski, A. Marandi, C. R. Phillips, R. Hamerly, K. A. Ingold, R. L. Byer, and M. M. Fejer, Temporal simultons in optical parametric oscillators, Phys. Rev. Lett. 120, 053904 (2018).

[82] C. Xu, and F. W. Wise, Recent advances in fibre lasers for nonlinear microscopy, Nat. Photonics 7, 875 (2013).

[83] C. F. Kaminski, R. S. Watt, A. D. Elder, J. H. Frank, and J. Hult, Supercontinuum radiation for applications in chemical sensing and microscopy, Appl. Phys. B 92, 367 (2008).

[84] S. Lefrancois, D. Fu, G. R. Holtom, L. Kong, W. J. Wadsworth, P. Schneider, R. Herda, A. Zach, X. Sunney Xie, and F. W. Wise, Fiber four-wave mixing source for coherent anti-Stokes Raman scattering microscopy, Opt. Lett. 37, 1652–1654 (2012).

[85] F. M. Mitschke, and L. F. Mollenauer, Discovery of the soliton self-frequency shift, Opt. Lett. 11, 659–661 (1986).

[86] Y. Tang, L. G. Wright, K. Charan, T. Wang, C. Xu, and F. W. Wise, Generation of intense 100 fs solitons tunable from 2 to 4.3 μm in fluoride fiber, Optica 3, 948–951 (2016).

[87] T. Cheng, Y. Kanou, K. Asano, D. Deng, M. Liao, M. Matsumoto, T. Misumi, T. Suzuki, and Y. Ohishi, Soliton self-frequency shift and dispersive wave in a hybrid four-hole $AsSe_2$-As_2S_5 microstructured optical fiber, Appl. Phys. Lett. 104, 121911 (2014).

[88] T. Südmeyer, J. Aus der Au, R. Paschotta, U. Keller, P. G. R. Smith, G. W. Ross, and D. C. Hanna, Femtosecond fiber-feedback optical parametric oscillator, Opt. Lett. 26, 304–306 (2001).

[89] T. Südmeyer, E. Innerhofer, F. Brunner, R. Paschotta, T. Usami, H. Ito, S. Kurimura, K. Kitamura, D. C. Hanna, and U. Keller, High-power femtosecond fiber-feedback optical parametric oscillator based on periodically poled stoichiometric $LiTaO_3$, Opt. Lett. 29, 1111–1113 (2004).

[90] F. Kienle, P. S. Teh, Shaif-Ul Alam, Corin BE Gawith, David C. Hanna, David J. Richardson, and David P. Shepherd, Compact, high-pulse-energy, picosecond optical parametric oscillator, Opt. Lett. 35, 3580–3582 (2010).

[91] T. Steinle, F. Neubrech, A. Steinmann, X. Yin, and H. Giessen, Mid-infrared Fourier-transform spectroscopy with a high-brilliance tunable laser source: investigating sample areas down to 5 μm diameter, Opt. Express 23, 11105–11113 (2015).

[92] K. A. Ingold, A. Marandi, M. JF Digonnet, and R. L. Byer, Fiber-feedback optical parametric oscillator for half-harmonic generation of sub-100-fs frequency combs around 2 μm, Opt. Lett. 40, 4368–4371 (2015).

[93] L. F. Mollenauer and R. H. Stolen, The soliton laser, Opt. Lett. 9, 13 (1984).

[94] I. N. Duling, All-fiber ring soliton laser mode locked with a nonlinear mirror, Opt. Letters 16, 539–541 (1991).

[95] S. M. J. Kelly, Characteristic sideband instability of periodically amplified average soliton, Electron. Lett. 28, 806–807 (1992).

[96] N. J. Smith, K. J. Blow, and I. Andonovic, Sideband generation through perturbations to the average soliton model, J. Lightwave Technol. 10, 1329–1333 (1992).

[97] F. W. Wise, A. Chong, and W. H. Renninger, High-energy femtosecond fiber lasers based on pulse propagation at normal dispersion, Laser Photonics Rev. 2, 58–73 (2008).

[98] D. T. Reid, J. M. Dudley, M. Ebrahim-Zadeh, and W. Sibbett, Soliton formation in a femtosecond optical parametric oscillator, Opt. Lett. 19, 825–827 (1994).

[99] O. Paul, A. Quosig, T. Bauer, M. Nittmann, J. Bartschke, G. Anstett, and J. A. L'huillier, Temperature-dependent Sellmeier equation in the MIR for the extraordinary refractive index of 5% MgO doped congruent $LiNbO_3$, Appl. Phys. B 86, 111–115 (2007).

[100] T. J. Driscoll, G. M. Gale, and F. Hache, Ti: sapphire second-harmonic-pumped visible range femtosecond optical parametric oscillator, Opt. Commun. 110, 638–644 (1994).

[101] W. J. Tomlinson, R. H. Stolen, and A. M. Johnson, Optical wave breaking of pulses in nonlinear optical fibers, Opt. Lett. 10, 457–459 (1985).

[102] R. Deiterding, R. Glowinski, H. Oliver, and S. Poole, A reliable split-step Fourier method for the propagation equation of ultrafast pulses in single-mode optical fibers, J. Lightwave Technol 31, 2008–2017 (2013).

[103] P. Grelu, and N. Akhmediev, Dissipative solitons for mode-locked lasers, Nat. Photonics 6, 84 (2012).

[104] M. Chernysheva, A. Bednyakova, M. Al Araimi, R. CT Howe, G. Hu, T. Hasan, A. Gambetta, G. Galzerano, M. Rümmeli, and A. Rozhin, Double-Wall Carbon Nanotube Hybrid Mode-Locker in Tm-doped Fibre Laser: A Novel Mechanism for Robust Bound- State Solitons Generation, Sci. Rep. 7, 44314 (2017).

[105] J. Peng, and H. Zeng, Build-Up of Dissipative Optical Soliton Molecules via Diverse Soliton Interactions, Laser Photonics Rev. 12, 1800009 (2018).

[106] F. Adler, K. C. Cossel, M. J. Thorpe, I. Hartl, M. E. Fermann, and J. Ye, Phase-stabilized, 1.5W frequency comb at 2.8–4.8 μm, Opt. Lett. 34, 1330–1332 (2009).

[107] A. Woutersen, U. Emmerichs, and J. H. Bakker, Femtosecond mid-IR pump-probe spectroscopy of liquid water: Evidence for a two-component structure, Science 278, 658–660 (1997).

[108] S. Cha, J. H. Sung, S. Sim, J. Park, H. Heo, M. H. Jo, M, and H. Choi, 1s-intraexcitonic dynamics in monolayer MoS_2 probed by ultrafast mid-infrared spectroscopy, Nat. Commun. 7, 10768 (2016).

[109] S. Chaitanya Kumar, A. Esteban-Martin, T. Ideguchi, M. Yan, S. Holzner, T. W. Hänsch, N. Picqué and M. Ebrahim-Zadeh, Few-cycle, broadband, mid-infrared optical parametric oscillator pumped by a 20-fs Ti:sapphire laser, Laser Photonics Rev. 8, L86–L91 (2014).

[110] Radiantis, Oria IR, http://www.radiantis.com/oria-ir-opo.html

[111] R. Das, S. Chaitanya Kumar, G. K. Samanta, and M. Ebrahim- Zadeh, Broadband, high-power, continuous-wave, mid-infrared source using extended phase-matching bandwidth in MgO:PPLN, Opt. Lett. 34, 3836–3838 (2009).

[112] H. S. Hung, J. Prawiharjo, N. K. Daga, D. C. Hanna, and D. P. Shepherd, J. Opt. Soc. Am. B 24, 2998–3006 (2007).

[113] Z. Zhang, J. Sun, T. Gardiner, and D. T. Reid, Opt. Express 19, 17127–17132 (2011).

[114] A. Aadhi and G. K. Samanta, Opt. Lett. 42, 2886–2889 (2017).

[115] Radiantis, Blaze, http://www.radiantis.com/products/ultrafast-laser-system/120-blaze.html

[116] H. Günzler and H. U. Gremlich, IR Spectroscopy: An Introduction. Berlin, Germany: Wiley-VCH (2002).

[117] S. Dupont, C. Petersen, J. Thøgersen, C. Agger, O. Bang, and S. R. Keiding, IR microscopy utilizing intense supercontinuum light source, Opt. Express 20, 4887-¡–4892 (2012).

[118] J. Hildenbrand, J. Herbst, J. Wöllenstein, and A. Lambrecht, Explosive detection using infrared laser spectroscopy, Proc. SPIE 7222, 72220B (2009).

[119] C. Petibois and G. Deleris, Chemical mapping of tumor progression by FT-IR imaging: Towards molecular histopathology, Trends Biotechnol. 24, 455–462 (2006).

[120] G. Edwards, R. Logan, M. Copeland, L. Reinisch, J. Davidson, B. Johnson, R. Maciunas, M. Mendenhall, R. Ossoff, J. Tribble, and J. Werkhaven, Tissue ablation by a free-electron laser tuned to the amide II band, Nature 371, 416–419 (1994).

[121] L. M. Mille and R. J. Smith, Synchrotrons versus globars, pointdetectors versus focal plane arrays: Selecting the best source and detector for specific infrared microspectroscopy and imaging applications, Vib. Spectrosc. 38, 237–240 (2005).

[122] J. Faist, Quantum Cascade Lasers, Oxford, U.K.: Oxford Univ. Press (2013).

[123] C. R. Petersen U. Møller, I. Kubat, B. Zhou, S. Dupont, J. Ramsay, T. Benson, S. Sujecki, N. Abdel-Moneim, Z. Tang, and Furniss, D, Mid-infrared supercontinuum covering the 1.4–13.3 μm molecular finger-print region using ultra-high NA chalcogenide step-index fibre, Nature Photon. 8, 830–834 (2014).

[124] M. Beutler, I. Rimke, E. Büttner, P. Farinello, A. Agnesi, V. Badikov, D. Badikov, and V. Petrov, Difference-frequency generation of ultrashort pulses in the mid-IR using Yb-fiber pump systems and $AgGaSe_2$, Opt. Express 23, 2730–2736 (2015).

[125] J. Krauth, A. Steinmann, R. Hegenbarth, M. Conforti, and H. Giessen, Broadly tunable femtosecond near-and mid-IR source by direct pumping of an OPA with a 41.7 MHz Yb: KGW oscillator, Opt. Express 21, 11516–11522 (2013).

[126] L. Kang, M. Zhou, J. Yao, Z. Lin, Y. Wu, and C. Chen, Metal thiophosphates with good mid-infrared nonlinear optical performances: A first-principles prediction and analysis, J. Amer. Chem. Soc. 137, 13049–13059 (2015).

[127] S. Chaitanya Kumar, P. G. Schunemann, K. T. Zawilski, and M. Ebrahim- Zadeh, Advances in ultrafast optical parametric sources for the midinfrared based on $CdSiP_2$, J. Opt. Soc. Am. B. 33, D44–D56 (2016).

[128] A. Peremans, D. Lis, F. Cecchet, P. G. Schunemann, K. T. Zawilski, and V. Petrov, Noncritical singly resonant synchronously pumped OPO for generation of picosecond pulses in the mid-infrared near 6.4 μm, Opt. Lett. 34, 3053–3055 (2009).

[129] O. Chalus, P. G. Schunemann, K. T. Zawilski, J. Biegert, and M. Ebrahim- Zadeh, Optical parametric generation in $CdSiP_2$, Opt. Lett. 24, 4142–4144 (2010).

[130] G. Marchev, A. Tyazhev, V. Petrov, P. G. Schunemann, K. T. Zawilski, G. Stöppler, and M. Eichhorn, Optical parametric generation in $CdSiP_2$ at 6.125 μm pumped by 8 ns long pulses at 1064 nm, Opt. Lett. 37, 740–742 (2012).

[131] Z. Zhang, D. T. Reid, S. Chaitanya Kumar, M. Ebrahim-Zadeh, P. G. Schunemann, K. T. Zawilski, and C. R. Howle, Femtosecond-laser pumped $CdSiP_2$ optical parametric oscillator producing 100 MHz pulses centered at 6.2 μm, Opt. Lett. 38, 5110–5113 (2013).

[132] V. Ramaiah-Badarla, S. Chaitanya Kumar, A. Esteban-Martin, K. Devi, K. T. Zawilski, P. G. Schunemann, and M. Ebrahim-Zadeh, Ti:sapphire-pumped deep-infrared femtosecond optical parametric oscillator based on $CdSiP_2$, Opt. Lett. 41, 1708–1711 (2016).

[133] S. Chaitanya Kumar A. Esteban-Martin, A. Santana, K. T. Zawilski, P. G. Schunemann, and M. Ebrahim-Zadeh, Pump-tuned deep-

infrared femtosecond optical parametric oscillator across 6–7 μm based on $CdSiP_2$, Opt. Lett. 41, 3355–3358 (2016).

[134] N. Leindecker, A. Marandi, R. L. Byer, K. L. Vodopyanov, J. Jiang, I. Hartl, M. Fermann, and P. G. Schunemann, Octave-spanning ultrafast OPO with 2.6–6.1 μm instantaneous bandwidth pumped by femtosecond Tm-fiber laser, Opt. Express 20, 7046–7053 (2012).

[135] B. Metzger, B. Pollard, I. Rimke, E. Büttner, and M. B. Raschke, Single step sub-200 fs mid-infrared generation from an optical parametric oscillator synchronously pumped by an erbium fiber laser, Opt. Lett. 41, 4383–4386 (2016).

[136] P. Loza-Alvarez, C. T. A. Brown, D. T. Reid, W. Sibbett, and M. Missey, High-repetition-rate ultrashort-pulse optical parametric oscillator continuously tunable from 2.8 to 6.8 μm, Opt. Lett. 24, 1523–1525, (1999).

[137] I. Pupeza, D. Sánchez, J. Zhang, N. Lilienfein, M. Seidel, N. Karpowicz, T. Paasch-Colberg, I. Znakovskaya, M. Pescher, W. Schweinberger, V. Pervak, E. Fill, O. Pronin, Z. Wei, F. Krausz, A. Apolonski, and J. Biegert, High-power sub-two-cycle mid-infrared pulses at 100 MHz repetition rate, Nature Photon. 9, 721–724 (2015).

[138] P. Dumas, F. Polack, B. Lagarde, O. Chubar, J. L. Giorgetta, and S. Lefrançois, Synchrotron infrared microscopy at the French Synchrotron Facility SOLEIL, Infrared Phys. Techn. 49, 152–160 (2006).

[139] Y. Yu, X. Gai, P. Ma, D. Y. Choi, Z. Yang, R. Wang, S. Debbarma, S. J. Madden, and B. Luther-Davies, A broadband, quasi-continuous, mid-infrared supercontinuum generated in a chalcogenide glass waveguide, Laser Photon. Rev. 8, 792–798, (2014).